

---

# **Resilient Composites for Armor Applications**

Final Report

by E. R. Strutt, E. A. Olevsky, and M. A. Meyers

---

January 30, 2001

Army Research Office  
under contract  
DAAH04-95-1-0236

prepared by  
Department of Mechanical and Aerospace Engineering  
University of California, San Diego  
9500 Gilman Drive,  
La Jolla, CA 92093

Approved for public release; distribution unlimited

The views, opinions, and/or findings contained in this report are those of the authors and should not be construed as an official Department of the Army position, policy, or decision, unless so designated by other documentation.

# REPORT DOCUMENTATION PAGE

Form Approved  
OMB NO. 0704-0188

Public Reporting burden for this collection of information is estimated to average 1 hour per response, including the time for reviewing instructions, searching existing data sources, gathering and maintaining the data needed, and completing and reviewing the collection of information. Send comment regarding this burden estimate or any other aspect of this collection of information, including suggestions for reducing this burden, to Washington Headquarters Services, Directorate for Information Operations and Reports, 1215 Jefferson Davis Highway, Suite 1204, Arlington, VA 22202-4302, and to the Office of Management and Budget, Paperwork Reduction Project (0704-0188), Washington, DC 20503.

1. AGENCY USE ONLY (Leave Blank)		2. REPORT DATE 30 January 2001	3. REPORT TYPE AND DATES COVERED Final Report 1 June 95 - 30 May 00
4. TITLE AND SUBTITLE High Strain, High Strain-Rate Deformation of Fragmented Alumina (Revised title: Resilient Composites for Armor Applications)		5. FUNDING NUMBERS DAAH04-95-1-0236	
6. AUTHOR(S) E.R. Strutt, E.A. Olevsky, and M.A. Meyers (P.I.)			
7. PERFORMING ORGANIZATION NAME(S) AND ADDRESS(ES) The Regents of the University of California Office of Contract & Grant Administration, 0934 9500 Gilman Drive La Jolla, CA 92093-0934		8. PERFORMING ORGANIZATION REPORT NUMBER	
9. SPONSORING / MONITORING AGENCY NAME(S) AND ADDRESS(ES) U. S. Army Research Office P.O. Box 12211 Research Triangle Park, NC 27709-2211		10. SPONSORING / MONITORING AGENCY REPORT NUMBER U.S. Army Research Office <b>ARC 34271.1-MS-AAS</b>	

11. SUPPLEMENTARY NOTES  
The views, opinions and/or findings contained in this report are those of the author(s) and should not be construed as an official Department of the Army position, policy or decision, unless so designated by other documentation.

12 a. DISTRIBUTION / AVAILABILITY STATEMENT  Approved for public release; distribution unlimited.	12 b. DISTRIBUTION CODE
---	-------------------------

13. ABSTRACT (Maximum 200 words)

The original objectives of the proposed research were accomplished by H. C. Chen. After the successful completion of his Ph. D. Dr. Chen was employed by CERCOM and used the knowledge gained in his doctoral for the development of armor. He was actively involved in a number of defense projects, including the DARPA Light Weight Armor program coordinated by SwRI. The work in the AASERT proposal was published in Acta Materialia and the proceedings of the APS conference on shock compression of condensed matter:

H.C. Chen, M.A. Meyers, and V.F. Nesterenko, "Shear Localization in Granular and Comminuted Alumina," in "Shock Compression of Condensed Matter 1995," ed. S.C. Schmidt and W.C. Tao, AIP Press, (1996) 607-610.

V.F. Nesterenko, M.A. Meyers, and H-C. Chen, "Shear Localization in High Strain, High Strain Rate Deformation of Granular Alumina," Acta Met. et Mat., 44 2017-2026 (1996).

The objectives having been accomplished early, it was decided to redirect the program toward the processing, properties, and characterization of TiC-NiTi composites. Thus, the AASERT effort complemented and augmented the MURI in which the group was involved. Elizabeth Strutt, a US citizen, was supported by the AASERT program throughout a good portion of its duration. The results reported herein are primarily her doctoral work, that is at an advanced state. It is felt that this AASERT program was highly successful, leading to seven publications( listed in page xiv).

14. SUBJECT TERMS alumina, ballistic performance, SHS, TiC-NiTi composites			15. NUMBER OF PAGES 161
			16. PRICE CODE
17. SECURITY CLASSIFICATION OR REPORT UNCLASSIFIED	18. SECURITY CLASSIFICATION ON THIS PAGE UNCLASSIFIED	19. SECURITY CLASSIFICATION OF ABSTRACT UNCLASSIFIED	20. LIMITATION OF ABSTRACT  UL

NSN 7540-01-280-5500

Standard Form 298 (Rev.2-89)  
Prescribed by ANSI Std. Z39-18  
298-102

20010301 145

# Table of Contents

Table of Contents	i
List of Figures	iii
List of Tables	viii
Acknowledgements	x
Statement of Problem Studied	xi
Summary of Most Important Results	xii
List of Publications	xiv
List of Scientific Personnel	xv
1. Introduction and Objectives	1
2. Background: Titanium Carbide	3
2.1 Structure	3
2.2 Thermodynamics	6
2.3 Mechanical Behavior of $TiC_x$	7
3. Background: NiTi	10
3.1 Equilibrium Phase Diagram for Ni-Ti System	10
3.2 NiTi Martensite Phases	11
3.3 Driving Force for Martensitic Transformation	15
3.4 Transformation Temperatures	16
3.5 Mechanical Behavior of NiTi alloys	23
Tension	25
Compression	28
Bending	31
Fracture Toughness	32
Strain Rate	34
3.6 Strengthening Mechanisms in NiTi	39
Heat Treatment	40
Thermo-Mechanical Treatment	43
4. Background: TiC-NiTi Composites	44
4.1 Microstructure	44
4.2 Effects of Thermal Excursion	47
4.3 Effects of Mechanical Deformation	51
5. Background: Processing	56
5.1 SHS	57
5.2 Densification	62
6. Materials and Experimental Procedures	66
6.1 Starting Materials	66
6.2 Combustion Synthesis/ Densification Procedure	66
6.3 Material Characterization	72

6.4 Mechanical Testing	76
7. Preliminary Results and Discussion	83
7.1 Thermodynamic Analysis	83
Adiabatic Temperature Calculations	83
7.2 X-ray Diffraction Analysis	85
7.3 Shape Change During QIP	92
Theory	92
Equations Describing the Constitutive Behavior of a Porous Specimen	93
Equations Describing the Constitutive Behavior of PTM	95
Equation Describing the Constitutive Behavior of a Porous Specimen Embedded in PTM	95
Experimental Measurements of Shape Change	99
7.4 Indentation Experiments and Constitutive Response	101
7.5 SHS/QIP	104
7.6 $\text{TiC}_x$ Particle Size and Morphology	106
7.7 Chemistry of Matrix	109
7.8 DSC Results	117
7.9 In-Situ TEM	127
7.10 Mechanical Tests	133
References	146



## List of Figures

Figure 2.1	Phase diagram for the Ti-C system [Murray (1987)]	4
Figure 2.2	Lattice parameter of $\text{TiC}_x$ as a function of composition [Storms (1967)]	5
Figure 3.1	The equilibrium phase diagram for Ni-Ti [Murray (1986)]	11
Figure 3.2	The approximate lattice correspondence between the B2 parent phase and B19' martensite. The x, y, and z-axes denote the B2 coordinate system. The x', y', and z' axes denote the B19' coordinate system. It is not drawn to scale [Buchheit <i>et al.</i> (1996)].	13
Figure 3.3	(a) Electrical resistivity curve, (b) DSC curve for a 49.8Ti-50.2at%Ni alloy. Specimen was cold rolled (25%) and then annealed at 773 K for 3.6 ks Adapted from Nam <i>et al.</i> (1990).	17
Figure 3.4	Surface relief during martensite formation and reversion correlated with resistivity in a forged and heat treated Ti-50.5at%Ni alloy [Sandrock <i>et al.</i> (1971)]	18
Figure 3.5	Effect of thermal cycling on the electrical resistance vs. temperature for Ti-49.8at%Ni alloy, which was solution treated at 1273 K for 1 hour followed by quenching into ice water. The arrows indicate $R_s$ (labeled $T_R$ ), $M_s$ and $M_f$ [Miyazaki <i>et al.</i> (1986b)]	20
Figure 3.6	Composition dependence of the $M_s$ temperature (on cooling) [Hanlon <i>et al.</i> (1967)].	21
Figure 3.7	Effect of oxygen content on the $M_s$ temperature [Saburi (1998)]	22
Figure 3.8	Components of the stress (a) and strain (b) resolved perpendicular and parallel to a potential habit plane.	25
Figure 3.9	The changes in $M_s$ in a $\text{Ni}_{50.0}\text{Ti}_{50.0}$ alloy due to applied uniaxial tension (UT), uniaxial compression (UC), zero hydrostatic stress (ZH), and triaxial compression (TC) [Jacobus <i>et al.</i> (1996)]	25
Figure 3.10	Stress-strain curves as a function of temperature for a Ti-50.6at%Ni alloy that was solution treated at 1273 K for 1 hour and subsequently quenched in ice water [Miyazaki <i>et al.</i> (1981)].	27
Figure 3.11	Tension/compression hysteresis for a Ti-50.8at% alloy in (a) the B2 structure, (b) the superelastic range, and (c) the B19' structure. The $M_s$ temperature for this alloy is 268 K [Plietsch <i>et al.</i> (1997)]	30
Figure 3.12	Stress-strain curves of a 50.8at%Ni-Ti alloy tested in three-point, four-point, pure bending and tension [Wick <i>et al.</i> (1995)].	31

Figure 3.13	The fracture energy $E$ along $\sigma_{0.2}$ , $\sigma_p$ , and $\sigma_{UTS}$ for the different alloys in Table 3.3. In (a) and (b) the fracture energy is for sharp notch specimens. In (c) the fracture energy is for V-notch Charpy specimens. Figure (d) shows how $\sigma_{0.2}$ , $\sigma_p$ , and $\sigma_{UTS}$ are determined.	33
Figure 3.14	Stress-strain curves for CuAlNi single crystals tested at strain rates of 0.001 and 0.1/sec. The specimens were allowed to cool down between loading and unloading. The material was initially at 24 °C (23 °C above $M_s$ ) [Rodriguez <i>et al.</i> (1975)].	35
Figure 3.15	The thermal effect on loading and unloading CuAlNi single crystal crystals at various strain rates. The initial temperature was 24 °C (23 °C above $M_s$ ). [Rodriguez <i>et al.</i> (1975)].	36
Figure 3.16	Comparison of calculated and experimental stress-strain curves for NiTi [Wu <i>et al.</i> (1996)].	39
Figure 3.17	Time-temperature-transformation curves for a Ti-50.2at%Ni alloy [Nishida <i>et al.</i> (1986)]	41
Figure 3.18	Transmission electron micrograph of $Ti_3Ni_4$ precipitates in Ti-51.3at%Ni alloy aged at 500 °C [Saburi <i>et al.</i> (1982, 1989)].	42
Figure 4.1	Microstructure of vacuum hot pressed TiC-NiTi composites. (a) 10vol%TiC-NiTi [Mari <i>et al.</i> (1995a)], (b) 20vol%TiC-NiTi [Dunand <i>et al.</i> (1996)].	45
Figure 4.2	Microstructure of (a) etched 10vol%TiC-NiTi, showing large TiC particle surrounded by NiTi particles, (b) etched NiTi showing prior surfaces of metallic powder [Fukami-Ushiro <i>et al.</i> (1996a)].	46
Figure 4.3	Calorimetry spectra for the first thermal cycle of TiC-NiTi composites with a matrix composition of 51.4at%Ti-Ni (scanning rate: 20K/min) [Mari <i>et al.</i> (1995a)]	47
Figure 4.4	Calorimetry spectra for the 100 <sup>th</sup> cycle of TiC-NiTi composites with a matrix composition of 51.4at%Ti-Ni (scanning rate: 20 K/min) [Mari <i>et al.</i> (1995a)]	49
Figure 4.5	Stress-strain curves of TiC-NiTi composites tested at $T_d = A_f + 5$ K after cooling from $A_f + 20$ K. [Fukami-Ushiro <i>et al.</i> (1996a)]	53
Figure 4.6	Stress-strain curves of TiC-NiTi composites tested at $T_d = M_s + 5$ K after cooling from $A_f + 20$ K. [Fukami-Ushiro <i>et al.</i> (1996a)]	53
Figure 4.7	Stress-strain curves of TiC-NiTi composites tested at room temperature (below $M_f$ ) [Fukami-Ushiro <i>et al.</i> (1996a)].	55
Figure 5.1	Processing steps during Self-Propagating High Temperature Synthesis (SHS) of TiC-NiTi composites.	58

Figure 5.2	Sequence of formation of $\text{TiC}_x$ during SHS process. (a) Ni-Ti melt formation, homogenization, and capillary spreading around carbon particles. (b) Nucleation and growth of $\text{TiC}_x$ grains. (c) Continued growth and separation of $\text{TiC}_x$ . (d) Formation of $\text{TiC}_x$ chain. (e) Separation of chain into individual $\text{TiC}_x$ spherules which continue to grow by Ostwald ripening [LaSalvia <i>et al.</i> (1995b)].	61
Figure 5.3	Schematic illustration of Quasi-Isostatic Pressing (QIP).	63
Figure 5.4	Dependence of the residual porosity on the pressing delay time for consolidation of SHS produced material [Merzhanov (1990)].	65
Figure 6.1	Sample containment fixture.	68
Figure 6.2	Backscattered electron micrograph of alumina/graphite granular pressure transmitting medium.	70
Figure 6.3	Backscattered electron micrograph of alumina/graphite granular pressure transmitting medium after many SHS/QIP cycles.	70
Figure 6.4	Schematic representation of the loading as a function of time during the QIP densification process.	78
Figure 5.5	Instron machine with radiant furnace and ceramic compression arbor used For quasi-static experiments.	77
Figure 6.6	Configuration of the split hopkinson bar dynamic testing technique.	80
Figure 6.7	Ballistic test configuration for target that was not laterally confined (Configuration 1)	81
Figure 6.8	Ballistic test configuration for targets that were press fit into steel plate (Configuration) 2	82
Figure 7.1	Adiabatic temperature in TiC-NiTi system as a function of volume fraction of NiTi.	84
Figure 7.2	X-ray diffraction scan for stoichiometric TiC-40vol%NiTi	85
Figure 7.3	Backscattered electron micrograph TiC-40vol%NiTi. The microstructure, consisting of TiC particles surrounded by a two-phase matrix, is typical of composites synthesized with the anticipation of stoichiometric carbide formation.	86
Figure 7.4	X-ray diffraction scan for nonstoichiometric $\text{TiC}_{0.7}$ -40vol%NiTi	88
Figure 7.5	Backscattered electron micrograph of nonstoichiometric $\text{TiC}_{0.7}$ -40vol%NiTi. The microstructure, consisting of spheroidal TiC particles surrounded by a NiTi matrix, is typical of composites synthesized with the anticipation of the formation of nonstoichiometric carbide.	88
Figure 7.6	Selected area diffraction pattern in $\text{TiC}_{0.7}$ -40vol%NiTi showing 6-fold rotational symmetry. The pattern matches the NiTi B2 structure. [Courtesy of Dr. A. J. Strutt]	89

Figure 7.7	X-ray diffraction scans for $\text{TiC}_{0.7}$ -NiTi samples with an initial compact size of 7.5 cm in diameter and 300 g	91
Figure 7.8	Loading mode under Quasi-Isostatic Pressing	93
Figure 7.9	Shrinkage anisotropy as a function of specimen porosity under QIP.	98
Figure 7.10	(a) Schematic of indentation setup; (b) Cross-section of indented TiC-NiTi specimen, showing distortion and full densification under indenter	102
Figure 7.11	(a) Experimentally obtained stress strain response of SHS product (TiC-NiTi); (b) Predictions of stress strain response using Skorohod equation and analytical framework for free-upsetting geometry ( $\sigma_{rr} = 0$ ), for different values of rheology parameter $n$ ( $A=180 \text{ MPa.s}^n$ ).	104
Figure 7.12	Comparison of pore structure in SHS synthesized TiC-40vol%NiTi. (a) as-reacted material, not subject to post reaction densification; (b) reacted and densified material.	105
Figure 7.13	The particle morphology of the 7.5 cm diameter $\text{TiC}_{0.7}$ -NiTi samples [Courtesy of Dr. T. Radetic, NCEM]	107
Figure 7.14	Transmission electron micrographs of $\text{TiC}_{0.7}$ -20vol%NiTi showing the interface between the TiC particles and the NiTi matrix [Courtesy C. Echer, NCEM]	109
Figure 7.15	Concentration profile for the $\text{TiC}_{0.7}$ -20NiTi measured by EDX in the transmission electron microscope [Courtesy of C Echer, NCEM].	111
Figure 7.16	Concentration profile for the $\text{TiC}_{0.7}$ -40NiTi measured by EDX in the transmission electron microscope [Courtesy of C. Echer, NCEM].	113
Figure 7.17	Concentration profile for the $\text{TiC}_{0.7}$ -60NiTi measured by EDX in the transmission electron microscope [Courtesy of C. Echer, NCEM].	114
Figure 7.18	SAD pattern taken from the matrix of the aged 80NiTi samples [Courtesy of Dr. T. Radetic, NCEM]	116
Figure 7.19	Calorimetry spectra for the $\text{TiC}_{0.7}$ -NiTi samples during the first thermal cycle (Scanning rate: $5^\circ\text{C/min}$ ) Curves have been shifted along the vertical axis in order to facilitate comparison of transformation temperatures. Samples sectioned from the 7.5 cm diameter, 300 g samples.	117
Figure 7.20	The calorimetry spectra for 20NiTi upon heating.	122
Figure 7.21	Calorimetry spectra for as-synthesized 80NiTi sample during the first thermal cycle (Scanning rate: $5^\circ\text{C/min}$ ).	124
Figure 7.22	Calorimetry spectra for aged 80NiTi sample (Scanning rate: $5^\circ\text{C/min}$ ).	126

Figure 7.23	In-situ experiments in 20NiTi. (a)-(d) $R \rightarrow B19'$ transformation upon cooling. (e)-(h) $B19' \rightarrow B2$ transformation upon heating. (a) $T=-45\text{ }^{\circ}\text{C}$ (b) $T=-65\text{ }^{\circ}\text{C}$ (c) $T=-86\text{ }^{\circ}\text{C}$ (d) $T=-112\text{ }^{\circ}\text{C}$ (e) $T=74\text{ }^{\circ}\text{C}$ (f) $T=80\text{ }^{\circ}\text{C}$ (g) $T=85\text{ }^{\circ}\text{C}$ (h) $T=86\text{ }^{\circ}\text{C}$ [Courtesy of Dr. T. Radetic, NCEM]	128
Figure 7.24	Nucleation of B19' at the intersection of a TiC interface and a NiTi grain boundary in 20NiTi [Courtesy of Dr. T. Radetic, NCEM].	130
Figure 7.25	The stress-strain curve for the 30NiTi composite tested at a temperature room temperature and loaded to approximately 2350 MPa. (a) First compression cycle. The small remaining strain upon unloading may result from residual stresses in the adhesive used to attach the strain gage. (b) Second compression cycle	135
Figure 7.26	The stress strain curve for another 30NiTi sample tested at $T_d=A_f+20\text{ }^{\circ}\text{C}$ and loaded to 2600 MPa	137
Figure 7.27	Stress-strain curve for $\text{TiC}_{0.7}$ -30vol%NiTi tested dynamically at a strain rate of $10^2/\text{sec}$ .	138
Figure 7.28	Fracture surface of failed $\text{TiC}_{0.7}$ -30vol%NiTi	139
Figure 7.29	Vickers hardness of SHS/QIP $\text{TiC}_{0.7}$ -NiTi composites compared to the hardness of monolithic TiC and $\text{TiC}_{0.7}$ [LaSalvia <i>et al.</i> (1992) and Kosolapova (1986)].	141
Figure 7.30	Photograph of $\text{TiC}_{0.7}$ -30 vol%NiTi plate and steel projectile after impact without lateral confinement.	142
Figure 7.31	Photograph of $\text{TiC}_{0.7}$ -30 vol%NiTi plate after 3850 Joule impact	144.
Figure 7.32	Photograph of $\text{TiC}_{0.7}$ -60 vol%NiTi (a) after 1885 Joule impact and (b) after 6507 Joule impact.	145

## List of Tables

Table 2.1	Thermodynamic properties of stoichiometric TiC [Shackelford (1994)]	7
Table 2.2	Mechanical properties of $\text{TiC}_x$ compounds. Data is compiled from [1] Kosolapova (1986), [2] Miracle <i>et al</i> (1983), and [3] Das <i>et al.</i> (1982).	9
Table 3.1	Lattice correspondence between B19' martensite variants (indexed m) and B2 parent phase (indexed B2) [Miyazaki <i>et al.</i> (1989), Plietsh <i>et al.</i> (1997)].	14
Table 3.2	SIM transformation strains, given in percent, along $[111]_{\text{B2}}$ , $[110]_{\text{B2}}$ and $[100]_{\text{B2}}$ directions. Tension strains are positive, compression strains are negative [Plietsh <i>et al.</i> (1997)].	14
Table 3.3	The nominal composition and transformation temperatures, determined by dilatometry, for the alloys in Figure 3.13 [Melton <i>et al.</i> (1981)].	33
Table 5.1	Conventional methods used to synthesize TiC-NiTi composites.	56
Table 6.1	Impurity content for -325 mesh Ti powder from Micron Metals, Inc.	67
Table 6.2	Impurity content for 3 micron Ni powder from Aldrich Chemical Co.	67
Table 6.3	Impurity content of 2 micron C powder from Cerac, Inc.	67
Table 6.4	Characteristic times during QIP densification of SHS produced TiC-NiTi composites.	71
Table 6.5	Chemical composition of NiTi standard used to determine matrix chemistry of TiC-NiTi composites. Reporting level $\pm 1\%$ .	75
Table 6.6	Theoretical densities of TiC-NiTi and $\text{TiC}_{0.7}$ -NiTi composites	76
Table 7.1	Comparison of theoretical and experimental results on QIPing of Ni and Ti porous samples	100.
Table 7.2	The times and pressures that produced the best results for the 7.5 cm samples loaded according to the configuration in Figure 6.1.	106
Table 7.3	$\text{TiC}_x$ particle size as a function of NiTi content in $\text{TiC}_{0.7}$ -NiTi composites. Compact size 3cm diameter, 25g.	107
Table 7.4	Composition of matrix of 7.5 cm diameter $\text{TiC}_{0.7}$ -NiTi composites. The corresponding standard deviations are presented in parentheses.	110
Table 7.5	Measured net enthalpy of transformation during cooling and estimate of fraction of martensite formed.	119
Table 7.6	Transformation temperatures measured by differential scanning calorimetry	120
Table 7.7	Measured net enthalpy of transformation during heating	122

Table 7.8	The transformation temperatures measured in the DSC and in the TEM.	131
Table 7.9	Transformation temperatures in $\text{TiC}_{0.7}$ -30NiTi measured by acquiring calorimetry spectra between 20 °C and 150 °C. (It is worth noting that the this composite was formed from an original powder compact that was only 150 g in mass and 6.4 cm in diameter)	133
Table 7.10	Flexural strength of $\text{TiC}_{0.7}$ -30vol%NiTi.	140
Table 7.11	Vickers hardness of $\text{TiC}_{0.7}$ -NiTi composites.	140
Table 7.12	Summary of the ballistic tests performed in Configuration 2.	143

## Acknowledgements

This material is based upon work supported by the U.S. Army Research Offices under contracts DAAH04-95-1-0236 and DAAH04-96-1-0376, by the San Diego County Minority Fellowship Program, and by the Director, Office of Science, Office of Basic Energy Sciences, of the U.S. Department of Energy under Contract No. DE-AC03-76SF00098. The transmission electron microscopy work was performed at the National Center for Electron Microscopy, Lawrence Berkeley National Laboratory, University of California, Berkeley, CA 94720.

E.R. Strutt would like to thank Dr. J.C. LaSalvia for the guidance at the beginning of this investigation, which includes all the training in powder processing, SHS and densification. This research on TiC-NiTi composites was an extension of his work on the TiC-Ni-Mo system.

The authors would like to thank Dr. T. Radetic of the National Center for Electron Microscopy (NCEM) for performing the TEM characterization of the  $\text{TiC}_{0.7}\text{-NiTi}$  composites. The in-situ transformation experiments took many hours and often required working late into the night. E.R. Strutt would also like to thank her for the many in-depth discussions on crystallography and twinning. Her kindness and knowledge have been of great help. E.R. Strutt would like to thank C. Echer of NCEM for the acquisition of EDX data and for coordinating the use of the Be-tipped double tilt analytical holder. E.R. Strutt would like to thank NCEM for the use of their facilities and expertise for four months.

The authors would like to thank Dr. V.F. Nesterenko and Dr. S. Indrakanti for the use of the vacuum furnace and cut-off saw. The authors would like to thank the Analytical Facility of Scripps Institution of Oceanography for the training and use of the XRD, microprobe, and SEM. We thank D. Wright, Dr. A Rohatgi, and Dr. K. Vecchio for the training and use of DSC equipment.

The authors would like to thank D. Schickele, Manager of the Engineering Research Support Shop, for press-fitting the ballistic targets into steel-plates and for help designing and building various fixtures required during this investigation.

The authors would like to thank D. Lischer, J. Isaacs, Dr. S. Nemat-Nasser of the Center of Excellence for Advanced Materials (CEAM), for use of the CEAM mechanical test facilities and for the ballistic test using the 0.0019 kg projectile. The authors would like to thank Dr. W. Goldsmith of UC Berkeley for the ballistic tests using 0.031kg projectiles.

The authors would like to thank B.A. Burlingame for the financial administration of this program. E.R. Strutt would also like to thank her for coordinating the San Diego County Minority Fellowship.



## Statement of Problem Studied

This research focused on the production of TiC-NiTi composites by self-propagating high temperature synthesis combined with subsequent pressing in a granular medium. Most ceramics and cermets are produced by conventional sintering and hot pressing techniques. These methods require operation of high cost equipment for long times, in order to drive the complete conversion from reactants to products. An alternative, more energy efficient technique, known as self-propagating high temperature synthesis (SHS) uses the energy of the exothermic reaction between elemental metal and nonmetal powders to sustain the reaction as a combustion wave. This process results in the complete conversion from reactants to products within seconds after ignition. Unfortunately, the products of SHS tend to be highly porous and the pores must be removed if the material is going to be used in load bearing applications. One of the simplest and least expensive methods of consolidation involves surrounding the reactant material in a bed of graphite and alumina particulate before initiation of the combustion reaction. The sample can be ignited within the particulate and subjected to a uniaxial load immediately after passage of the combustion wave. The granular particulate acts as a pressure-transmitting medium that provides lateral confinement and redistributes the applied axial load to create a quasi-isostatic state of stress in the material. This method is known as Quasi-Isostatic Pressing (QIP). In this research the combined SHS/QIP method was used to produce TiC-NiTi composites. The goals included control of the product phase composition, microstructure, and porosity. The parameters that were considered for the optimization included the reactant chemical mixture, the initial powder compact porosity, the delay time between ignition and consolidation, and the applied load.

The second aspect of this investigation involved studying the effects of the TiC inclusions on the martensitic transformations of NiTi. Near stoichiometric NiTi undergoes a martensitic transformation from a cubic phase (B2) to either a rhombohedral R-phase or a monoclinic phase (B19'). These transformations are induced by changes in temperature or stress. In TiC-NiTi composites, differences in the thermal expansion coefficients and the elastic constants of the constituents result in the creation internal stresses in the material. These internal stresses should affect the movement of NiTi transformation fronts and the arrangement of B19' variants. In this research, in-situ TEM was performed to directly observe the microstructure, transformation path, and martensite nucleation and growth.

The final aspect of this research involved investigating the ballistic performance of TiC-NiTi composites. Since NiTi accommodates strain through phase transformation, twinning, and slip, it could act to toughen ceramic-based composites and provide a damage tolerant armor material with multiple hit capability.

## Summary of the Most Important Results

An investigation into the production of TiC-NiTi composites by a technique combining self-propagating high temperature synthesis (SHS) of elemental powders with densification by quasi-isostatic pressing (QIP) has been performed. Composites with varying volume fractions of NiTi were produced, and the resulting structures and transformation behavior were characterized.

Powder mixtures prepared anticipating the formation of stoichiometric TiC result in the formation of composites with a eutectic matrix of  $\text{Ni}_3\text{Ti}$  and NiTi. This titanium impoverishment of the matrix is consistent with the formation of nonstoichiometric  $\text{TiC}_x$  during the combustion reaction. The  $\text{Ni}_3\text{Ti}$  phase can be suppressed by anticipating the formation of  $\text{TiC}_{0.7}$  and adjusting the chemical content of the reactant mixture to include additional titanium.

The shape change during QIP densification of powder compacts can be modeled by analytical methods. The change in the aspect ratio depends on the porosity of the granular pressure-transmitting medium (PTM) that surrounds the powder compact and the initial compact dimensions and porosity. Experiments on Ni and Ti powder compacts show close agreement between the measured change in aspect ratio and the predicted change.

When combining QIP densification with the SHS process to make TiC-NiTi composites, the densification response after reaction depends on the constitutive description of the hot porous sample. Material parameters are necessary for implementation into computational codes, which can then predict the response of the material under a variety of loading configurations and enable a predictive shape

capability. Indentation tests provide an effective method to measure these material parameters.

The combined technique of SHS/QIP is an effective method for producing TiC-NiTi composites. The final porosity can be minimized by adjusting the time delay before application of the external load.

The room temperature structure of the NiTi matrix depends on the original compact size. For example, 3 cm samples of TiC<sub>0.7</sub>-40NiTi have a matrix structure which is B2 NiTi, while 7.5 cm samples of the same initial chemical composition have a matrix structure composed of R and B19' martensite. This is probably linked to differences in the cooling rates, which can cause changes in matrix chemistry. It may also be due to differences in the TiC<sub>x</sub> particle size.

In-situ TEM reveals that the multi-step  $B2 \rightarrow R \rightarrow B19'$  transformation occurs in the matrix upon cooling. The B19' nucleates at the TiC<sub>x</sub> interfaces and grows outward away from the particles. The growth of individual B19' variants is limited by impingement with other martensite variants. During heating, the direct  $B19' \rightarrow B2$  reaction occurs. The B19' variants that were among the last to form during the forward transformation, are the first to transform to B2 during the reverse transformation.

Ballistic tests on 40 mm targets show that a TiC<sub>0.7</sub>-30volume%NiTi composite with a thickness of only 4.3 mm (areal density = 2.1 g/cm<sup>2</sup>) can defeat a 3850 Joule projectile without any penetration into the steel back-plate. A TiC<sub>0.7</sub>-20volume%NiTi composite with a thickness of 5.8 mm (areal density 2.8 g/cm<sup>2</sup>) allows a 5544 Joule projectile to penetrate only a few millimeters into the steel back-plate.

## List of Publications

- E.A. Olevsky, E.R. Strutt, and M.A. Meyers, "Characterization by indentation of combustion synthesized cermets," *Scripta Mater.* (2000) accepted.
- E.R. Strutt, E.A. Olevsky, and M.A. Meyers, "Self-propagating high-temperature synthesis and densification of powder cermets," *Mater Prod. Techn.* (2000) - submitted
- E.A. Olevsky, E.R. Kristofetz, and M.A. Meyers, "Controlled net shape, density, and microstructure of TiC-NiTi cermets using quasi-isostatic pressing," *Intern. J. SHS*, 7(4), 517-528 (1999)
- E.R. Strutt, E.A. Olevsky, and M.A. Meyers, "Combustion Synthesis / Densification of Ceramics and Cermets", in: Powder Materials: Current Research and Industrial Practices, F.D.S. Marquis (ed.), The Minerals, Metals, & Materials Society, 73-89 (1999)
- E. Olevsky, E. Strutt, and M.A. Meyers, "Modeling and experimentation on indentation of combustion synthesized cermets," *Adv. Powd. Metall. Partic. Mater.*, 3.93-3.100 (1998)
- E. Olevsky, J. La Salvia, and M. Meyers, "Modeling and experimentation on quasi-isostatic pressing," *Adv. Powd. Metall. Partic. Mater.*, 20.13-20.19 (1997)
- E. Olevsky, E. Kristofetz, C. Uzoigwe, and M. Meyers, Optimization of combustion synthesis in TiC-based cermets, *Adv. Powd. Metall. Partic. Mater.*, 3.43-3.49 (1997)

## **List of Participating Scientific Personnel**

H.C. Chen, PhD UCSD awarded 1997  
C. Echer, NCEM\*  
Professor W. Goldsmith, UC Berkeley  
J Isaacs, CEAM<sup>8</sup>  
G Knowling, Undergraduate student, UCSD  
J.C LaSalvia, PhD  
D. Lischer, CEAM<sup>8</sup>  
Professor M. A. Meyers (P.I.), UC San Diego  
Professor S Nemat-Nasser, CEAM<sup>8</sup>  
Professor V.F. Nesterenko, UC Can Diego  
Professor E. A. Olevsky, San Diego State University  
T. Radetic, PhD, NCEM\*  
D. Schickele, Manager, Engineering Research Support Shop, UCSD.  
E. R. Strutt, PhD candidate UCSD  
C Uzoigwe, Undergraduate student UCSD

<sup>8</sup>CEAM      Center for Excellence in Advanced Materials,  
UC San Diego  
9500 Gilman Dr.  
LaJolla CA 92093

\*NCEM      National Center for Electron Microscopy  
Lawrence Berkeley National Laboratory  
Berkeley CA 94720  
(<http://ncem.lbl.gov>)

## **I. Introduction and Objectives**

In this research, TiC-NiTi composites were produced in order to investigate how stiff inclusions affect the martensitic transformations in NiTi. TiC-NiTi composites have been considered as candidate armor materials since at least 1977. In that year, D. Goldstein was issued a patent for the synthesis of TiC-NiTi armor plate by infiltration of porous carbon with a Ti-rich Ni-Ti alloy followed by heating to provide solid state conversion of the carbon into TiC. Goldstein used NiTi as the matrix for his composites, because NiTi can accommodate strain by phase transformation and twinning, as well as by slip. He recognized that these additional mechanisms of strain accommodation could act to toughen ceramic-based composites and provide a damage tolerant armor material with multiple hit capability.

Near stoichiometric NiTi undergoes a martensitic transformation from a cubic phase (B2) to either a rhombohedral phase (R-phase) or a monoclinic phase (B19'). The driving force for the transformation is the energy necessary to move atoms from positions in the parent structure to positions in the martensitic structure. This transformation can be induced by changes in temperature or stress. The martensitic transformations in NiTi under conditions of thermal excursion and external loading have been extensively studied. However, the introduction of stiff ceramic inclusions into NiTi creates internal stresses in the material, during either thermal cycling or external loading, because of differences in the thermal expansion coefficients and Young's moduli of the constituents. These internal stresses should affect the martensitic transformation, and have only begun to be studied in composites with low

volume fractions of reinforcement by Dunand and co-workers. Ultimately, in order to tailor the microstructure of TiC-NiTi armor materials, it is necessary to understand the interactions between the matrix and reinforcement in composites that have a high volume fraction of ceramic reinforcement. This work was initiated to study both the thermal and mechanical properties of TiC-NiTi composites and to directly observe the effect of carbide particles on the NiTi transformation by performing in-situ TEM.

In this research the TiC-NiTi composites with varying volume fractions of TiC have been produced by an energy efficient technique, known as self-propagating high temperature synthesis (SHS). SHS uses the energy of the exothermic reaction between elemental metal and nonmetal powders to sustain the reaction as a combustion wave. This process results in the complete conversion from reactants to products within seconds after ignition. The combustion reaction was combined with an in-situ densification technique, whereby the reactant material was surrounded in a bed of graphite and alumina particulate before initiation of the combustion reaction. The sample was ignited within the particulate and subjected to a uniaxial load immediately after passage of the combustion wave. The granular particulate acted as a pressure-transmitting medium that provided lateral confinement and redistributed the applied axial load to create a quasi-isostatic state of stress in the material. This method has been patented by Ceracon and is known as Quasi-Isostatic pressing (QIP).

## II. Background: Titanium Carbide

In order to determine the structure-property relationships in TiC-NiTi composites, it is necessary to have a thorough understanding of the characteristics of each of the constituents. It is important to review the elastic properties of the components, because the difference in the Young's modulus of the TiC and NiTi phases results in load transfer to the reinforcement. The TiC ceramic phase is typically a nonstoichiometric compound whose mechanical properties will depend on the metal-to-nonmetal ratio. Its load bearing ability will change with chemical composition. More significantly, the material is brittle at room temperature. This makes it sensitive to internal pores and surface flaws that act as sites for stress concentration. Cracks that form in TiC will not be blunted by localized plastic deformation, so they can result in catastrophic failure of the ceramic. In this section, the crystal structure, nonstoichiometry, and mechanical behavior of TiC will be reviewed.

### 2.1 Structure

The compound  $\text{TiC}_x$  has the B1 NaCl (rocksalt) structure. This structure consists of two interpenetrating FCC lattices of titanium and carbon in which the carbon atoms occupy the octahedral interstices of the Ti sublattice. Figure 2.1 shows the equilibrium phase diagram for the Ti-C system [Murray (1987)]. The  $\text{TiC}_x$  phase extends over the range  $x=0.49$  to 1.0, beyond which excess carbon precipitates. This wide range of composition results from vacancies in the carbon sublattice.



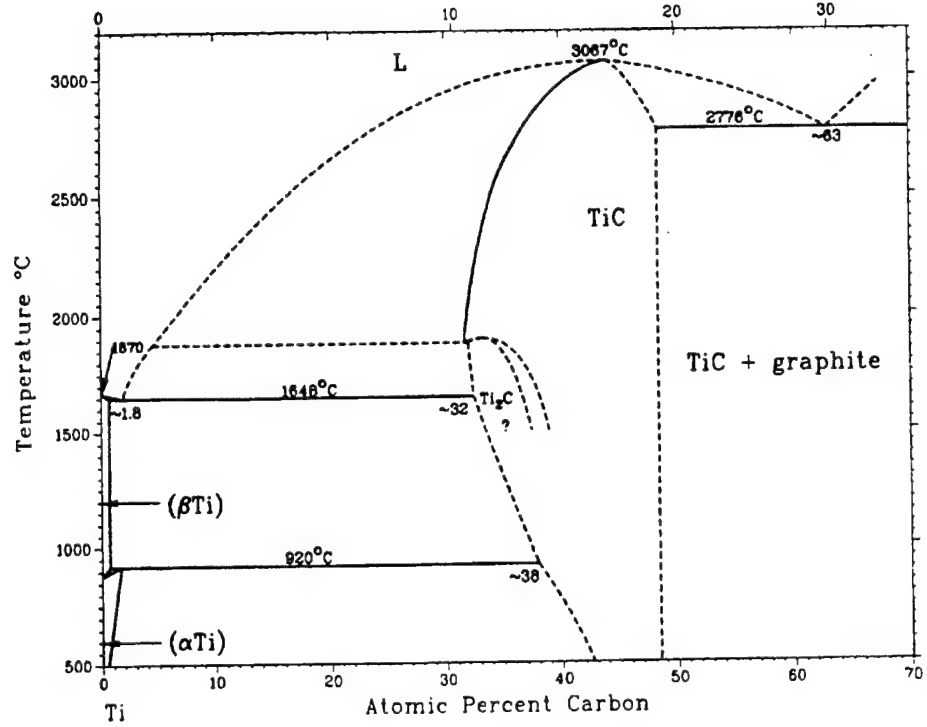


Figure 2.1 Phase diagram for the Ti-C system [Murray (1987)].

The lattice parameter of  $\text{TiC}_x$  depends on the composition. Figure 2.2 shows how the lattice parameter varies as a function of the carbon-to-titanium ratio (C/Ti) [Storms (1967)]. For the stoichiometric compound, the lattice parameter has a value of 0.4328 nm and the density is  $4.93 \text{ g/cm}^3$ .

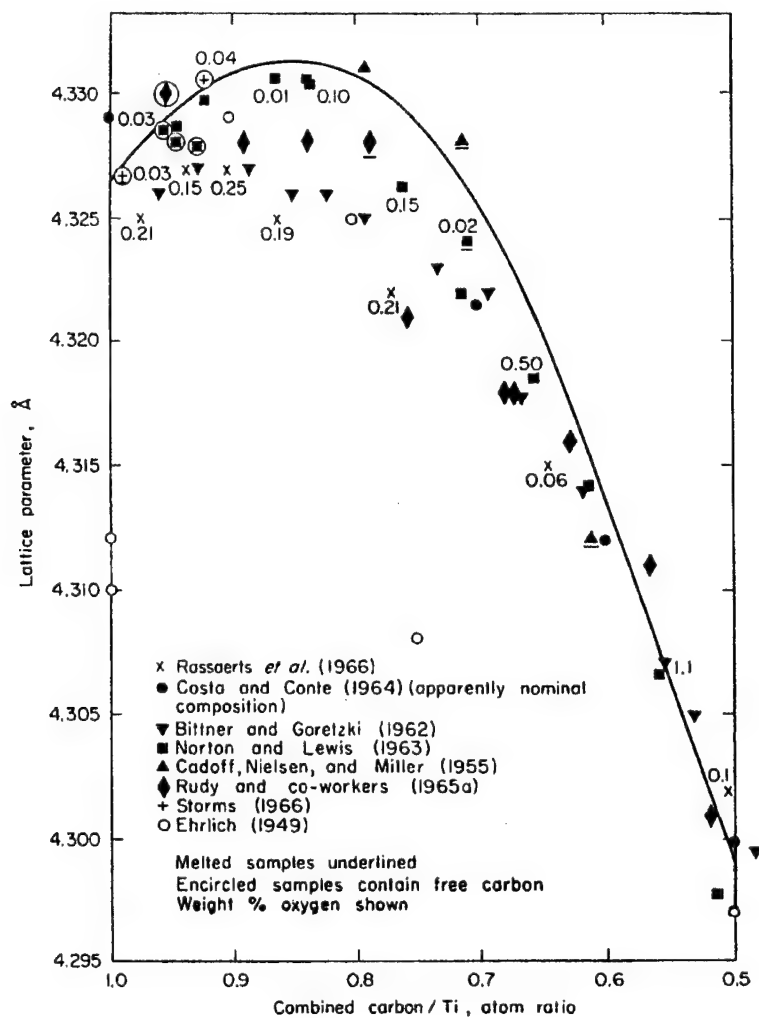


Figure 2.2 Lattice parameter of  $\text{TiC}_x$  as a function of composition [Storms (1967)]

The wide compositional range of  $\text{TiC}_x$  is extremely important to consider during powder processing of TiC-NiTi composites. Mixtures prepared anticipating formation of stoichiometric carbide may actually result in the formation of nonstoichiometric carbide particles surrounded by a titanium impoverished matrix. The loss of titanium in the matrix could lead to precipitation of Ni-rich phases, such as  $\text{Ni}_3\text{Ti}$ . [Poletika *et al.* (1983)].

Bonding in  $\text{TiC}_x$  is a combination of metal-to-metal and metal-to-nonmetal interactions. The directionality of the Ti-C bonds results in a high Peierls stress and limited dislocation mobility [Williams *et al.* (1962)]. The stress required for dislocation movement is so high that at ambient temperature it exceeds the stress required for fracture. Consequently,  $\text{TiC}_x$  is brittle at room temperature and its strength is limited by internal pores and flaws. In this research, porosity is minimized during the QIP densification process by adjusting the magnitude of the applied load and the time delay before loading.

## 2.2 Thermodynamics

The synthesis of TiC-NiTi composites by SHS is driven by the exothermic heat released during the reaction of elemental titanium and carbon powders. TiC has an extremely high heat of formation ( $\Delta H_{f,298} = -184.5 \text{ kJ/mol}$ ) which is sufficient to create a self-propagating combustion reaction in the material. The heat evolved during the reaction raises the temperature of the material to several thousands of degrees. These high temperatures cause melting of the NiTi, which facilitates the QIP densification process.

The thermodynamic properties of TiC are listed in Table 2.1. TiC has an extremely high melting temperature (3067 °C), which has made it popular for use in high temperature applications. The high melting temperature has also been used as evidence to support the hypothesis that the bonding in  $\text{TiC}_x$  is partially covalent [Williams *et al.* (1962)].

Table 2.1 also includes the thermal expansion coefficient of TiC. Differences in thermal expansion coefficient between TiC and NiTi can cause internal stresses in TiC-NiTi composites subjected to changes in temperature. In this research, TiC-NiTi composites with varying volume fractions of reinforcement will be thermally cycled to see how the internal stresses from thermal mismatch affect the phase transformation temperatures of the NiTi.

Table 2.1 Thermodynamic properties of stoichiometric TiC [Shackelford (1994)].

Heat of Formation $\Delta H_{f,298}(\text{kJ/mol})$	-184.5
Melting Temperature (°C)	3067
Average Thermal Expansion Coefficient (°C <sup>-1</sup> ) between 25-750 °C	$7.3 \times 10^{-6}$

### 2.3 Mechanical Behavior of $\text{TiC}_x$

The mechanical properties of TiC are listed in Table 2.2. They depend on the nonmetal-to-metal ratio, porosity and grain size. Both the Young's modulus and hardness decrease as the carbon content decreases. Since the number of carbon-to-titanium bonds is lower in nonstoichiometric  $\text{TiC}_x$ , these trends support the view that there is covalent bonding between titanium and carbon atoms, which limits dislocation

motion and controls the mechanical behavior of  $\text{TiC}_x$  at ambient temperature [Williams *et al.* (1962)].

The porosity and density are listed separately in Table 2.2, because sintered  $\text{TiC}_x$  compounds often contain heavy impurity elements which are not accounted for in calculations of the theoretical density. The additional mass from heavy impurities increases the density of the material, so that the “percentage of the theoretical density” is not necessarily a measure of the porosity.

Table 2.2 Mechanical properties of  $\text{TiC}_x$  compounds. Data is compiled from [1] Kosolapova (1986), [2] Miracle *et al.* (1983), [3] Das *et al.* (1982), and [4] Bauccio (1994).

	Porosity	Percentage Theoretical Density	Grain Size ( $\mu\text{m}$ )	E (GPa)	$\sigma_c$ (MPa)	$\sigma_{bend}$ (MPa)	Knoop Hardness (GPa)	Vickers Hardness (GPa)
TiC [4]	-----	-----	-----	-----	2958	-----	-----	-----
TiC [1]	1.0	-----	3	-----	-----	-----	-----	30.0
TiC [3]	-----	99-99.5%	8	-----	-----	520	19.2	-----
TiC <sub>0.99</sub> [1]	5.2	-----	5	494	-----	-----	-----	-----
TiC <sub>0.96</sub> [1]	1.5-5.0%	-----	-----	460	-----	-----	-----	-----
TiC <sub>0.950</sub> [1]	-----	-----	-----	-----	-----	-----	-----	27.9
TiC <sub>0.93</sub> [2]	-----	~100	14	-----	-----	475	17.5	-----
TiC <sub>0.905</sub> [1]	-----	-----	-----	-----	-----	-----	-----	26.1
TiC <sub>0.88</sub> [1]	5.0%	-----	12.0	465	-----	-----	-----	-----
TiC <sub>0.850</sub> [1]	-----	-----	-----	-----	-----	-----	-----	24.2
TiC <sub>0.83</sub> [1]	5.1%	-----	34.0	440	-----	-----	-----	-----
TiC <sub>0.83</sub> [2]	-----	97.7	20	-----	-----	250	15.1	-----
TiC <sub>0.800</sub> [1]	-----	-----	-----	-----	-----	-----	-----	23.5
TiC <sub>0.75</sub> [2]	-----	99.8	21	-----	-----	250	14.7	-----
TiC <sub>0.74</sub> [1]	5.0%	-----	64.7	420	-----	-----	-----	-----
TiC <sub>0.665</sub> [1]	-----	-----	-----	-----	-----	-----	-----	19.0
TiC <sub>0.66</sub> [2]	-----	99.9	22	-----	-----	300	12.8	-----

### III. Background: NiTi

In order to ultimately understand the mechanical behavior of TiC-NiTi composites, it is important to review the properties of near equiatomic Ni-Ti alloys. Nickel content, heat treatment, and thermo-mechanical treatment all affect the structure of NiTi and its martensitic transformations that are responsible for shape memory and superelasticity. To separate these effects of chemistry and processing on the NiTi from the effects of internal stresses generated by ceramic inclusions in TiC-NiTi composites will require careful measurement of matrix composition and microstructure.

#### 3.1 Equilibrium Phase Diagram for Ni-Ti System

Figure 3.1 shows the equilibrium phase diagram for Ni-Ti [Murray (1986)]. Although not shown the equilibrium NiTi B2 phase field is very narrow at temperatures below 923 K and is generally accepted to be only between 50.0 and 50.5 at% Ni. The NiTi B2 phase can be retained in Ni-rich NiTi alloys by quenching from the region of maximum solubility (1100 °C). The proposed eutectoid reaction  $\text{NiTi} \rightarrow \text{NiTi}_2 + \text{Ni}_3\text{Ti}$ , represented by the dashed line, does not exist. It has been shown by more recent work, that the impurity oxide  $\text{Ti}_4\text{Ni}_2\text{O}$  was confused with  $\text{NiTi}_2$  of similar structure [Saburi (1998)].

The narrow compositional range of B2 NiTi is bordered by regions of two-phase equilibrium of either  $\text{NiTi}_2 + \text{NiTi}$  or  $\text{Ni}_3\text{Ti} + \text{NiTi}$ . Since both  $\text{NiTi}_2$  and  $\text{Ni}_3\text{Ti}$  are relatively brittle phases and neither undergoes stress induced martensitic

transformations, formation of these phases is to be avoided in this work. Preliminary experiments have shown that this is possible if the composition is carefully tailored prior to the combustion synthesis reaction.

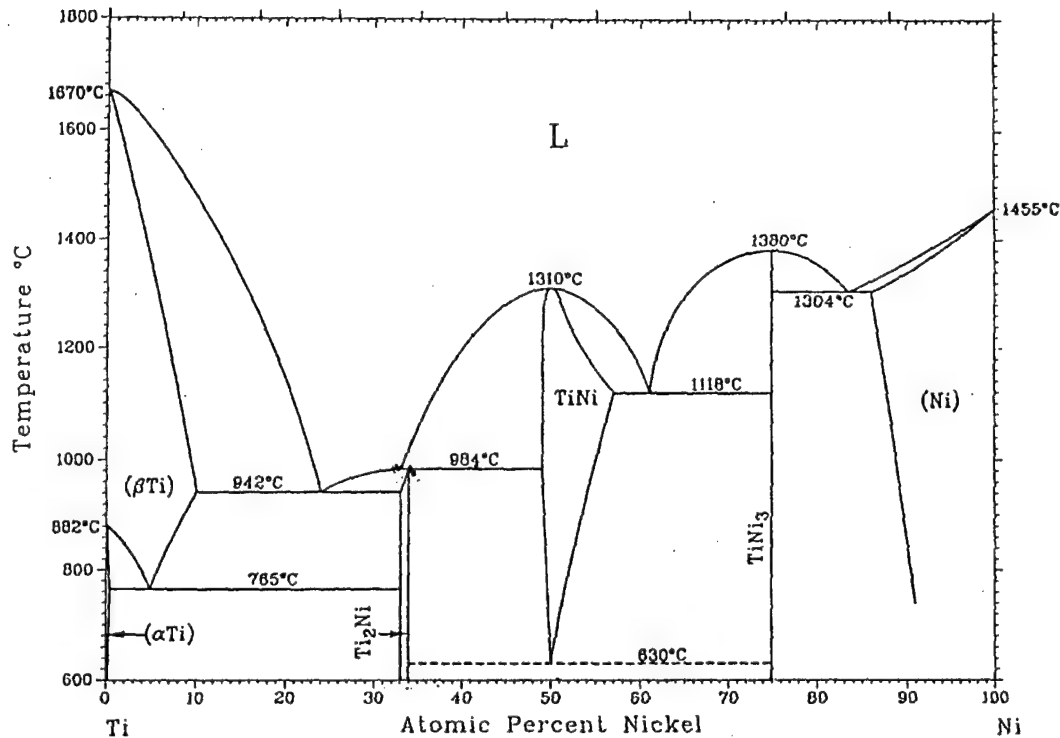


Figure 3.1 The equilibrium phase diagram for Ni-Ti [Murray(1986)].

### 3.2 NiTi Martensite Phases

In this research it is proposed that the NiTi matrix in TiC-NiTi composites will accommodate strain through stress induced phase transformation or martensite variant reorientation. NiTi alloys transform from a cubic B2 (CsCl) parent phase to a monoclinic B19' phase either directly or in two steps, i.e. B2 → rhombohedral phase (so-called R phase) → B19'. The direct transformation is reported in solution treated



NiTi. The transformation to the R phase is reported after cold working and subsequent annealing in near-equiatomic NiTi [Miyazaki *et al.* (1982, 1986a)], after aging between 400 °C and 700 °C in nickel rich NiTi [Saburi *et al.* (1982), Miyazaki *et al.* (1986a)], or after thermal cycling of solution treated NiTi [Miyazaki *et al.* (1986b)].

The  $B2 \rightarrow B19'$  and the  $B2 \rightarrow R \rightarrow B19'$  transformations are martensitic (diffusionless) transformations, and hence they are not associated with a compositional change. The martensite is produced from the parent phase by the cooperative movement of atoms whose individual displacements are significantly smaller than the interatomic spacing. This cooperative movement is possible because both the  $B19'$  and R martensite have a specific lattice correspondence with the B2 structure. It is this correspondence that makes the transformations crystallographically reversible and leads to the shape memory and superelastic effects. The following paragraphs describe each of these structures and their associated correspondences.

The parent NiTi phase has a B2 (CsCl) structure with space group  $Pm\bar{3}m$  [221]. Its lattice parameter is 0.3015nm [e.g. Otsuka *et al.* (1971)].

The  $B19'$  martensite is accepted to be monoclinic, but there is still some uncertainty about the space group. It has been reported to be  $P12_1/c1$  [Otsuka *et al.* (1971)],  $P112_1/m$  [Michal *et al.* (1981)], or both  $P112_1/m$  and  $P12_1/c1$  [Golestaneh *et al.* (1990)]. Its lattice parameters vary with composition. For a Ti-49.75at%Ni alloy, they have been reported to be  $a=0.4120$  nm,  $b=0.2889$  nm,  $c=0.4622$  nm, and  $\beta=96.8^\circ$ . The orientation relationship between the parent B2 phase and the  $B19'$  phase is of the type  $(001)_M$   $6.5^\circ$  from  $(101)_{B2}$  and  $[\bar{1}\bar{1}10]_M // [\bar{1}\bar{1}\bar{1}]_{B2}$  [Otsuka *et al.*

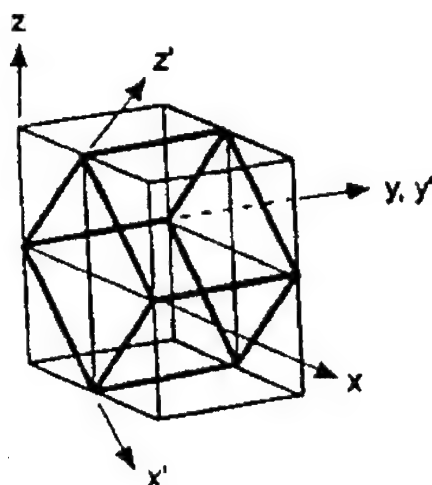


Figure 3.2. The approximate lattice correspondence between the B2 parent phase and B19' martensite. The  $x, y,$  and  $z$  axes denote the B2 coordinate system. The  $x', y',$  and  $z'$  axes denote the B19' coordinate system. It is not drawn to scale [Buchheit *et al.* (1996)].

(1971)]. The body diagonal of the parent B2 is approximately parallel to the face diagonal of the B19' martensite. This correspondence is shown in Figure 3.2 [Buchheit *et al.* (1996)]. The 12 variants that satisfy this relation are given in Table 3.1 [Miyazaki *et al.* (1989), Plietsch *et al.* (1997)]. Each of these different variants is twin related to one another. When the B19' is formed by cooling, these different variants form a self-accommodating structure characterized by a triangular morphology [Miyazaki *et al.* (1989)]. Under loading, the variant that accommodates the maximum amount of strain in the direction of the applied load grows at the expense of the others. This is because each variant is associated with a particular crystallographic transformation strain relative to the parent B2. These transformation strains define the limit of recoverable strain and are shown in Table 3.2 [Plietsch *et al.* (1997)].

Table 3.1 Approximate lattice correspondence between B19' martensite variants (indexed m) and B2 parent phase (indexed B2) [Miyazaki *et al.* (1989), Plietsh *et al.* (1997)]

Variant	$[100]_m$	$[010]_m$	$[001]_m$
1	$[011]_{B2}$	$[\bar{1}00]_{B2}$	$[0\bar{1}1]_{B2}$
2	$[0\bar{1}1]_{B2}$	$[\bar{1}00]_{B2}$	$[0\bar{1}\bar{1}]_{B2}$
3	$[0\bar{1}\bar{1}]_{B2}$	$[\bar{1}00]_{B2}$	$[01\bar{1}]_{B2}$
4	$[01\bar{1}]_{B2}$	$[\bar{1}00]_{B2}$	$[011]_{B2}$
5	$[101]_{B2}$	$[0\bar{1}0]_{B2}$	$[10\bar{1}]_{B2}$
6	$[\bar{1}01]_{B2}$	$[0\bar{1}0]_{B2}$	$[101]_{B2}$
7	$[\bar{1}0\bar{1}]_{B2}$	$[0\bar{1}0]_{B2}$	$[\bar{1}01]_{B2}$
8	$[10\bar{1}]_{B2}$	$[0\bar{1}0]_{B2}$	$[\bar{1}0\bar{1}]_{B2}$
9	$[110]_{B2}$	$[00\bar{1}]_{B2}$	$[\bar{1}10]_{B2}$
10	$[\bar{1}10]_{B2}$	$[00\bar{1}]_{B2}$	$[\bar{1}\bar{1}0]_{B2}$
11	$[\bar{1}\bar{1}0]_{B2}$	$[00\bar{1}]_{B2}$	$[\bar{1}\bar{1}0]_{B2}$
12	$[1\bar{1}0]_{B2}$	$[00\bar{1}]_{B2}$	$[110]_{B2}$

Table 3.2 SIM transformation strains, given in percent, along  $[111]_{B2}$ ,  $[110]_{B2}$  and  $[100]_{B2}$  directions. Tension strains are positive, compression strains are negative [Plietsh *et al.* (1997)].

Variant	$[111]_{B2}$	$[110]_{B2}$	$[100]_{B2}$
1	-3.7	-5.2	-4.2
2	-1.4	-5.2	-4.2
3	-3.7	+3.6	-4.2
4	+9.7	+3.6	-4.2
5	-3.7	+3.6	+2.6
6	+9.7	+3.6	+2.6
7	-3.7	-5.2	+2.6
8	-1.4	-5.2	+2.6
9	-3.7	-3.4	+2.6
10	-1.4	+8.4	+2.6
11	-3.7	-3.4	+2.6
12	+9.7	+8.4	+2.6

The R phase has rhombohedral symmetry with space group  $P\bar{3}1m$ . It is described by a hexagonal unit cell with dimensions  $a=0.738$  nm and  $c=0.532$  nm. The lattice correspondence between the parent B2 phase and the R phase is  $(111)_{B2} // (0001)_R$  and  $\langle \bar{2}11 \rangle_{B2} // \langle \bar{2}\bar{1}\bar{1}0 \rangle_R$ . [Goo *et al.* (1985)]. There are four variants that satisfy this relationship.

### 3.3 Driving Force for Martensitic Transformation

The driving force for a martensitic transformation in NiTi is the energy required to force the structural change between either B2 and B19', or B2 and R. This critical value is dependent only on the structural correspondences between the phases. It is equal to the energy necessary to move the atoms from positions in the parent structure to their positions in the martensitic structure. This driving energy ( $\Delta G$ ) can be provided by sufficient cooling and/or stress, since it is composed of two competing energy terms, a chemical term ( $\Delta G_c$ ) and a non-chemical term ( $\Delta G_{nc}$ ). The chemical component  $\Delta G_c$  is a measure of the net change in enthalpy and entropy between the different atomic configurations at a specific temperature ( $\Delta G_c = \Delta H - T\Delta S$ ). Since the amplitude of the atomic oscillations depend on temperature, the magnitude of  $\Delta G_c$  also depends on temperature. When the temperature is lowered below some critical point it becomes energetically favorable for the relatively open B2 structure to change to more close packed structures. The non-chemical term  $\Delta G_{nc}$  of the overall Gibbs free energy is primarily a measure of the stored elastic strain energy around the martensite. It is strongly affected by both internal and external stresses, which can

either assist or oppose the transformation. Since this term is sensitive to elastic strain energy, it is expected that the internal stresses from ceramic inclusions in TiC-NiTi composites will affect the volume fraction of martensite formed at a particular temperature.

### 3.4 Transformation Temperatures

The  $B2 \rightarrow B19'$  and  $B2 \rightarrow R \rightarrow B19'$  transformations are characterized by a series of transformation temperatures:

$R_s$	R-phase start temperature
$R_f$	R-phase finish temperature
$M_s$	B19' martensitic start temperature
$M_f$	B19' martensitic finish temperature
$A_s$	reverse transformation start temperature
$A_f$	reverse transformation finish temperature

These transformation temperatures are typically measured by either electrical resistivity (ER) or differential scanning calorimetry (DSC) techniques. Figure 3.3 shows the electrical resistivity versus temperature curve and the DSC curve for a thermo-mechanically treated 49.8Ti-50.2Ni (at%) alloy [Nam *et al.* (1990)]. DSC detects the changes in heat flow that occur in the alloy during a phase transformation. The onset temperature for the R-phase transformation,  $R_s$ , is defined as the temperature at which the heat flow first deviates from the baseline upon cooling. This is because the formation of the R-phase generates heat that can be detected as an exothermic peak on the DSC curve. When no more R martensite is formed upon further cooling, the DSC curve returns to the baseline. This point is defined as  $R_f$ , the R-phase finish temperature. It is important to note that  $R_s$  is not the same as  $R_f$ .

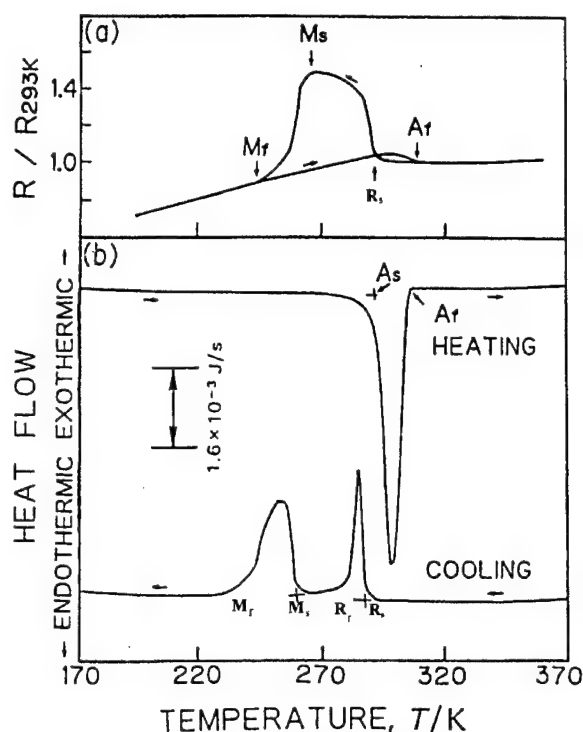


Figure 3.3 (a) Electrical resistivity curve, (b) DSC curve for a 49.8Ti-50.2at%Ni alloy. Specimen was cold rolled (25%) and then annealed at 773 K for 3.6 ks. Adapted from Nam *et al.* (1990).

because the elastic strain energy around the martensite resists further growth unless an additional chemical driving force (i.e. cooling) is available. The second peak on the DSC cooling curve is due to the  $R \rightarrow B19'$  transformation. The formation of  $B19'$  also gives off heat that creates an exothermic peak.  $M_s$  is where the  $B19'$  martensite starts to form upon cooling and  $M_f$  is where the  $B19'$  finishes forming. Upon heating, the reverse transformation occurs. This appears as a single endothermic peak on the DSC curve in Figure 3.3(b). The reverse start and finish temperatures are labeled as  $A_s$  and  $A_f$ , respectively. The absence of two peaks on heating reveals that this particular alloy transforms directly from  $B19' \rightarrow B2$ .

Figure 3.3 also shows the correspondence between the ER and DSC techniques for measuring transformation temperatures. The temperature at which the resistivity starts to increase on cooling coincides with  $R_s$  on the DSC curve within 2K. The temperature at which the resistivity starts to decrease coincides with  $M_s$ . The correspondence between the drop in resistivity and  $M_s$  has also been observed optically. Figure 3.4 shows the surface relief of a Ti-50.5at%Ni alloy during the martensitic transformation [Sandrock *et al.* (1971)]. The first observable formation of martensite upon cooling occurs very near the sharp negative break in the resistivity curve.

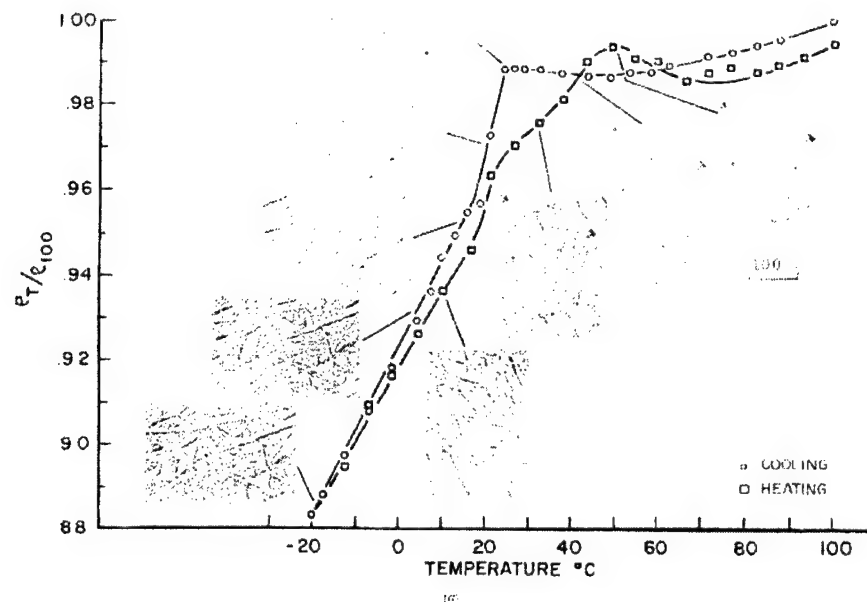


Figure 3.4 Surface relief during martensite formation and reversion correlated with resistivity in a forged and heat treated Ti-50.5at% Ni alloy [Sandrock *et al.* (1971)].

In this work, transformation temperatures of the TiC-NiTi composites will be measured either by differential thermal analysis (DTA) or electrical resistivity, depending upon the structure of the NiTi matrix at room temperature. The transformation temperatures of those samples that are martensitic at room temperature will be measured in the Perkin Elmer DTA 1700, which operates between ambient temperature and 1500 °C. The transformation temperatures of those samples with a B2 matrix at room temperature will be determined by the four-terminal electrical resistivity technique.

In order to study how TiC inclusions affect the structure of variant self-accommodation in the matrix of TiC-NiTi composites, samples will be thermally cycled through the B19' transformation within the TEM. It has been reported that thermal cycling can change the  $M_s$  temperature. Figure 3.5 shows the electrical resistance versus temperature curves, as a function of the number of thermal cycles, for a Ti-49.8at%Ni alloy that was solution treated at 1273 K followed by quenching in ice water [Miyazaki *et al.* (1986b)]. The arrows represent the  $R_s$  (labeled as  $T_R'$ ),  $M_s$ , and  $M_f$  transformation temperatures. These experiments show that  $M_s$  and  $M_f$  decrease with increasing number of thermal cycles, while  $R_s$  remains constant. Similar results have been obtained in solution treated Ti-50.6at%Ni and Ti-51.6at%Ni alloys. The decrease in  $M_s$  and  $M_f$  with thermal cycling has been attributed to the introduction and rearrangement of dislocations during the repeated motion of the parent-martensite interface. These dislocations change the internal stress field, thereby changing the amount of chemical energy (cooling) required to induce the transformation on further cycling. In contrast to the thermal cycling effects observed



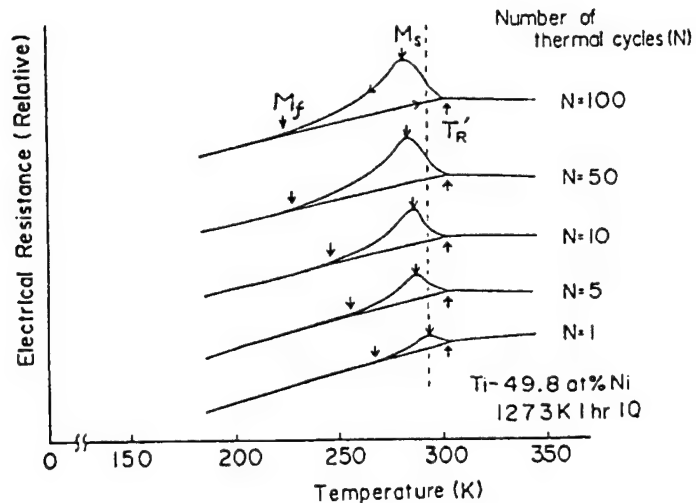


Figure 3.5 Effect of thermal cycling on the electrical resistance vs temperature for Ti-49.8at%Ni alloy which was solution treated at 1273 K for 1 hour followed by quenching into ice water. The arrows indicate  $R_s$  (labeled  $T_R$ ),  $M_s$  and  $M_f$  [Miyazaki *et al.* (1986b)].

in solution treated NiTi alloys, no changes in transformation temperatures during thermal cycling have been observed in aged Ni-rich alloys or annealed cold worked Ti-49.8at%Ni alloys. It is thought that the fine precipitates in aged Ni rich alloys and the high density dislocation network in cold worked NiTi restrict the introduction of mobile dislocations during thermal cycling.

For stress induced transformation to be effective in TiC-NiTi composites, the NiTi matrix should have the B2 structure at room temperature ( $293K > M_s$ ). It is also important that the  $M_s$  temperature under conditions of no load is not so low that the critical stress required to induce martensite formation approaches the critical stress for deformation by slip. For variant reorientation to be effective, the NiTi matrix should be in the martensite phase at room temperature. These transformation temperatures

can be controlled by adjustments of the nickel content or by ternary alloying. Figure 3.6 shows the effects of nickel content (expressed as at%Ti) on the  $M_s$  temperature [Hanlon *et al.* (1967)].  $M_s$  decreases sharply with small additions of nickel. This strong sensitivity to nickel makes precise microprobe or energy dispersive spectroscopy (EDS) measurements crucial for characterization.

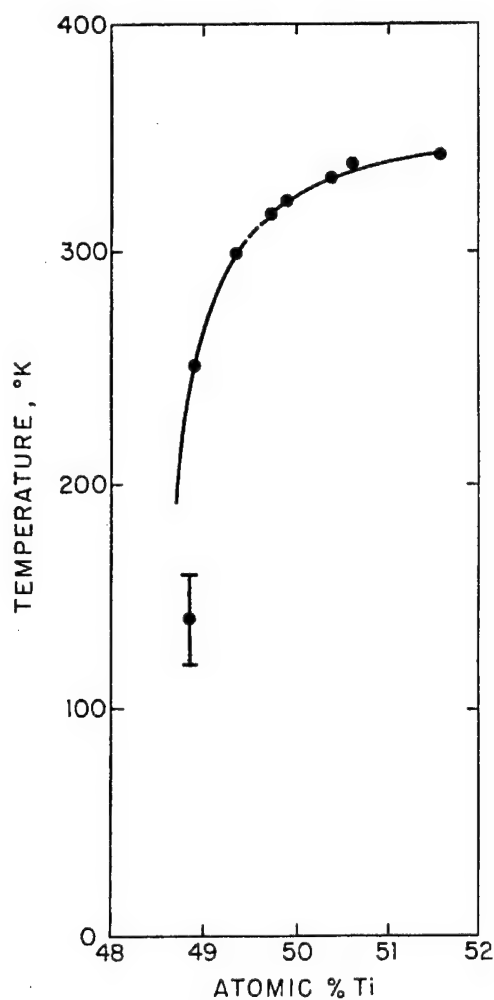


Figure 3.6 Composition dependence of the  $M_s$  temperature (on cooling) [Hanlon *et al.* (1967)].

Ternary alloying is also effective in adjusting transformation temperatures in NiTi alloys. The  $M_s$  temperature can be lowered either by substitution of vanadium, chromium, manganese, or aluminum for titanium, or by substitution of cobalt or iron for nickel. Conversely, the  $M_s$  temperature can be raised by substitution of palladium or gold for nickel [Saburi (1998)]. If necessary in this work, additions of these alloying elements can be made prior to the combustion synthesis reaction.

The TiC-NiTi composites studied in this project are synthesized in air, so it is useful to consider the effects of oxygen on the transformation temperature. Figure 3.7 shows the  $M_s$  plotted against oxygen content in specially prepared Ti-Ni-O alloys [Saburi (1998)]. The  $M_s$  decreases linearly with increasing oxygen. Since oxygen has limited solubility in NiTi (0.045 at%), this behavior has been attributed to the formation of the oxide  $Ti_4Ni_2O$ . As this oxide forms, it consumes twice the number of titanium atoms compared to the number of nickel atoms. This causes relative nickel enrichment of the NiTi, which is known to depress  $M_s$ .

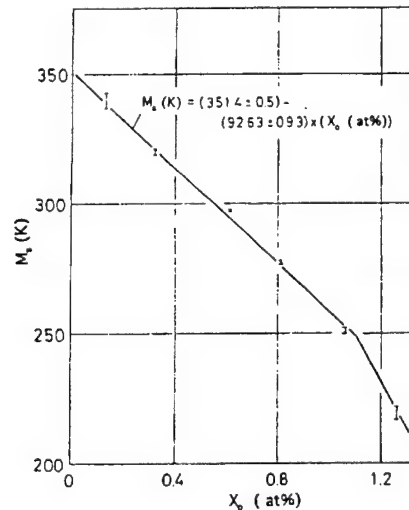


Figure 3.7 Effect of oxygen content on the  $M_s$  temperature [Saburi (1998)].

### 3.5 Mechanical Behavior of NiTi alloys

During mechanical loading of NiTi, the applied stress introduces mechanical work that can either assist or oppose the martensitic transformation. This mechanical work is the result of the interaction between the normal component of the applied stress ( $\sigma$ ) with the dilatational component of the transformation strain ( $\epsilon$ ), and the interaction of the shear component of the applied stress ( $\tau$ ) with the shear component of the transformation strain ( $\gamma$ ). Figure 3.8 shows the components of the stress and strain resolved perpendicular and parallel to a potential habit plane.  $\sigma$  is numerically positive when the normal stress is tensile, and negative when the normal stress is compressive.  $\tau$  is always taken to be positive because the 24 possible habit permutations in NiTi.

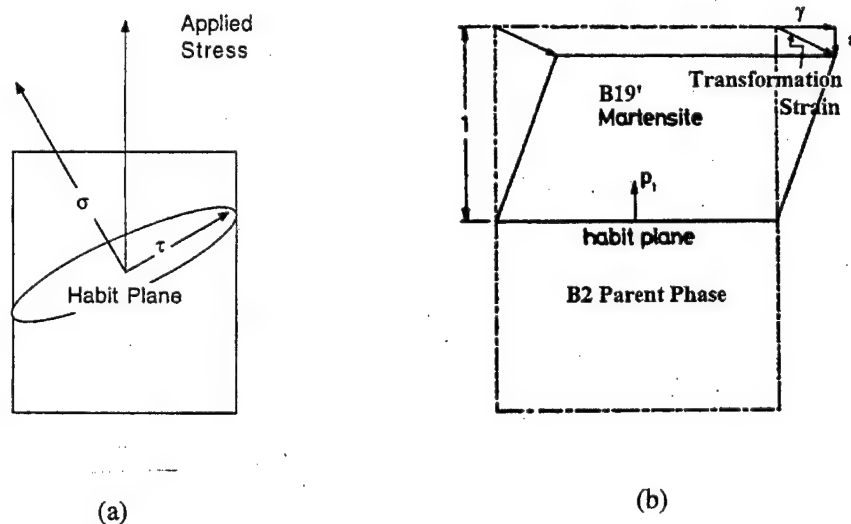


Figure 3.8 Components of the (a) stress and (b) strain resolved perpendicular and parallel to a potential habit plane.

Patel and Cohen (1953) proposed that the mechanical work of the applied stress contributes algebraically to the free energy of the system in the form of additional non-chemical energy terms,  $\sigma\varepsilon$  and  $\tau\gamma$ . Since the driving force  $\Delta G$  is constant and equal to the sum of  $\Delta G_c$  and  $\Delta G_{nc}$ , the non-chemical energy terms can either assist or oppose the transformation by increasing or decreasing the amount of chemical energy required to induce the transformation. Whether the mechanical work assists or opposes the transformation depends on the sign of the stress components. Since the B19' transformation is characterized by a negative volume change ( $\varepsilon < 0$ ), tensile stresses should oppose the transformation, compressive stresses should assist the transformation, and shear stresses should always assist the transformation. Figure 3.9 shows the changes in  $M_s$  for a polycrystalline  $\text{Ni}_{50.0}\text{Ti}_{50.0}$  alloy subjected to uniaxial tension (UT), uniaxial compression (UC), zero hydrostatic stress (ZH), and triaxial compression (TC) [Jacobus *et al.* (1996)]. These data appear to contradict the prediction of Patel and Cohen (1953), because the transformation in uniaxial tension requires a lower stress than in uniaxial compression. It is important to emphasize that the Patel and Cohen model does not consider the actual transformation strains that can be accommodated by the martensite variants. The transformation strains,  $\varepsilon$  and  $\gamma$ , are different in tension and compression. In polycrystalline NiTi, uniaxial tensile strains exceed uniaxial compressive strains by 50% (see Table 3.2). Consequently, the resolved shear component of the applied stress,  $\tau$ , in uniaxial tension aids the transformation more effectively than the resolved shear component in uniaxial compression.

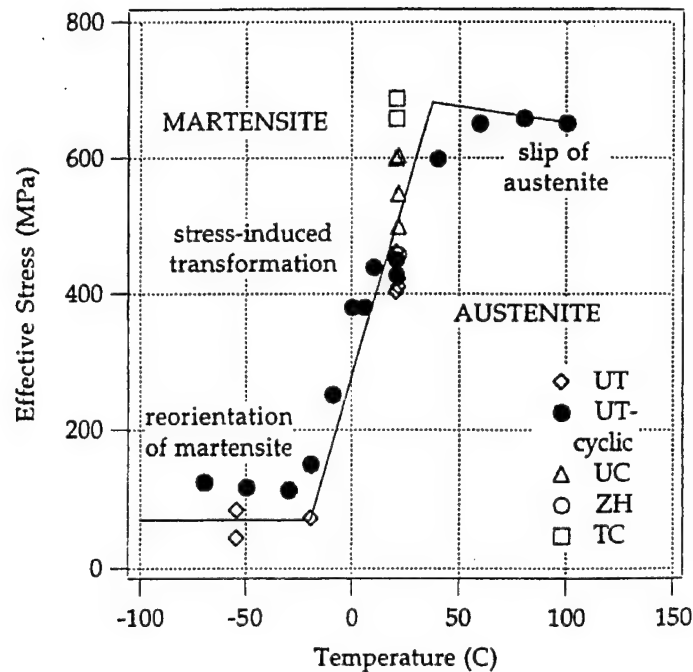


Figure 3.9 The changes in  $M_s$  in an  $Ni_{50.0}Ti_{50.0}$  alloy due to applied uniaxial tension (UT), uniaxial compression (UC), zero hydrostatic stress (ZH), and triaxial compression (TC) [Jacobus *et al.* (1996)]

A large portion of this research will focus on the mechanical behavior of TiC-NiTi composites, so a thorough review of the stress-strain behavior of NiTi is essential. The mechanical response of NiTi is dependent on composition, microstructure, test temperature, and deformation mode. All of these factors must be considered when interpreting data.

### Tension

Almost all data on the mechanical behavior of NiTi are from tests performed in tension. Typical tests study how the stress-strain response changes with temperature.

It has been found that the **shape memory** and **superelastic effects** depend on the relationship between the transformation temperatures (specifically  $M_s$  and  $A_f$ ) and the deformation temperature. Figure 3.10 shows the stress-strain curves (in tension) as a function of temperature for a Ti-50.6at%Ni alloy that was solution treated at 1273 K for 1 hour and subsequently quenched in ice water [Miyazaki *et al.* (1981)]. Its transformation temperatures (in the absence of an applied load) were  $M_f=128$  K,  $M_s=190$  K,  $A_s=188$  K, and  $A_f=221$  K. The stress-strain curves for this alloy can be divided into four temperature regimes corresponding to different deformation modes. The first range (I) includes curves (a)~(e) for which the test temperature was below  $M_s$  ( $T < M_s$ ) and the NiTi was completely in the B19' phase during loading. The curves are smooth and parabolic. This deformation behavior has been attributed to the movement of preexisting martensite plates or internal twins. The variants that could accommodate the maximum amount of strain in the direction of loading grew at the expense of the others. After unloading, most of the strain remained. The second range (II) includes curves (f)~(h) for which  $M_s < T < A_f$  and the alloy was initially in the B2 phase. These curves are characterized by sharp bending at the yield point and a broad plateau. These features have been attributed to the formation of stress induced martensite (SIM). After unloading, there was again residual strain. The residual strains in both ranges (I) and (II) were perfectly recovered by heating above  $A_f$ . This is the **shape memory effect**. The third range (III) includes curves (i)~(l) where  $A_f < T < T_c$  and  $T_c$  is the critical temperature where plastic deformation by slip (dislocation motion) starts. In this range, there is also a sharp bending at the yield point and a broad plateau as in region II, but the strain was fully recovered upon

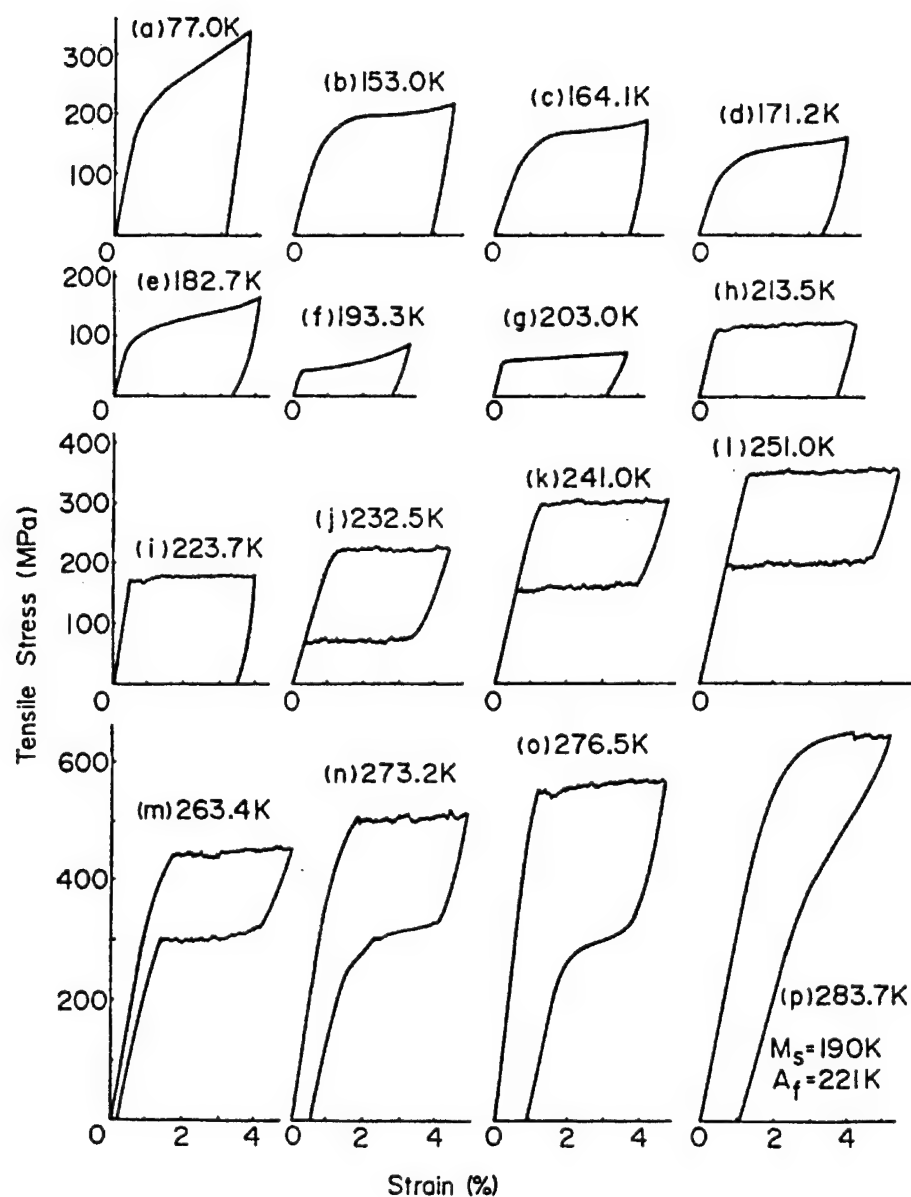


Figure 3.10 Stress-strain curves as a function of temperature for a Ti-50.6at%Ni alloy that was solution treated at 1273 K for 1 hour and subsequently quenched in ice water [Miyazaki *et al.* (1981)].



unloading. This has been attributed to the formation of SIM upon loading and its complete reversion to the parent B2 phase upon unloading. This is the **superelastic effect**. It has also been noted that with increasing temperature, the stress required to induce the transformation increases. This behavior has been described by the modified Clausius-Clapeyron equation

$$\frac{d\sigma_T}{dT} = \frac{\rho \cdot \Delta H}{\Delta\epsilon_T \cdot T_0}$$

where  $\sigma_T$  is the global stress,  $\rho$  is the alloy density,  $\Delta H$  is the heat of transformation,  $\Delta\epsilon_T$  is the global strain due to the transformation, measured from the maximum length of the initial plateau on the stress-strain curve, and  $T_0$  is where the martensite and parent phase are in equilibrium. There is still some dispute as to how to define  $T_0$ , but for thermoelastic transformations it has been suggested that  $T_0 = \frac{1}{2}(M_s + A_f)$  is most appropriate. The fourth range (IV) includes curves (m)~(p) for which  $T > T_c$ . In this temperature range, the curves deviate from linearity before the sharp bending at the yield point. This has been attributed to slip deformation, which can occur prior to the formation of SIM at high temperatures. In these tests some residual strain remained after unloading, because plastic deformation by slip is not recoverable.

### Compression

Although the tensile test is the most common method of evaluating the mechanical properties of NiTi alloys, it will not be used in this research. TiC-NiTi

composites are extremely difficult to machine, so they will be tested primarily in compression. It is important to mention that the mechanical response of NiTi in compression is very different from that measured in tension. Figure 3.11 shows the tension/compression hysteresis for Ti-50.8at%Ni samples tested at various temperatures [Plietsch *et al.* (1997)]. In Figure 3.11(a) the sample was tested above the maximum temperature at which martensite can be stress induced,  $M_d$ , so that the B2 structure was stable and remained untransformed throughout the experiment. The loading curve in tension is completely symmetrical to the loading curve in tension. In Figure 3.11(b) the sample was tested in the superelastic range. Upon loading the B2 transformed to oriented B19'. This loading curve shows pronounced asymmetry. The material has a higher modulus in compression than in tension. Also, the transformation strain in compression is approximately 50% lower than the strain in tension. In Figure 3.11(c) the sample was tested below  $M_s$ , so that the structure was in the B19' phase throughout the test. In this temperature regime the deformation was characterized by variant reorientation. This loading curve is also asymmetrical with a strain in compression that is only half the strain in tension.

The different mechanical responses in tension and compression result from the maximum transformation strains that can be accommodated by the martensite variants. Table 3.2 shows the transformation strains for each of the twelve variants along three different directions. For loading in the  $[111]_{B2}$  direction, Variants 4, 6, and 12 accommodate the largest strain in tension (+9.7%), while Variants 1, 3, 5, 7, 9, and 11 accommodate the largest strain in compression (-3.7%). For loading along the  $[100]_{B2}$

axis, the behavior is reversed. Maximum compressive strains (-4.2%) are larger than maximum tensile strains (+2.6%). However, when the ratio  $\epsilon_{\max, \text{tension}} / \epsilon_{\max, \text{compression}}$  is averaged over all orientations (as in a polycrystalline material), the tensile strains exceed the compressive strains by 50% [Plietsch *et al.* (1997)].

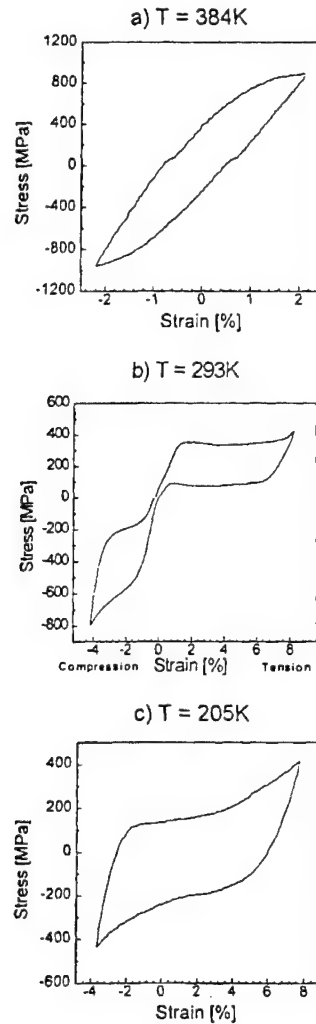


Figure 3.11 Tension/compression hysteresis for a Ti-50.8at% alloy in (a) the B2 structure, (b) the superelastic range, and (c) the B19' structure. The  $M_s$  temperature for this alloy is 268 K [Plietsch *et al.* (1997)].

## Bending

The composites synthesized in this project will be tested in bending, so it is useful to briefly consider the bending response of NiTi. Figure 3.12 shows the stress-strain curves of a 50.8at%Ni-Ti alloy subjected to 3-point, 4-point, and pure bending (free bending without intermediate loading points) [Wick *et al.* (1995)]. The 8% strain in bending was completely recovered upon unloading. In this work, the samples will be tested to failure, which is expected to occur at much smaller strains as a result of the brittle inclusions.

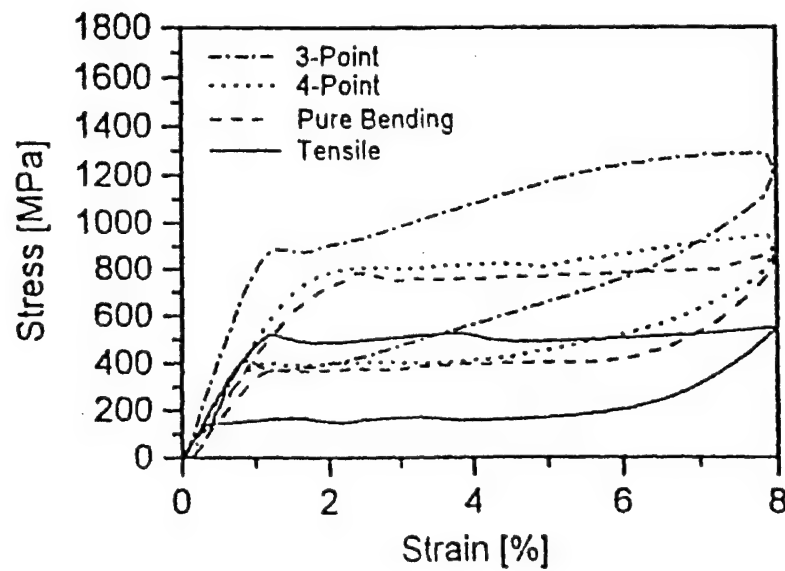


Figure 3.12 Stress-strain curves of a 50.8at%Ni-Ti alloy tested in three-point, four-point, pure bending and tension [Wick *et al.* (1995)].

## Fracture Toughness

One of the goals of this research is to tailor the chemistry and microstructure of the TiC-NiTi composites in order to maximize the fracture energy per unit volume. This requires studying the effect of martensitic transformation on the toughness of the material. Figure 3.13 shows the fracture toughness data (labeled E) obtained for three different NiTi alloys [Melton *et al.* (1981)]. Figures 3.13(a) and 3.13(b) record data for sharp notch tensile tests and Figure 3.13(c) records data for notched Charpy tests. The values of  $\sigma_{0.2}$ ,  $\sigma_P$ , and  $\sigma_{UTS}$  (defined in 3.13(d)) are also shown for comparison. The transformation temperatures are given in Table 3.3. The fracture toughness of each of the NiTi alloys has a minimum just below  $M_d$ , the maximum temperature at which martensite can be stress induced. This minimum has been attributed to the interaction between the slip process and the stress induced martensitic transformation. It has been proposed that the intersection of a growing martensite plate and a dislocation line could lead to a step on the martensite-parent interface and a kink in the dislocation. These steps and kinks would restrict the mobility of both the martensite plate and dislocation line on further straining. The presence of a toughness minimum underscores the importance of measuring and tailoring the transformation temperatures in the material. For maximum toughness, ambient temperature should not be near  $M_d$ . Also, for dynamic toughening (shown in 3.13(c)), it might be more effective to tailor the chemistry so that the material deforms by plastic flow rather than stress induced transformation.

Table 3.3. The nominal composition and transformation temperatures, determined by dilatometry, for the alloys in Figure 3.13 [Melton *et al.* (1981)].

Alloy	Nominal composition (wt.%)	Transformation temperatures ( $^{\circ}\text{C}$ )			
		$M_s$	$M_f$	$A_s$	$A_f$
2	54.8 Ni 45.2 Ti	20	-20	39	77
3	55.5 Ni 44.5 Ti	-30	-53	-12	0
5	49 Ni 44 Ti 5 Cu 2 Fe	-80	-106	-58	-31

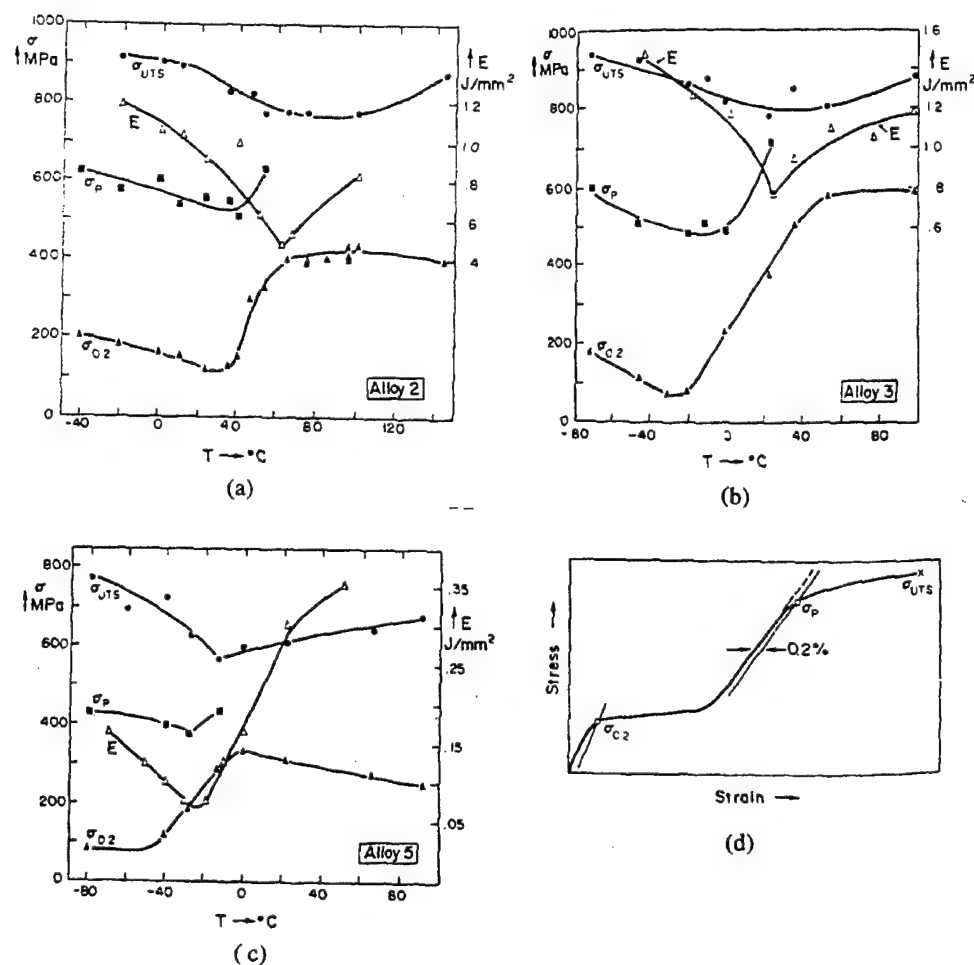


Figure 3.13. The fracture energy  $E$  along with  $\sigma_{0.2}$ ,  $\sigma_p$ , and  $\sigma_{UTS}$  for the different alloys in Table 3.3. In (a) and (b) the fracture energy is for sharp notch specimens. In (c) the fracture energy is for V-notch Charpy specimens. Figure (d) shows how  $\sigma_{0.2}$ ,  $\sigma_p$ , and  $\sigma_{UTS}$  are determined [Melton *et al.* (1981)].

## Strain Rate

Research on the structure-property relationships in TiC-NiTi composites is driven by interest in its application as an armor material. In contrast to the quasi-static test conditions described above (except in the Charpy tests), ballistic phenomena are characterized by large deformations and short times. Therefore, optimizing the properties of an armor material requires characterizing its response under conditions of high strain rate. Unfortunately, no high strain rate data for NiTi exists. The largest strain rate at which NiTi has been tested is  $10^{-2}$ /s. However, the effect of varying strain rate below ( $10^{-2}$ /sec) has been studied [Wu *et al.* (1996)].

Initial work on the effect of strain rate on the mechanical properties of shape memory alloys focused on the behavior of CuAlNi single crystals above  $M_s$  (Rodriguez *et al.* (1975)). Figure 3.14 shows the stress strain curves for CuAlNi tested at strain rates of 0.001/sec and 0.1/sec. In both experiments there was a delay after completion of loading before the specimen was unloaded in order to allow it to return to ambient temperature. The results show that the slope of the stress-strain curve (in the transforming region) was steeper at the higher strain rate. This was attributed to temperature changes within the specimen during testing. Figure 3.15 shows the thermal effect on loading and unloading CuAlNi single crystals at various strain rates [Rodriguez *et al.* (1975)]. At lower strain rates the measured temperature increase is smaller since there is more time available for the heat to be conducted away from the sample.

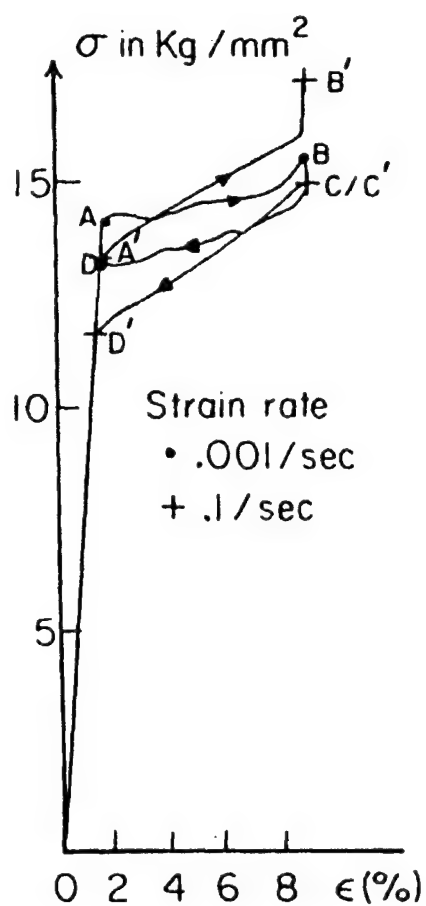


Figure 3.14 Stress-strain curves for CuAlNi single crystals tested at strain rates of 0.001 and 0.1/sec. The specimens were allowed to cool down between loading and unloading. The material was initially at 24 °C (23 °C above  $M_s$ ) [Rodriguez *et al.* (1975)].



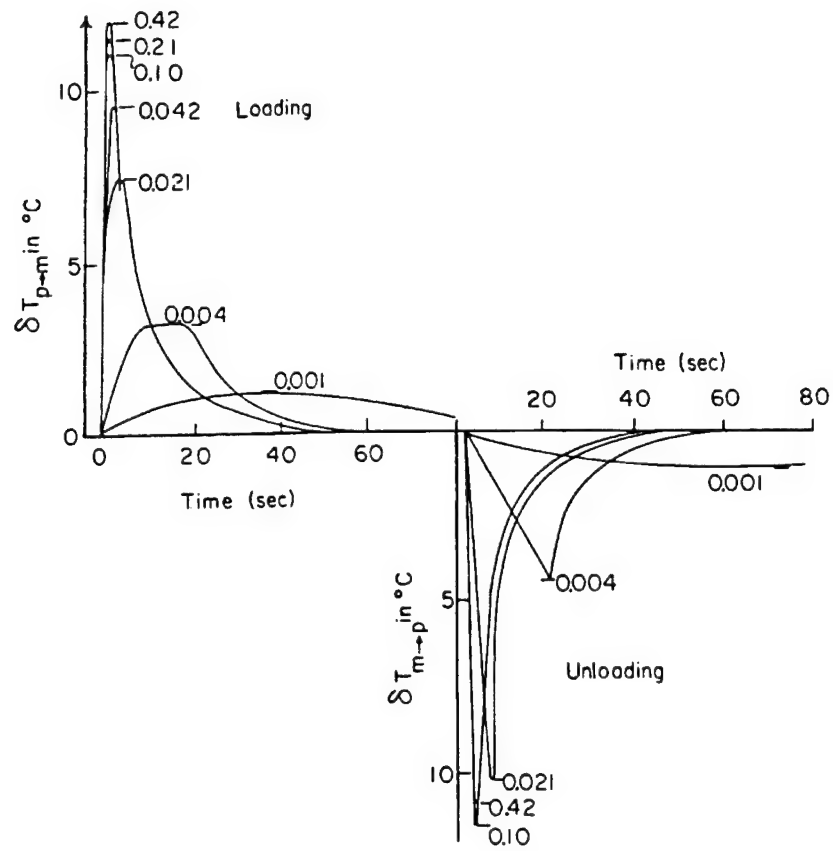


Figure 3.15 The thermal effect on loading and unloading CuAlNi single crystals at various strain rates. The initial temperature was 24  $^{\circ}\text{C}$  (23  $^{\circ}\text{C}$  above  $M_s$ ) [Rodriguez *et al.* (1975)].

The temperature changes during loading and unloading of shape memory alloys result from the heat of transformation  $\Delta H$ . The exothermic heat that is released during the parent to martensite transformation increases the sample temperature upon loading and the endothermic heat that is absorbed during the reverse transformation lowers the sample temperature upon unloading. The maximum temperature change in the sample is given by  $\delta T = \frac{\Delta H}{c}$ , where  $c$  is the specific heat of the martensite for the forward transformation or the specific heat of the parent B2 for the reverse transformation.

For samples tested at high strain rates, there is less time for  $\Delta H$  to be conducted away, so the resulting temperature increase is greater. This increase in sample temperature decreases the chemical driving force for the forward transformation. More nonchemical energy is required. Consequently, as the sample gets progressively warmer, the stress necessary for continued growth of the martensite progressively increases.

Similar strain rate effects in NiTi alloys have been reported [Jacobus *et al.* (1996)], which are also thought to be the result of temperature changes during loading and unloading. A model based on heat transfer has been developed in an attempt to correlate the observed strain rate effect with thermal effects [Wu *et al.* (1996)]. The temperature change at a given strain rate is calculated from conservation of energy:

$$\frac{1}{2} \left( \frac{d\varepsilon}{dt} \right) \sigma \pi r^2 l_o dt + \left( \frac{d\varepsilon}{dt} \right) dt \pi r^2 l_o \rho \frac{\Delta H}{\varepsilon_M} - 2h \pi r l_o (T - T_o) dt = C_p \pi r^2 l_o \rho \Delta T$$

The first term on the left hand side is the energy induced by the applied stress, the second term is the energy involved in the phase transformation, and the third term is the energy exchange that occurs between the sample and the surrounding environment. The term on the right-hand side is the energy that is released (or stored) by the material as a result of the temperature change. The variables in the equation are defined as follows:  $r$  is the radius of the wire,  $l_o$  is the length,  $\varepsilon_M$  is the maximum length of the plateau in the stress strain curve, and  $h$  is the convection coefficient. The temperature changes predicted by this equation can then be substituted into the Clausius Clapeyron equation in order to generate a theoretical stress strain curve. Figure 3.16 compares the theoretical and experimental stress strain curves for NiTi [Wu *et al.* (1996)]. It must be emphasized that the theoretical curves are not determined independently from the experimental curves. The value of  $\varepsilon_M$  used to predict the material temperature must be taken from the experimentally measured stress strain curve. The theoretical stress strain curve is only used as a tool to correlate the observed strain rate effect with the increase in sample temperature.

In order to determine if there is any intrinsic effect of strain rate on the martensitic transformation, tests have been performed in a liquid environment [Wu *et al.* (1996)]. The liquid environment was used to accelerate the heat transfer between the samples and the surroundings, so that sample temperatures would remain relatively constant. In these experiments, there did not appear to be any change in the mechanical response for strain rates varying between  $10^{-4}$  and  $10^{-2}$ /sec.

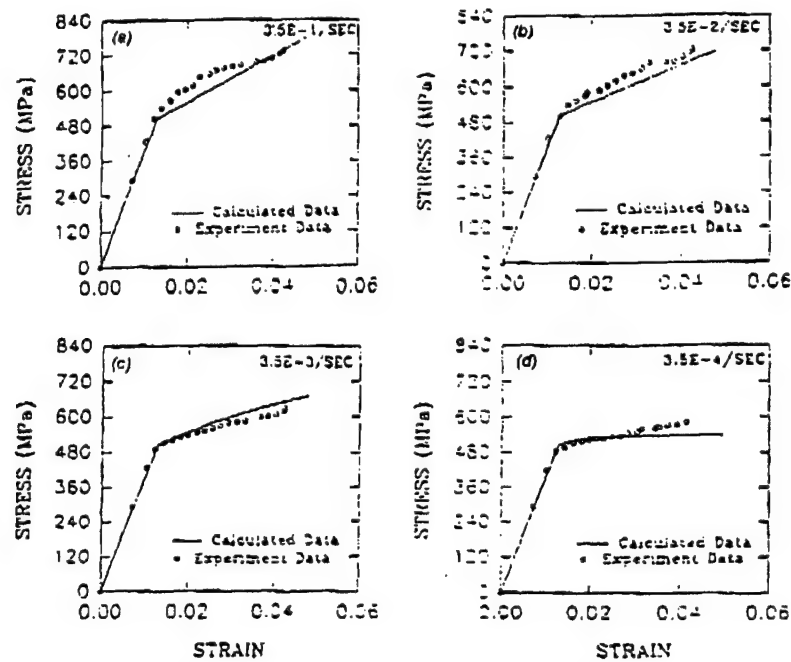


Figure 3.16 Comparison of calculated and experimental stress-strain curves for NiTi [Wu *et al.* (1996)]

In this research, the mechanical response of TiC-NiTi composites will be studied in air, because the armor will be used for land or air based vehicles. It is expected that the stress strain responses of these composites will depend on strain rate, if the NiTi matrix transforms in response to the applied load.

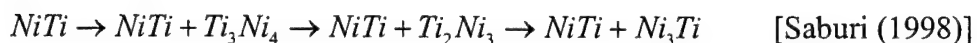
### 3.6 Strengthening Mechanisms in NiTi

In NiTi, deformation by slip is a competing process with stress induced martensitic transformation. Slip introduces nonrecoverable strain that limits the extent

of the shape memory and superelastic effects. In order to increase the resistance to slip in NiTi alloys, two techniques are used. Heat treatment is used in Ni-rich NiTi alloys. Thermo-mechanical treatment is used in near-equiatomic NiTi alloys.

### Heat Treatment

As mentioned earlier, the range of composition for the B2 phase field is very narrow below 923 K. Consequently NiTi alloys having a nickel content in excess of 50.5at% will decompose either upon slow cooling or upon aging at a temperature below 973 K after quenching from a high temperature. Figure 3.17 shows the time-temperature-transformation curves for a Ti-52.0at%Ni alloy [Nishida *et al.* (1986)]. The phase  $T_{11}Ni_{14}$  is stoichiometrically similar to  $Ti_3Ni_4$ , so that the decomposition sequence for aging below 953 K is now quoted as



The final products correspond to the equilibrium phase diagram, but the decomposition involves formation of metastable phases. The  $Ti_3Ni_4$  phase is a metastable phase that forms in the early stages of aging. It precipitates as fine lenticular platelets that are coherent with the B2 matrix. Figure 3.18 shows a transmission electron micrograph of  $Ti_3Ni_4$  precipitates formed in Ti-51.3at%Ni alloy aged at 500 °C [Saburi *et al.* (1982,1989)]. As this phase grows, it distorts the B2 lattice and hinders the movement of dislocations. This strengthens the B2 matrix by raising the flow stress for slip. The precipitation of  $Ti_3Ni_4$  also increases the  $M_s$

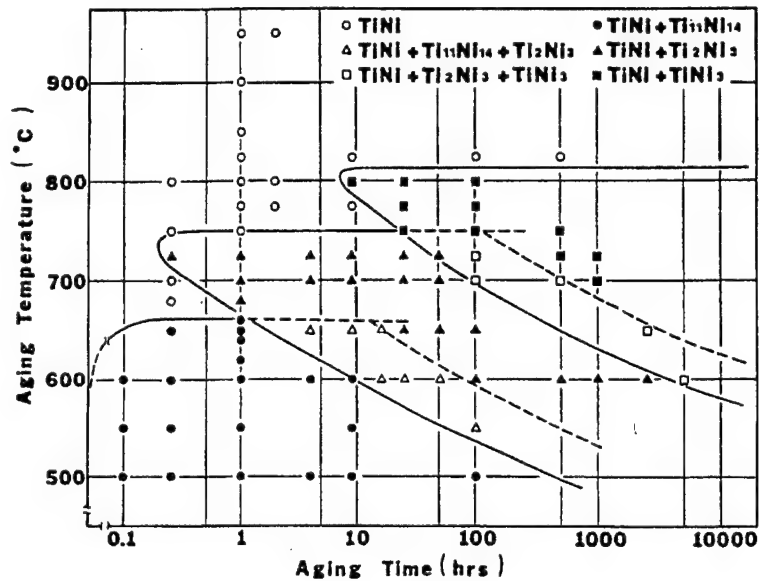


Figure 3.17 Time-temperature-transformation curves for a Ti-50.2at%Ni alloy [Nishida *et al.* (1986)].

by shifting the nickel content of the matrix towards the stoichiometric composition. Increasing  $M_s$  effectively lowers the stress required to initiate the transformation. This helps to ensure that SIM formation occurs before slip. Heat treatments for Ni-rich NiTi alloys are designed to precipitate and retain  $Ti_3Ni_4$  at room temperature. Typically this involves aging at temperatures between 573 K and 773 K for one hour followed by quenching into ice water [Saburi *et al.* (1982), Miyazaki *et al.* (1982, 1986a)].

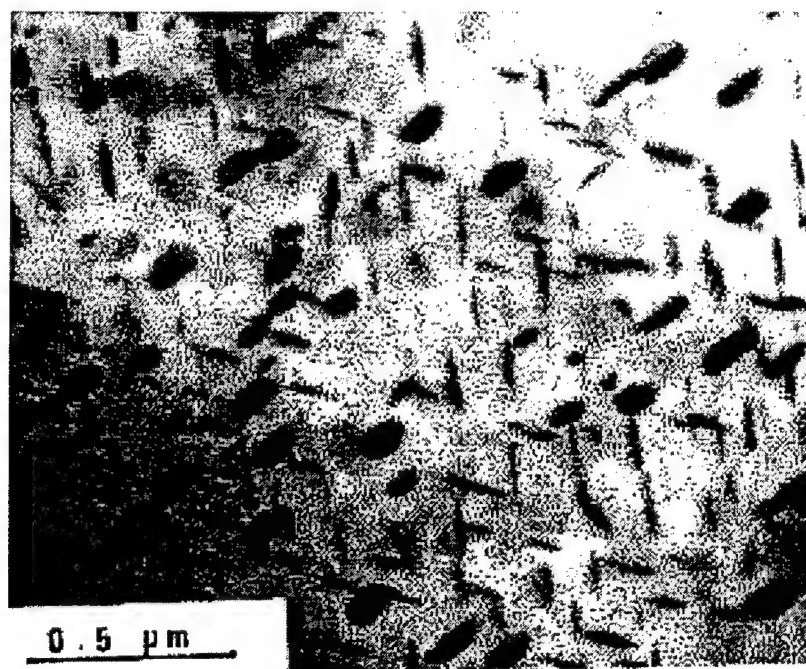


Figure 3.18 Transmission electron micrograph of  $\text{Ti}_3\text{Ni}_4$  precipitates in Ti-51.3at%Ni alloy aged at 500 °C [Saburi *et al.* (1982, 1989)].

### Thermo-Mechanical Treatment

Unlike nickel rich NiTi alloys, those of near-equiatomic composition are not sensitive to heat treatment and cannot be precipitation hardened by formation of  $\text{Ti}_3\text{Ni}_4$ . These alloys are hardened by thermo-mechanical treatment, i.e. cold work followed by annealing [Miyazaki *et al.* (1982, 1986a), Saburi *et al.* (1986)]. Cold work results in the generation of a large number of dislocations that eventually become tangled and resist dislocation movement (slip). Subsequent annealing below the recrystallization temperature reduces residual stresses created during cold work by facilitating dislocation rearrangement within the deformation structure. Thermo-mechanical treatment is probably not feasible for strengthening the NiTi matrix in TiC-NiTi composites, because the ceramic inclusions have high hardness and low ductility which make cold working difficult.



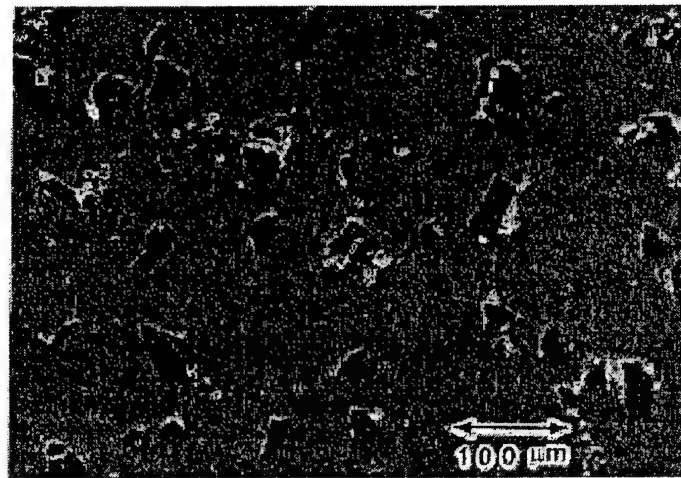
## IV. Background: TiC-NiTi Composites

TiC-NiTi systems are useful because they provide an opportunity to study how internal stresses affect the martensitic transformation. The internal stresses result from the shape mismatch that occurs between the matrix and reinforcement during thermal excursion, phase transformation, or external loading.

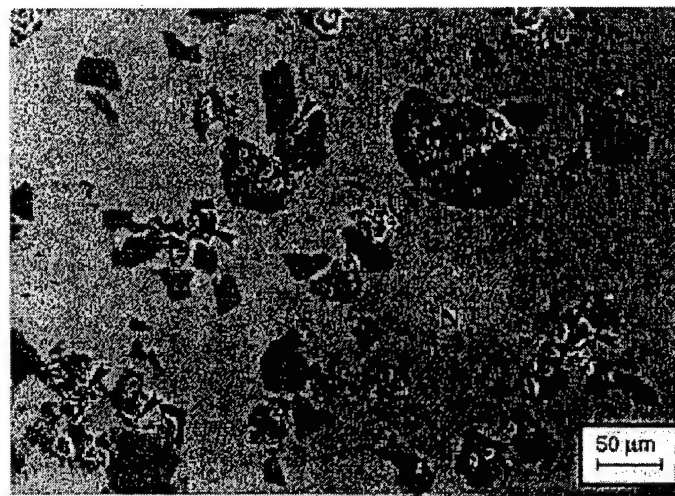
### 4.1 Microstructure

Figure 4.1 shows the microstructure of (a) 10vol%TiC-NiTi [Mari *et al.* (1995a)] and (b) 20vol% TiC-NiTi [Dunand *et al.* (1996)] composites formed by vacuum hot pressing. The TiC particles are irregularly shaped with an average particle size that corresponds closely to the reactant particle size (40  $\mu m$  in (a) and between 40-100  $\mu m$  in (b)). Pores appear both within the TiC particles and the matrix. Figure 4.2(a) shows the microstructure of etched 10vol%TiC-NiTi [Fukami-Ushiro *et al.* (1996a)] in which a large TiC particle is surrounded by several NiTi particles. The original powder particles in the matrix are still visible because contaminants on the surface of the starting powders remain in the product. This contamination is also shown in Figure 4.2(b) (see arrows). In this research, these microstructures obtained by vacuum hot pressing were compared to the microstructures of composites synthesized by SHS. Differences in (1) TiC particle size, morphology, and distribution, (2) pore size and distribution, and (3) NiTi texture

were evaluated.

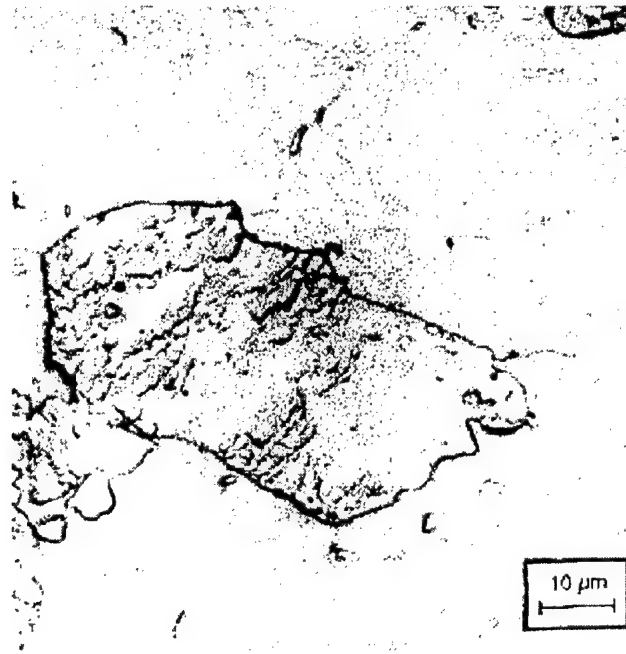


(a)

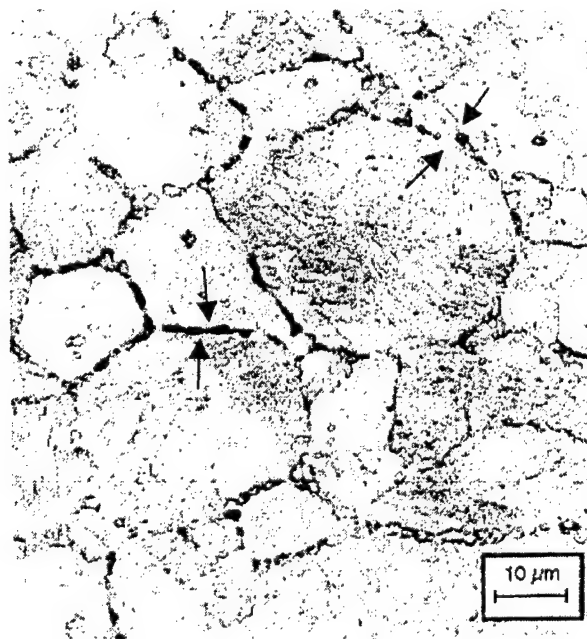


(b)

Figure 4.1 Microstructure of vacuum hot pressed TiC-NiTi composites. (a) 10 vol%TiC-NiTi [Mari *et al.* (1995a)], (b) 20 vol%TiC-NiTi [Dunand *et al.* (1996)].



(a)



(b)

Figure 4.2 Microstructure of (a) etched 10vol%TiC-NiTi, showing large TiC particle surrounded by NiTi particles, (b) etched NiTi showing prior surfaces of metallic powder [Fukami-Ushiro *et al.* (1996a)].

## 4.2 Effects of Thermal Excursion

Differential scanning calorimetry has been used to study the effects of TiC inclusions on the NiTi martensitic transformation during thermal excursion. Figure 4.3 shows the calorimetry spectra for the first thermal cycle of TiC-NiTi composites with a matrix composition of 51.4at%Ti-Ni [Mari *et al.* (1995a)]. The spectra are plotted in terms of heat capacity, instead of heat flow, so the forward martensitic transformation (occurring upon cooling) is represented by a downward departure from the baseline, and the reverse transformation (occurring during heating) is represented by an upward departure from the baseline. The transformation temperatures  $M_f$  and  $A_s$  decrease as the TiC particle content increases, while  $M_s$  and  $A_f$  are independent of particle content.

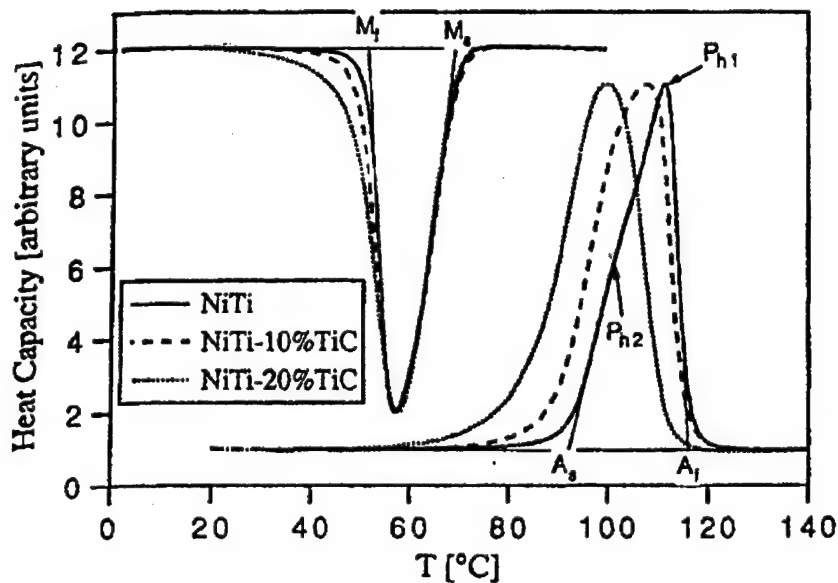


Figure 4.3 Calorimetry spectra for the first thermal cycle of TiC-NiTi composites with a matrix composition of 51.4at%Ti-Ni (scanning rate: 20 K/min) [Mari *et al.* (1995a)].

Since the temperature interval ( $M_s$ - $M_f$ ) over which the martensitic transformation occurs depends on the stored elastic energy [Salzbrenner and Cohen (1979)], the lowering of  $M_f$  with increasing particle content is thought to be the result of an increase in the stored elastic energy around the martensite. It has been proposed that the TiC particles effectively introduce internal stresses in the matrix, which oppose the propagation of the martensite. Additional chemical energy (cooling) is required in order to continue the  $B2 \rightarrow B19'$  transformation. This additional energy is stored during the forward transformation, and subsequently promotes the reverse transformation. Not as much chemical energy is necessary to drive the  $B19' \rightarrow B2$  transformation, so  $A_s$  is lowered [Mari *et al.* (1995a,b)].

In contrast to  $M_f$  and  $A_s$ , the martensite start temperature  $M_s$  is independent of particle content. This suggests that the TiC particles only affect martensite growth, not nucleation.

Calorimetry has also been used to study the effects of TiC particles on R phase formation after thermal cycling between  $-10^\circ\text{C}$  to  $170^\circ\text{C}$  [Mari *et al.* (1995a)]. Figure 5.4 shows the calorimetry spectra for the 100<sup>th</sup> cycle. All of the transformation temperatures have decreased. Also, the width of the forward transformation has increased, while the width of the reverse transformation has decreased. Most notably, the forward transformation peak of unreinforced NiTi has developed a more complex shape characterized by the appearance of peaks  $P_{c2}$  and  $P_{c3}$  on either side of the main peak.

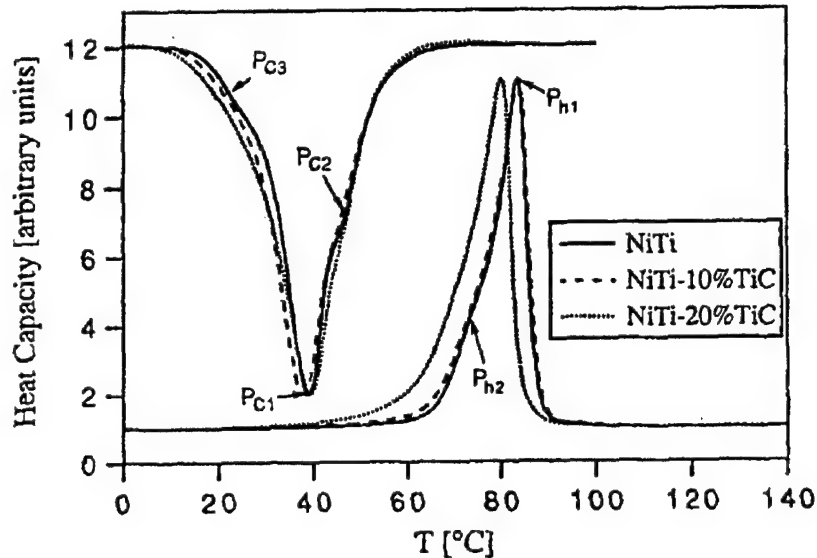


Figure 4.4 Calorimetry spectra for the 100<sup>th</sup> cycle of TiC-NiTi composites with a matrix composition of 51.4at%Ti-Ni (scanning rate: 20 K/min) [Mari *et al.* (1995a)].

The decrease in all the transformation temperatures for both unreinforced and reinforced NiTi after thermal cycling has been attributed to dislocation formation. Dislocations create a backstress around nucleating and growing B19' martensite plates. This backstress increases the chemical energy necessary to drive the forward transformation and decreases the chemical energy necessary to drive the reverse transformation.

The additional peaks superimposed on the main forward transformation peak for unreinforced NiTi have been attributed to the appearance of the R phase. Thermal cycling lowers the  $M_s$  temperature for the B2  $\rightarrow$  B19' transformation. Upon repeated cycling the  $M_s$  temperature is lowered below the  $R_s$  temperature. The temperature range of the R-phase stability is broadened, so that the transformation proceeds in multiple steps, B2  $\rightarrow$  R  $\rightarrow$  B19' [Mari *et al.* (1995a)].

The absence of additional peaks in the calorimetry spectra for TiC reinforced NiTi suggests that the carbide particles inhibit the R-phase transformation. This result was surprising, because it was originally expected that the misfit elastic stresses from the TiC would serve as nucleation sites for the R-phase. Since the R-phase is a rhombohedral distortion of the cubic lattice and is characterized by an elongation along the  $\langle 111 \rangle_{B2}$ , its nucleation should be favored by a tensile stress in that direction. On further analysis, Mari and Dunand (1995a) calculated that the stress field around ellipsoidal TiC particles is isostatic tensile with no preferred component along the  $\langle 111 \rangle_{B2}$  direction. Therefore, TiC should have little influence on the R-phase transformation.

In order to explain the suppression of the R-phase transformation in TiC-NiTi composites, Mari and Dunand (1995a) proposed that the TiC particles pin the dislocations that are generated during the repeated transformation. This pinning of dislocations results in a slower decrease in the  $M_s$  temperature during thermal cycling, so that the separation of the  $M_s$  and  $R_s$  temperatures is not as great as in unreinforced NiTi. Consequently, the temperature range for R-phase stability is smaller in the composites.

Unfortunately, the work by Mari and Dunand (1995a) was not accompanied by any electron microscopy. No observations of the R-phase transformation, B19' phase transformation, or their interactions with carbide particles and/or dislocations were made. In this work, the TiC-NiTi composites were thermally cycled in the TEM in order to study the effect of TiC inclusions on the martensitic phase transformations.

### 4.3 Effects of Mechanical Deformation

The effect of increasing TiC particle content on the mechanical behavior of TiC-NiTi composites has been studied by compressive loading [Fukami-Ushiro *et al.* (1996a)]. The stress-strain curves for composites tested at  $T_d = A_f + 5$  K and  $T_d = M_s + 5$  K are shown in Figures 4.5 and 4.6, respectively. All curves are characterized by a positive curvature after yielding and a positive curvature during unloading. These features have been attributed to the stress induced martensitic transformation. The transformation yield stress  $\sigma_{trans}$  decreases with decreasing temperature as expected by the modified Clausius-Clapeyron equation. Also, at each particular temperature,  $\sigma_{trans}$  increases with increasing TiC content, and the yield stress for slip  $\sigma_p$  decreases with increasing TiC content.

The increase in transformation yield stress with increasing particle content is thought to be due, in part, to elastic load transfer between the compliant NiTi matrix and the TiC reinforcement. The proportion of the external load borne by each of the constituents depends on volume fraction, shape, and orientation of the reinforcement and on the elastic properties of both the constituents. Since TiC particles are relatively stiff and they tend to deform less than the surrounding matrix, they should bear a relatively high proportion of the load and strengthen the composite. However, calculations show that the increase in transformation yield stress with increasing particle content is larger than predicted by Eshelby's load transfer theory. It is thought that dislocations are created at stress concentration points to relax the mismatch stresses and strains between the NiTi matrix and the TiC inclusions. These



dislocations stabilize the B2 matrix and inhibit the  $B2 \rightarrow B19'$  transformation by preventing the motion of interfaces. The greater the concentration of TiC particles, the greater the number of dislocations to inhibit the transformation, so the higher the yield stress for the transformation. Since the TiC-NiTi composites are expected to have regions of untransformed B2 within the matrix, and the B2 phase is weaker than the B19' phase, the yield stress for slip  $\sigma_p$  is expected to be lower in the composites [Fukami-Ushiro *et al.* (1996a)].

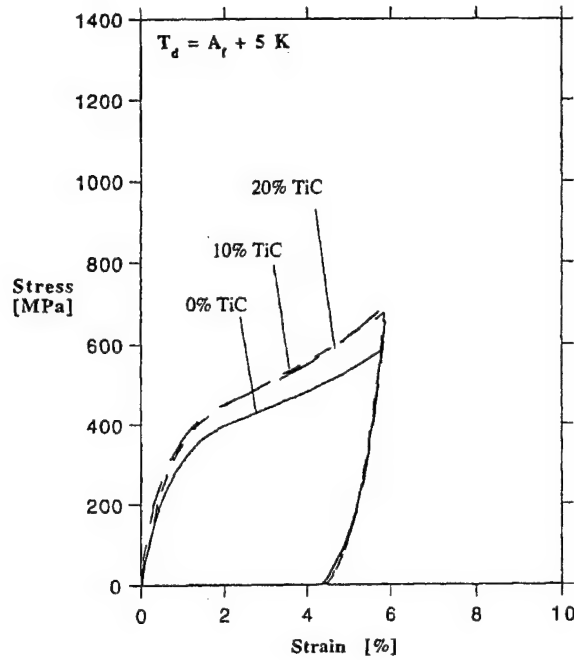


Figure 4.5 Stress-strain curves of TiC-NiTi composites tested at  $T_d = A_f + 5$  K after cooling from  $A_f + 20$  K [Fukami-Ushiro *et al.* (1996a)].

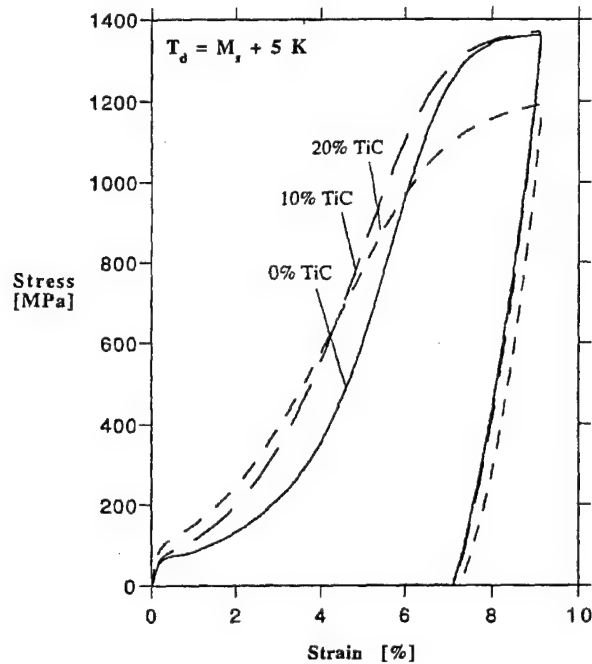


Figure 4.6 Stress-strain curves of TiC-NiTi composites tested at  $T_d = M_s + 5$  K after cooling from  $A_f + 20$  K [Fukami-Ushiro *et al.* (1996a)].

Figure 4.7 shows the stress-strain curves for TiC-NiTi composites tested below  $M_f$ . Since all samples were in the B19' phase during the deformation, the yielding behavior is the result of variant reorientation. The variants that accommodate the maximum strain in the direction of the applied load grow by twinning at the expense of the other variants. The twinning yield stress  $\sigma_{\text{twin}}$  appears to be independent of particle content. This disagrees with the calculations based on Eshelby load transfer theory, which predict that the twinning yield stress  $\sigma_{\text{twin}}$  should increase with increasing particle content. It is thought that the shape mismatch between the matrix and reinforcement is relaxed by localized twinning at the interface between the matrix and reinforcement. Then, at higher strains, dislocations are created to relax the mismatch. These dislocations prevent martensite twinning, thereby strengthening the matrix when twinning is the main deformation mechanism [Fukami-Ushiro *et al.* (1996a)].

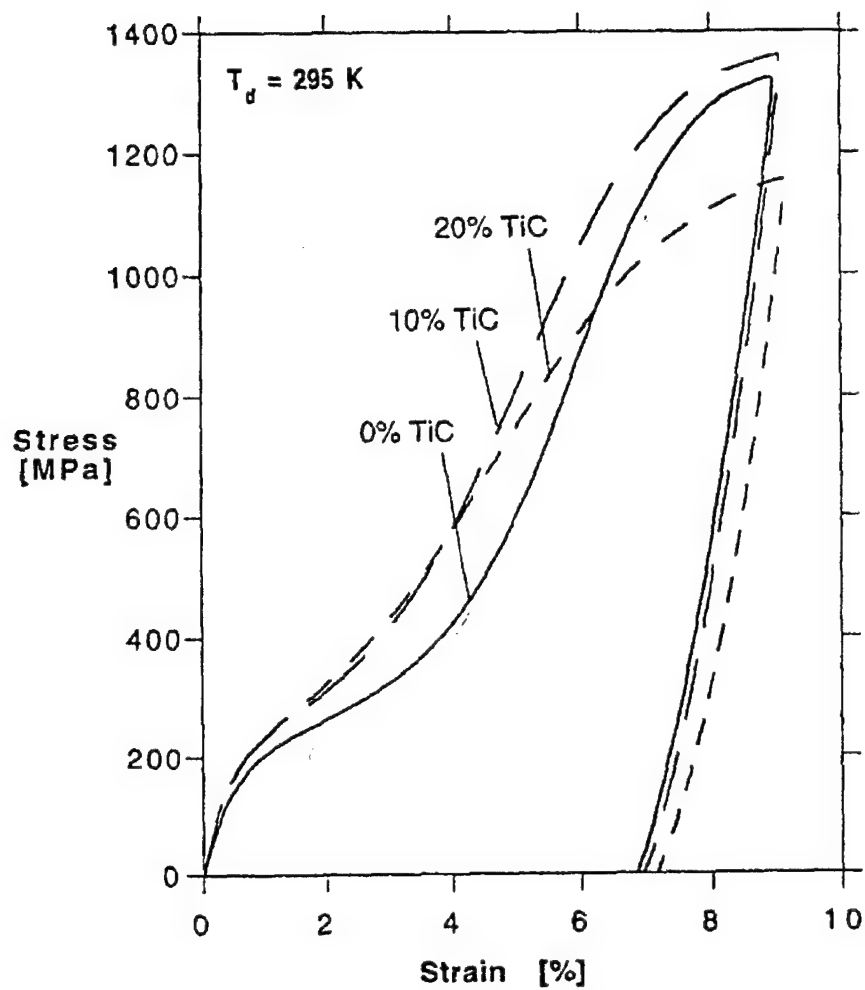


Figure 4.7 Stress-strain curves of TiC-NiTi composites tested at room temperature (below  $M_f$ ) [Fukami-Ushiro *et al.* (1996a)].

## V. Background: Processing

Previous work on the TiC-NiTi system has primarily focused on characterizing the properties of composites formed by conventional powder processing techniques. These techniques are listed in Table 5.1. Most of these methods require operation of high cost equipment for long times, in order to drive the complete conversion from reactants to products.

Table 5.1 Conventional methods used to synthesize TiC-NiTi composites.

	Method
Goldstein (1977)	Infiltration of porous carbon by a Ti-rich Ni-Ti alloy, followed by heating to provide solid state conversion of carbon into TiC
Poletika <i>et al.</i> (1983) Kul'kov <i>et al.</i> (1984) Akimov <i>et al.</i> (1986)	Sintering for 1 hour at 1300 °C or 1250-1280 °C
Panin <i>et al.</i> (1985)	Explosive pressing, followed by sintering for 1 hour at 1000-1350 °C
Goldstein (1992)	A sequence of CIPing at 680 MPa, sealing in a steel container evacuated to less than 100 microns, sintering between 900 °C and 1195 °C, followed by hot working to reduce the cross sectional by at least 25%
Mari <i>et al.</i> (1995a,b)	Vacuum hot pressing for 3.5 hours at 1150 °C and 25 MPa
Fukami-Ushiro <i>et al.</i> (1996a,b)	Vacuum hot pressing for 4-6 hours at 1080 °C and 65-75 MPa, followed by HIPing for 2 hours at 1160 °C and 172 MPa
Dunand <i>et al.</i> (1996)	Vacuum hot pressing for 5.25-5.5 hours at 1080 °C at 22-27 MPa, followed by HIPing for 2 hours at 1160 °C and 172 MPa

An alternative, more energy efficient processing method, known as combustion synthesis or self-propagating high temperature synthesis (SHS) has been used by A.N. Tabachenko and G.G. Kryuchkova (1993) to produce TiC-NiTi composites. In this work, SHS was combined with a post reaction densification technique, called Quasi-Isostatic Pressing, to produce TiC-NiTi composites with low residual porosity.

## 5.1 SHS

SHS uses the energy of the exothermic reaction between elemental metal and nonmetal (e.g. Ti+Ni+C) powders to sustain the reaction as a combustion wave. Figure 5.1 shows the simplicity of the process. An external energy source is only needed to initiate the reaction locally. Once ignited, the reaction itself produces sufficient energy to preheat the reactant powder ahead of the wave front to the ignition temperature. When the temperature of this powder reaches the ignition temperature, it also begins to react and generate heat, which is conducted further down the compact. SHS is simply a process of repeated ignition, reaction, and heat conduction [Munir *et al.* (1989), Merzhanov (1990), Moore *et al.* (1995a,b)].

In SHS, the high temperatures evolved during the exothermic reaction drive the propagation of the combustion wave. It has been determined empirically that the adiabatic temperature  $T_{ad}$  must be greater than 1800 K for an exothermic reaction to become self-sustaining equation [Novikov *et al.* (1975)]. Consequently, calculation of the adiabatic temperature is useful for predicting whether or not this process can be used to form a particular compound. The adiabatic temperature is calculated by

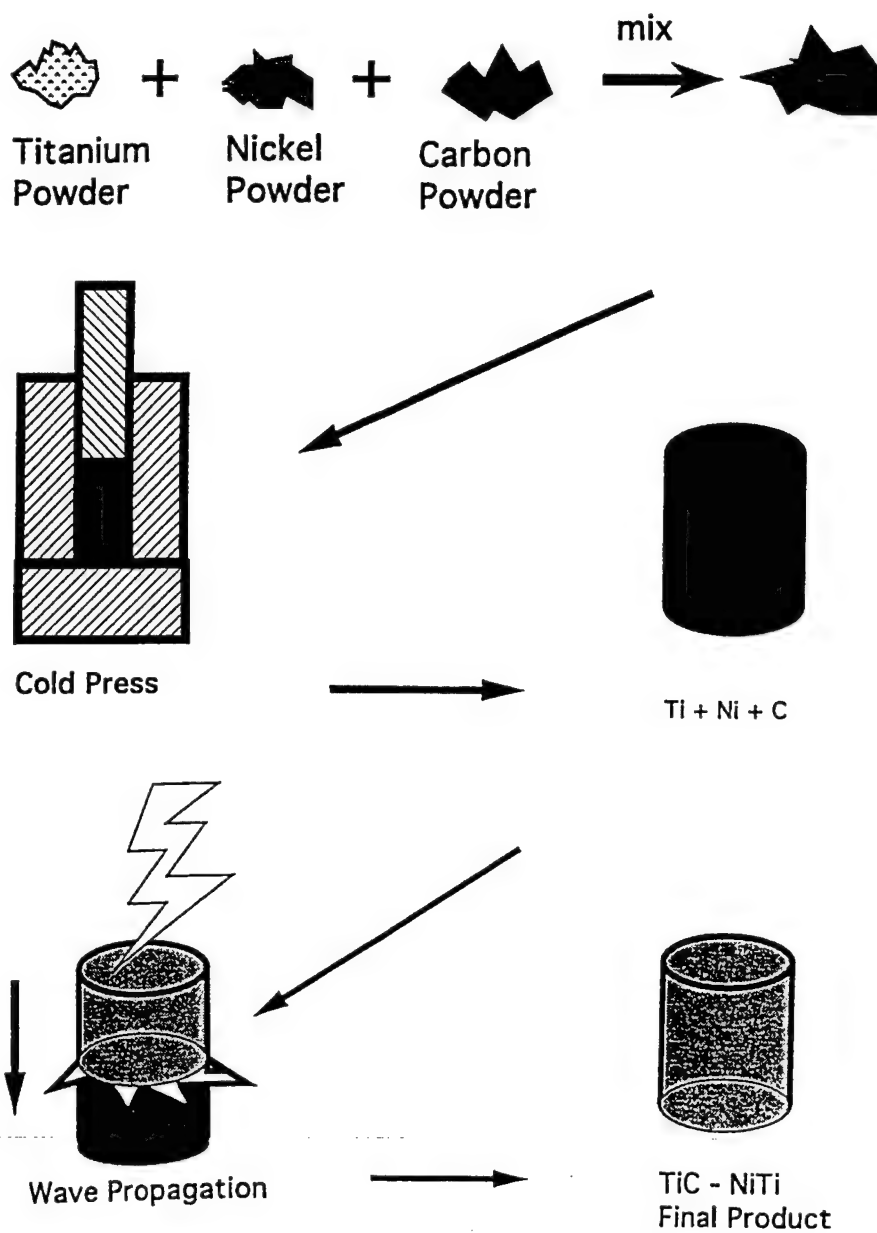


Figure 5.1 Processing steps during Self-Propagating High Temperature Synthesis (SHS) of TiC-NiTi composites. .

assuming conservation of energy. All the energy that is released by formation of the compound ( $\Delta H_{f,298}(\text{TiC}) = -184.5 \text{ kJ/mol}$  and  $\Delta H_{f,298}(\text{NiTi}) = -67.8 \text{ kJ/mol}$  [Barin (1995)]) goes to heating the product phase. The adiabatic temperature depends on the initial temperature, so weakly exothermic reactions can be made to self propagate by heating them. For systems, such as the TiC-NiTi system, where there is a product with a low melting temperature, some of the heat released during the reaction goes into driving the phase transformation, i.e. melting of the NiTi. This phase transformation must be included in the equation. In this work, the adiabatic temperatures for the TiC-NiTi system have been calculated as a function of volume fraction of NiTi. These calculations, although neglecting heat losses to the environment, provide an upper bound to the system temperature and to the volume fraction of liquid formed. This is useful for optimizing processing parameters, such as the delay time before loading.

The high temperatures evolved during SHS produce a self-purifying effect in the material by driving off volatile impurities. Consequently the purity of the products formed by SHS is not limited by the purity of the reactants. This is not the case for TiC-NiTi composites formed by sintering or hot pressing, where contaminants on the surface of the starting powders remain in the product [Fukami-Ushiro *et al.* (1996a)].

SHS is also a rapid processing technique. Combustion wave velocities as high as 1 cm/sec have been reported in the TiC-40vol%NiTi system [Tabachenko *et al.* (1993)], which means complete conversion from reactants to products can be expected



on a time-scale of seconds. This is significantly shorter than the processing times required for other synthesis techniques.

The differences between sintering and SHS extend beyond issues of cost, energy efficiency, time and product purity. The mechanisms of product formation by these two techniques are the result of fundamentally distinct thermodynamic processes, which lead to the evolution of different microstructures. Sintering of TiC-NiTi composites involves the bonding of TiC and NiTi powders. It is driven by the decrease in surface free energy that occurs with the formation of interparticle necks and bonds. Sintering does not involve chemical reaction, only mass transfer. Therefore, the TiC particle size in TiC-NiTi composites formed by sintering is determined by the initial powder particle size. In contrast, SHS of TiC-NiTi composites involves the exothermic reaction between Ti+C+Ni powders. The reaction is driven by the decrease in chemical free energy between the reactants and the products. The heat evolved during the reaction melts the Ti and Ni powders, so that the microstructure of TiC-NiTi composites is independent of the initial powder particle size. Instead, the structure is determined by the parameters of the combustion and post-combustion zones, such as temperature and rate of cooling.

The mechanism of TiC formation during SHS of TiC-Ni systems has been studied by quenching experiments using a copper cylinder with a tapered hole [LaSalvia *et al.* (1995a,b)]. Such quenching experiments create a range of cooling rates up to  $10^4$  K/sec, which allows subsequent characterization of the physical processes occurring at the reaction front. Figure 5.2 is a schematic illustration of the reaction process in the TiC-Ni system [LaSalvia *et al.* (1995b)]. The first stage (a)

involves the Ni and Ti melt formation, homogenization, and capillary spreading around the C particles. After the melt becomes saturated by carbon, a layer of carbide forms by nucleation and growth on the surface of the C particles (Figure b). The layer subsequently breaks up into TiC spherules, and another layer of carbide begins to form on the re-exposed C particle surface. (Figure c). The process of continuous formation and break up of TiC spherules proceeds until the residual carbon particle size is on the same order as the TiC layer thickness. Then, the TiC spherules don't break off until the carbon particle is fully reacted (Figure d). Eventually the TiC chain separates into individual spherules and the particles continue to grow by Ostwald ripening (Figure e).

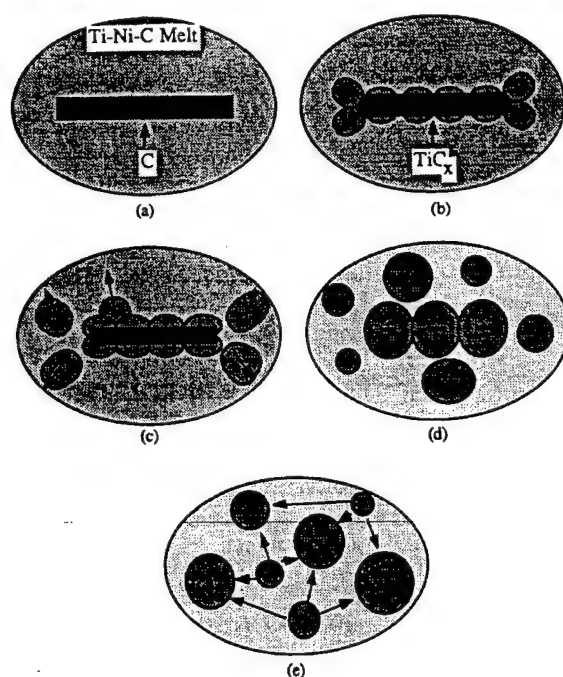


Figure 5.2 Sequence of formation of  $\text{TiC}_x$  during SHS process. (a) Ni-Ti melt formation, homogenization and capillary spreading around carbon particles. (b) Nucleation and growth of  $\text{TiC}_x$  grains. (c) Continued growth and separation of  $\text{TiC}_x$  spherules. (d) Formation of  $\text{TiC}_x$  chain. (e) Separation of chain into individual  $\text{TiC}_x$  spherules which continue to grow by Ostwald ripening [LaSalvia *et al.* 1995b)]

It is expected that the process of TiC particle formation in TiC-NiTi composites produced by SHS is similar to the mechanism described above for TiC formation in TiC-Ni systems.

## 5.2 Densification

The products of SHS are typically very porous, because escaping gases create channels through the newly formed material. The porosity formed during SHS can be reduced, or eliminated, by the application of a mechanical load while the product is still at a high enough temperature to sustain material flow without brittle failure. Examples of techniques include hot pressing, extrusion, rolling, and impact forging. In Japan, commercial NiTi alloys are produced by combining SHS with hot isostatic pressing [Kaieda *et al.* (1987)]. One of the simplest and least expensive methods of consolidation involves surrounding the hot porous material in a bed of granular particulate before application of a uniaxial load. Figure 5.3 shows a schematic illustration of the configuration. The graphite or graphite/alumina particulate acts as a pressure-transmitting medium that provides lateral confinement and redistributes the applied axial load. The simplicity of this method, patented by Ceracon [Lichti *et al.* (1985)], and known as the Quasi-Isostatic Pressing (QIP), allows the capability of combining the synthesis and densification sequence into a one step process [Raman *et al.* (1995)]. The sample can be ignited within the graphite particulate and densified immediately after passage of the combustion wave.

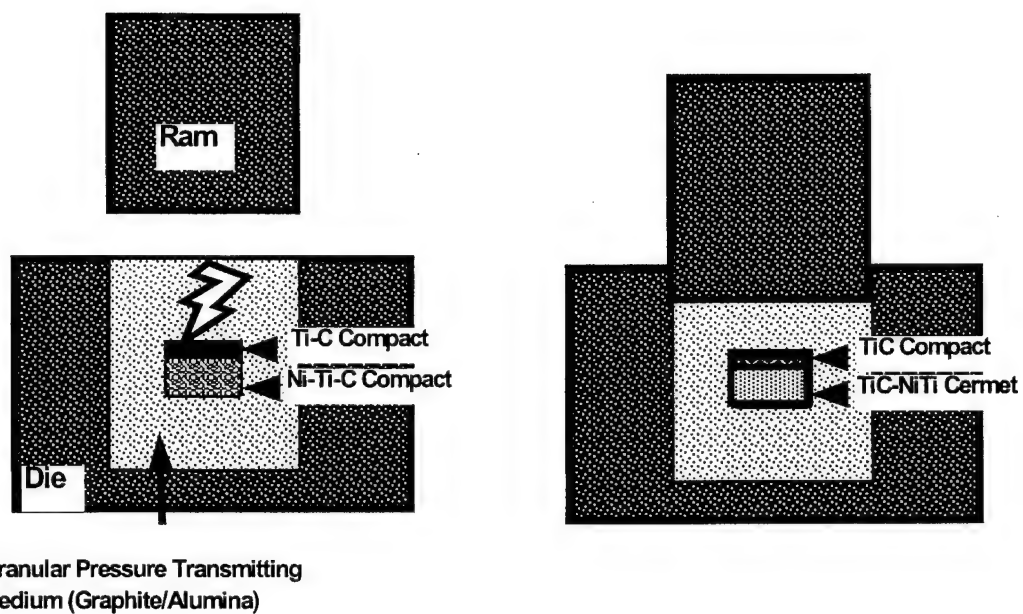


Figure 5.3 Schematic illustration of Quasi-Isostatic Pressing (QIP).

It has been recognized in previous studies on the densification of SHS synthesized materials that there is a time window in which successful densification may be accomplished. Materials must be mechanically loaded within this time window in order to ensure pore closure without brittle failure. Figure 5.4 shows the dependence of the residual porosity on the pressing delay time [Merzhanov (1990)]. The curve has a distinct porosity minimum, which defines the optimum delay time. For longer delay times, the porosity of the material increases, because the ability of the material to flow in response to an applied load decreases as the temperature drops. Figure 5.4 also shows an increase of residual porosity at low pressing delay times. This increase in porosity is connected with the incomplete outgassing of the volatile impurities. The escaping gases create a back-stress that opposes pore closure. In this research the delay time for pressing depended on the volume fraction of NiTi within the TiC-NiTi composite. The optimal delay times were determined by trial and error.

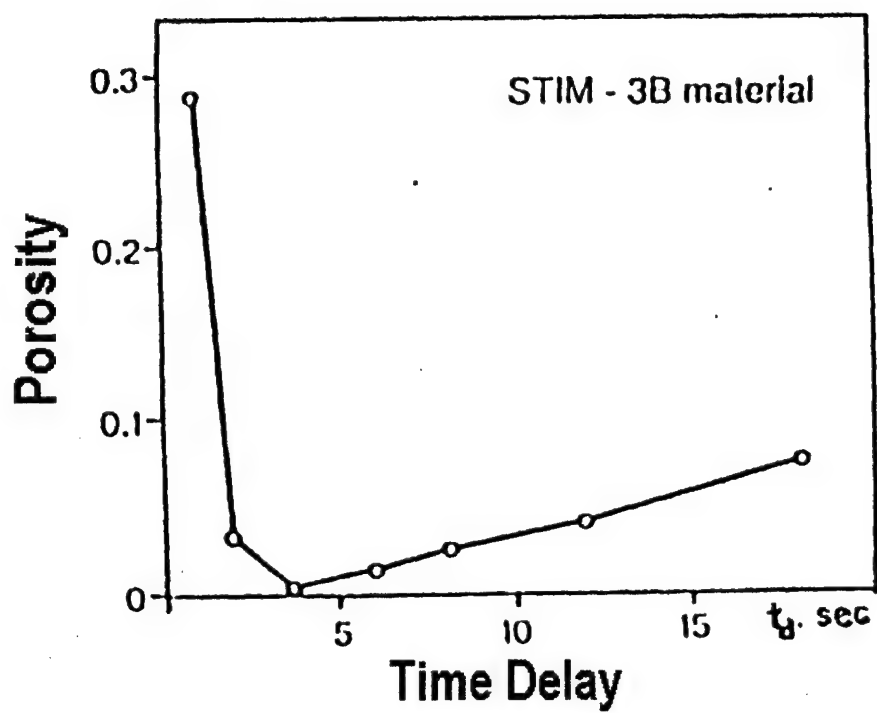
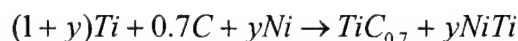
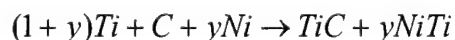


Figure 5.4 Dependence of the residual porosity on the pressing delay time for consolidation of SHS produced material [Merzhanov (1990)].

## VI. Materials and Experimental Procedures

### 6.1 Starting Materials

The starting materials used in this investigation were high purity powders of Ti, C and Ni. The impurity content, as determined by each respective manufacturer, is listed in Tables 6.1-6.3. The average particle sizes for the Ti, C, and Ni were 44  $\mu\text{m}$ , 2  $\mu\text{m}$ , and 3  $\mu\text{m}$ , respectively. The following basic reactions were studied:



Powders were mixed in order to obtain product compositions corresponding to volume fractions of NiTi between 0.2 and 0.8. The powders were loaded under argon into polyethylene jars and dry mixed with burundum<sup>TM</sup> grinding media (4:1 by weight) for 24 hours. Then the powders were baked in a vacuum oven for a minimum of 16 hours at approximately 100 °C and a pressure less than 100 mm Hg in order to remove adsorbed water. After baking, the powders were uniaxially pressed into either 25 g compacts with a diameter of 3 cm and height of 1 cm, or 300 g compacts with a diameter of 7.5 cm and height of approximately 2.5 cm

### 6.2. Combustion Synthesis/ Densification Procedure

The experimental configuration for the synthesis/densification process is shown in Figure 6.1. The fixture used to contain the samples was designed by La Salvia (1995)

Table 6.1. Impurity content for -325 mesh Ti powder from Micron Metals, Inc.

Impurity	Quantity (wt%)
Oxygen	0.314
Nitrogen	0.028
Hydrogen	220 PPM
Chlorine	0.03
Iron	0.044
Silicon	0.01
Carbon	0.017
Magnesium	0.02
Aluminum	<0.01

Table 6.2. Impurity content for 3 micron Ni powder from Aldrich Chemical Co.

Impurity	Quantity (PPM)
Calcium	4
Sodium	3
Magnesium	0.4

Table 6.3. Impurity content of 2 micron C powder from Cerac, Inc.

Impurity	Quantity
Aluminum	<0.01
Calcium	<0.01
Copper	<0.01
Iron	<0.01
Magnesium	<0.01
Manganese	<0.01
Silicon	<0.01
Strontium	<0.01
Titanium	<0.01
Vanadium	<0.01
Zirconium	<0.01



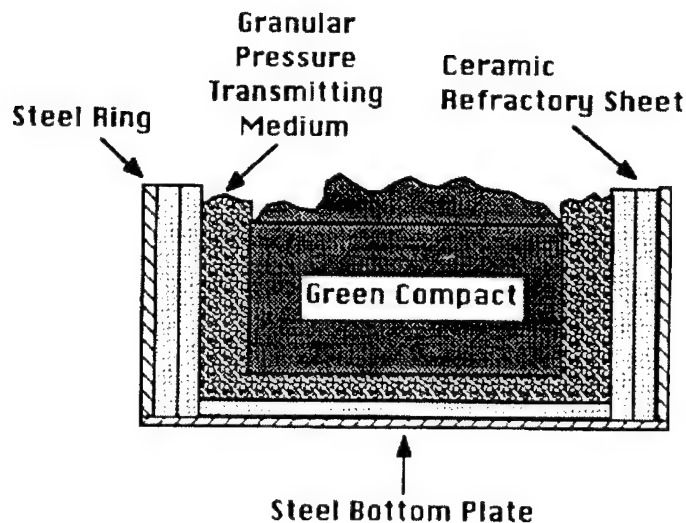


Figure 6.1. Sample containment fixture.

and consisted of a steel cup insulated with two layers of  $\text{Al}_2\text{O}_3\text{-SiO}_2$  refractory sheet (Zircar RSDR-3mm thick). For further insulation and to redistribute the applied axial load, the fixture was filled with an alumina/graphite granular medium. Figure 6.2 shows a backscattered electron micrograph of this granular pressure transmitting medium (PTM). The particles were within 50-230 mesh. The alumina particles were tabular shaped with closed intergranular pores. The graphite particles were generally spheroidal in shape with outward projecting nodules and surface fissures (see arrows). After repeated use the particles would break-up into fragments as shown in Figure 6.3. In this research, the PTM was either replaced after every experiment, or sieved to remove debris from the combustion reaction and fractured PTM particles smaller than 230 mesh. During the SHS/QIP process approximately 0.5 cm of the PTM was placed on the bottom of the cup and the sample was surrounded by it.

To aid the initiation of a planar combustion wave, the sample was also placed beneath a layer of loose Ti+C reactant powder. An electrochemical match consisting of Ni-Cr wire wrapped around a wooden matchstick was buried in the loose powder and ignited remotely by a variable transformer. Since sample reaction resulted in the expulsion of impurity gases, ignition was marked by the ejection of granular media from the containment fixture.

After ignition, samples were mechanically loaded to remove residual porosity. Figure 6.4 shows a schematic representation of the loading as a function of time. The time  $t_1$  (often referred to as the delay time) represents the time between ignition and the beginning of consolidation. In the present study,  $t_1$  was between 10 and 30 seconds. The difference between  $t_2$  and  $t_1$  ( $t_2-t_1$ ) is the time to maximum load. In these experiments the samples were loaded by an Enerpac H frame 100 ton capacity press to a maximum load between 50 and 70 tons. The time to reach the maximum load was approximately 10 sec. The quantity ( $t_3-t_2$ ) is the holding time under load and was set at 10 seconds. The unloading time ( $t_4-t_3$ ) was about one second. After densification the samples were placed in vermiculite for slow cooling. The characteristic times during the QIP densification sequence are reviewed in Table 6.4.

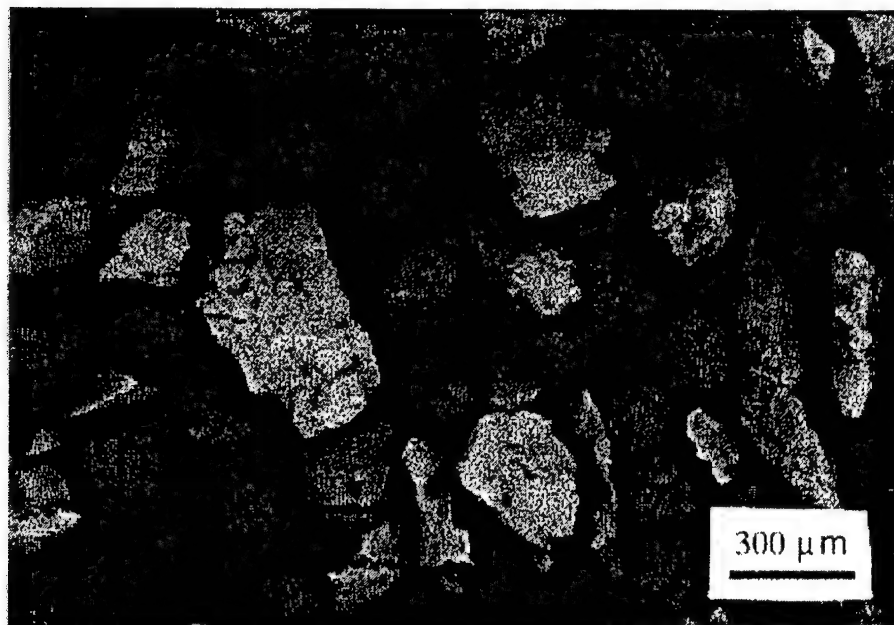


Figure 6.2 Backscattered electron micrograph of alumina/graphite granular pressure transmitting medium.

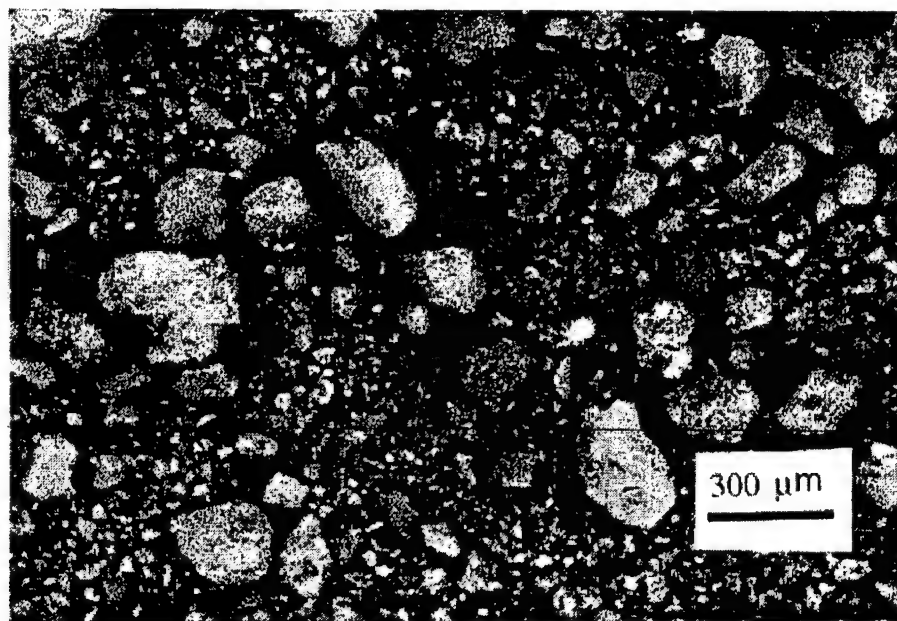


Figure 6.3 Backscattered electron micrograph of alumina/graphite granular pressure transmitting medium after many SHS/QIP cycles.

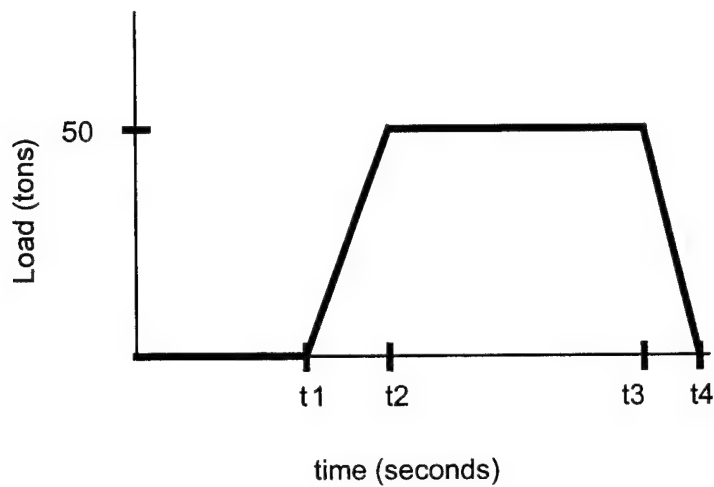


Figure 6.4 Schematic representation of the loading as a function of time during the QIP densification process.

Table 6.4 Characteristic times during QIP densification of SHS produced TiC-NiTi composites

Parameter		Time (sec)
Delay Time	$t_1$	10-30
Loading Time	$t_2 - t_1$	10-15
Holding Time	$(t_3 - t_2)$	10
Unloading Time	$(t_4 - t_3)$	1-2

### 6.3. Material Characterization

Optical and scanning electron microscopy (SEM) were performed to compare the microstructure of SHS produced TiC-NiTi composites with composites produced by standard sintering techniques. The porosity distribution was evaluated using a computer program by Media Cybernetics entitled "Image Pro-Plus." TiC particle size and morphology were also studied as a function of volume fraction of reinforcement. The particle sizes were measured by acquiring 10 images from different regions of the material and making 100 measurements of the particle diameter per image. These 1000 values were then averaged to determine a mean particle diameter,  $(\bar{d})$ . The actual particle size  $(\bar{D})$  was calculated from the expression  $\bar{D} = \frac{3}{2} \bar{d}$ .

X-ray diffraction was used to determine the individual phases present within the composites. The scans were performed using  $\text{Cu K}\alpha$  radiation with a Scintag XRD-2000 Theta-Theta diffractometer. The  $2\theta$  angles considered were between 35 and 80, with a step increment of 0.1.

The transformation temperatures were measured by differential scanning calorimetry (TA Instruments 2920 DSC). Cylindrical samples, 3 mm in diameter and 4 mm in height, were cut by electrodischarge machining from the 7.5 cm diameter composites. The samples were held at 150 °C for ten minutes and then cooled at 5 °C/min to -50 °C. After equilibrating at -50 °C for ten minutes, the samples were then heated back to 150 °C at 5 °C/min. The start and finish temperatures were determined

from the intersection of the tangent to curve at the point of maximum slope with the baseline.

In order to study the effect of thermal cycling on the transformation temperatures and the microstructure, samples were thermally cycled 30 times. This was accomplished by manually transferring them from an oil bath heated to +150 °C and a liquid nitrogen/methanol bath held at -50 °C.

Transmission electron microscopy (TEM) was performed at the National Center for Electron Microscopy (<http://ncem.lbl.gov>) on a JEOL 200CX microscope. The TEM foils were prepared by electrodischarge machining the 3 mm diameter samples used for the DSC measurements into disks with 1 mm thickness. These were ground down to 100  $\mu\text{m}$  on a Buehler Minimet polisher, dimpled to less than 20  $\mu\text{m}$ , and then ion-milled to electron transparency at liquid nitrogen temperature. It is important to note that during the foil preparation, wax was used to attach the samples to the necessary fixtures. This required heating the samples to 144°C, which was above the  $A_f$  temperature. Consequently, the samples were thermally cycled through the transformation during sample preparation. However, since the samples were held at liquid nitrogen temperature during the entire ion-milling process, the martensitic microstructure in the thin foils was formed in the bulk condition.

The NiTi morphology formed in the bulk condition was studied by performing TEM at room temperature. Selected area diffraction patterns, bright field, and dark field images were acquired to determine the presence of the B2, B19' and R phases and to characterize their morphologies both near and far from the carbide particles. Then in-situ heating and cooling was used to transform the sample in the microscope.

The sample holder used was a Gatan 636 double tilt analytical holder with a temperature range between  $-170^{\circ}\text{C}$  and  $+150^{\circ}\text{C}$ . The samples were heated in stages to  $110^{\circ}\text{C}$  (above the  $A_f$  temperature) and then cooled in stages back to room temperature. Liquid nitrogen was added to cool below room temperature. In-situ heating and cooling was used to investigate the transformation path, martensite nucleation and growth, and the effect of carbide particles on the transformation. The in-situ experiments were performed in stages in order to record selected area diffraction patterns, bright field and dark field images. The experiments were also recorded on video. It is important to note that the martensite formed during the in-situ experiments was subject to thin foil effects.

The chemical composition was first studied by microprobe. However, since the interaction volume of the electron beam was larger than the spacing between the carbide particles, it was not possible to get an accurate measurement of the NiTi matrix chemistry by this technique. Consequently, energy dispersive x-ray analysis (EDX) was performed within the TEM in order to determine the chemical composition of the matrix. A Kevex high angle detector (HAD) and a Kevex ultra thin window (UTW) detector were used. A NiTi sample (SE-508) from Nitinol Devices and Components Inc. was used for calibration. Table 6.5 lists the composition of the NiTi standard as determined by the manufacturer using a Direct Current Plasma Spectrometer. The uncertainty is within one percent.

The density of the TiC-NiTi composites was measured using the water absorption method outlined in ASTM C-373. The measured values were compared to the theoretical densities listed in Table 6.6. It is important to mention that the surfaces

Table 6.5 Chemical composition of NiTi standard used to determine matrix chemistry of TiC-NiTi composites. Reporting level  $\pm 1\%$ .

Element	Weight Percent
Ni	55.7
Ti	Balance
O	0.02
H	<0.0003
Co	0.0273
Fe	0.1800
Cu	<0.0050
C	0.0043

of samples were either ground or cut by electrodischarge machining prior to all density measurements in order to remove embedded PTM particles.

Ultrasonic testing was used to determine the elastic constants of the TiC-NiTi composites. The longitudinal ( $V_L$ ) and shear ( $V_s$ ) were measured using a Panametrics Model 5072 pulse receiver and oscilloscope. The Poisson's ratio ( $\nu$ ), Young's modulus ( $E$ ), and shear modulus ( $G$ ) were calculated from the following equations, assuming the material was homogeneous and isotropic:

$$\nu = \frac{1 - 2\left(\frac{V_s}{V_L}\right)^2}{2 - 2\left(\frac{V_s}{V_L}\right)^2}$$

$$E = V_L^2 \rho \frac{(1 + \nu)(1 - 2\nu)}{(1 - \nu)}$$

$$G = V_s^2 \rho$$

where  $\rho$  is the density.



Table 6.6 Theoretical densities of TiC-NiTi and TiC<sub>0.7</sub>-NiTi composites

Vol%NiTi	$\rho_{th}$ (TiC-NiTi)	$\rho_{th}$ (TiC <sub>0.7</sub> -NiTi)
0	4.93	4.63
10	5.08	4.81
20	5.23	4.99
30	5.39	5.18
40	5.54	5.36
50	5.69	5.54
60	5.84	5.72
70	5.99	5.91
80	6.14	6.09
90	6.29	6.27
100	6.45	6.45

#### 6.4. Mechanical Testing

Quasi-static axial compression tests were performed at a variety of temperatures above and below the  $R_s$  transformation temperature using an Instron machine specially equipped with a Research Incorporated radiant furnace and ceramic compression arbor designed by Dave Lischer of the Center for Excellence in Advanced Materials. Figure 6.5 shows the experimental apparatus. The radiant furnace was composed of four 500 watt tungsten light bulbs set in a quad elliptical mirrored chamber. Each lamp was positioned at one foci of one of the elliptical sub-chambers. The sample was positioned so that it sat at the other foci, which was common for each of the four elliptical sub-chambers. A controller was used to monitor the output of a thermocouple in the chamber, compare this temperature to a set value, and adjust the voltage to the lamps accordingly. A thermocouple was also placed directly in contact with the sample.

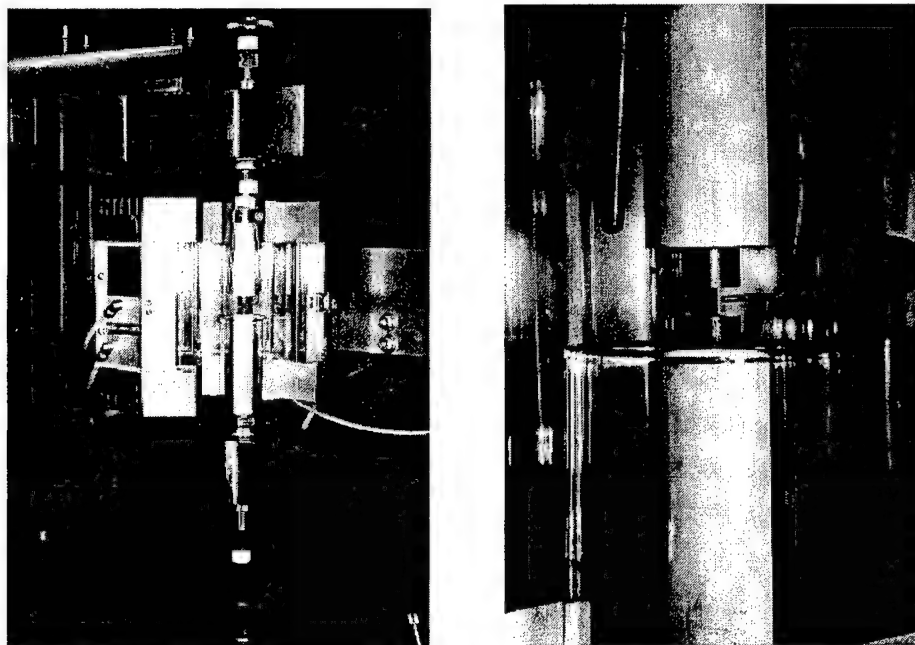


Figure 6.5 Instron machine with radiant furnace and ceramic compression arbor used for quasi-static experiments.

The TiC-NiTi composites for the quasi-static compression tests were cut by electrodischarge machining into cylindrical samples, 3.8 mm in diameter and 6 mm in height. Strain gages were attached to the samples in order to study the mechanical behavior at strains less than one percent. The strain gages were purchased from Measurements Group Inc. Initially the gages used were the WK-06-062AP-350 gages. These gages had a stiff backing, which tended to crack during attachment. In order to avoid damaging the gages during attachment, these WK-series gages were replaced by the EA-06-062AQ-350 Option LE gages which had a flexible backing that was less likely to crack. These EA-series gages had a maximum normal operating temperature of 175 °C, which exceeded the maximum test temperature of 110 °C maximum. The gages for room temperature tests were attached with Loctite Depend glue. This

adhesive could not be used for elevated temperature tests. Although it was rated for a maximum operating temperature of 121 °C, quasi-static tests performed at temperatures higher than 100 °C showed extremely high stresses with almost no corresponding strain. This was obviously unrealistic and was attributed to softening of the Loctite Depend adhesive. Since there was no longer a good bond between the sample and the gage, the strain was not being measured by the gage. For the elevated temperature tests the M-Bond 610 Adhesive from Measurements group was used. This adhesive was rated to have an operating temperature range between -269 °C to 260 °C. A very careful attachment procedure was required in order to ensure a good bond between the strain gage and the sample. Before the gage could be attached, the surface of the sample had to be carefully prepared. This required sanding the surface the sample, cleaning the area with acetone, applying the Measurement Group Inc.'s M-Prep conditioner and M-prep Neutralizer 5A, and then cleaning the area again with acetone. Because the test samples were so small, the gages had to be cut down in order to remove extra backing material. The back of the gage and the sample surface were then coated with a thin layer of the M-bond 610 adhesive. The adhesive was air-dried for 5 minutes and then the gage was attached to the sample. A silicone gum pad was placed over the gage and held in place with either a spring clamp or vice grips. The clamped gage/specimen assembly was then placed in a cool oven. The temperature of the oven was raised to 150 °C and the adhesive was cured for 2 hours.

During quasi-isostatic compression testing, the TiC-NiTi samples were sandwiched between silicon nitride whisker reinforced silicon carbide platens. Tests

were conducted at temperatures below  $R_f$ , slightly above  $R_s$ , and above  $A_f$ . Both the loading and unloading response of the material was monitored.

Flexural strength was measured using the four-point bending technique outlined in ASTM C-1161.

The Vickers hardness of the TiC-NiTi composites was measured using a Leco Microhardness Testing Machine Model M-400-H1. The load was 1000g for 15 sec.

Dynamic compression tests were performed using a modified split Hopkinson bar. The technique is illustrated in Figure 6.6. The material sample was placed between two long bars of known dimensions and elastic properties. A striker bar impacted the incident bar and generated an elastic wave that traveled down the length of the bar. At the incident bar/sample interface a portion of the elastic wave was reflected back along the incident bar and the remaining portion passed through the sample into the transmission bar. The waves were recorded by strain gages on the bars. The data from the reflected wave was used to determine the strain in the sample. The data from the transmitted wave was used to determine the stress in the sample

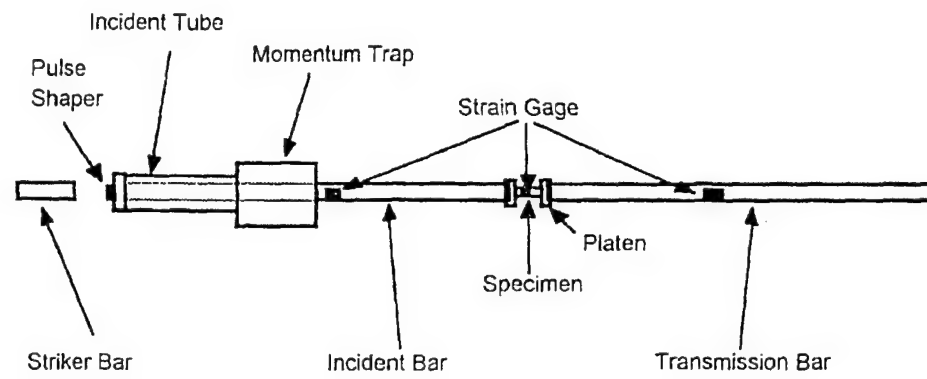


Figure 6.6 Configuration of the split hopkinson bar dynamic testing technique.

Since interest in TiC-NiTi composites focuses on their use as an armor material, ballistic tests were performed on the composites. Targets with a nominal diameter of 42 mm were cut by water jet from the center of the 7.5 mm samples. Since the water jet cutting created targets with a corrugated rim, the targets were then ground on a lathe to a diameter of 40 mm. The embedded PTM on the surface of the targets was removed by electrodischarge machining. Two different test configurations were used. In the configuration shown in Figure 6.7, the TiC-NiTi target was simply taped to a large steel back plate. There was no lateral confinement. A 1090 steel projectile, 25 mm in length and 3.9 mm in diameter, was fired at a velocity of 500 m/s. Since the projectile mass was 0.0019 kg, the energy of impact was 240 Joules. This experiment was performed at the Center of Excellence in Advanced Materials (CEAM) on the UC San Diego campus under the direction of Jon Isaacs and Dr. Sia Nemat-Nasser.

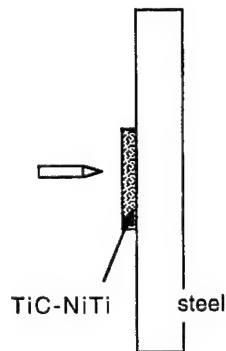


Figure 6.7 Ballistic test configuration for target that was not laterally confined (Configuration 1).

Figure 6.8 shows another configuration used to test the composites. In this configuration, the TiC-NiTi composites were press fit into 1.9 cm thick steel plates. A much larger steel projectile was used. The projectile length was 38.1 mm, the diameter was 12.7 mm, and the mass was 0.031 kg. The projectile velocity was varied from 350 m/s to 650m/s, corresponding to impact energies between 1885 Joules and 6500 Joules. These tests were carried out at UC Berkeley in the lab of Dr Werner Goldsmith.

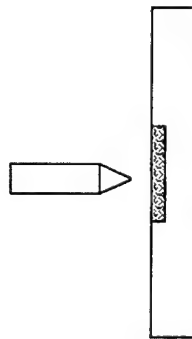


Figure 6.8 Ballistic test configuration for targets that were press fit into steel plate.  
Configuration 2.

## VII. Results and Discussion

### 7.1 Thermodynamic Analysis

#### Adiabatic Temperature Calculations

Using data from Barin's Thermochemical Data of Pure Substances (1995), the adiabatic temperatures for the TiC-NiTi system were determined graphically by the intersection of the product enthalpy curve with the reactant enthalpy curve. The results are shown in Figure 7.1. These calculations, although neglecting heat losses to the environment, provided an upper bound to sample temperature and were useful for preliminary selection of processing conditions, such as the delay time and load. Samples with low NiTi content achieved much higher reaction temperatures than samples with high NiTi content. These high temperatures were crucial for successful densification, because there was little liquid NiTi to facilitate material flow. Densification had to be accomplished before the TiC particles formed a rigid skeletal structure that resisted deformation [LaSalvia *et al.* (1994)]. Samples with low NiTi content were successfully consolidated by using short delay times and high loads. On the other hand, samples with high NiTi content did not produce high temperatures, but had a larger quantity of liquid available to accommodate viscous flow. In these samples, lower loads were used to remove residual porosity.



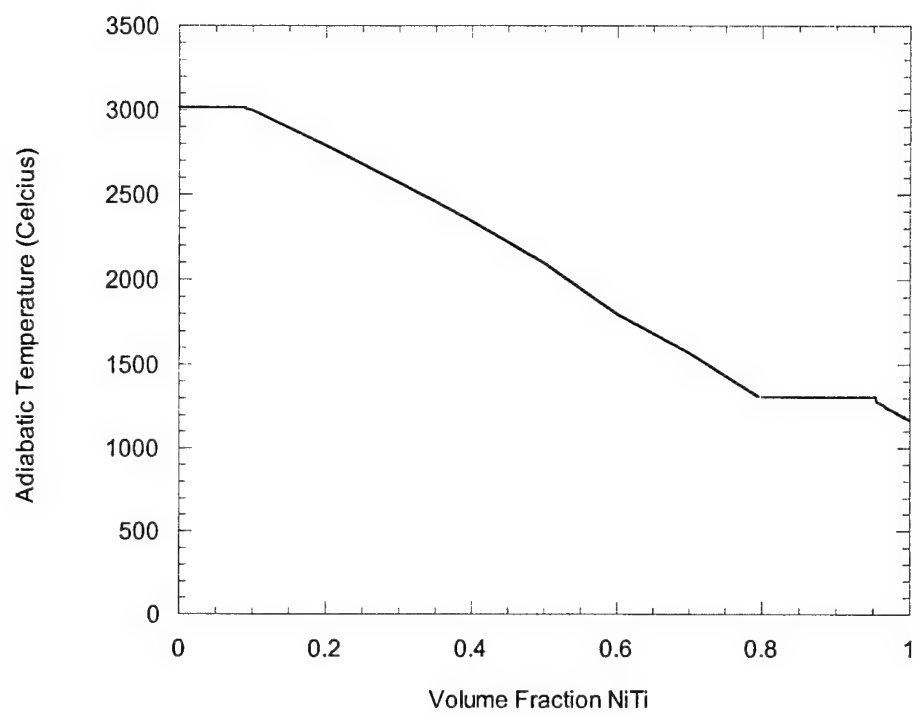


Figure 7.1 Adiabatic temperature in TiC-NiTi system as a function of volume fraction of NiTi.

## 7.2 X-ray Diffraction Analysis

The diffraction scan for a TiC-40vol%NiTi composite is shown in Figure 7.2. Comparison with the JCPDS Powder Diffraction file confirmed the presence of TiC and Ni<sub>3</sub>Ti. Although Ni<sub>3</sub>Ti was not anticipated as a product phase it was repeatedly the dominant matrix phase in samples mixed anticipating stoichiometric titanium carbide. Figure 7.3 shows the backscattered electron micrograph of the composite. The matrix appears to be composed of two phases forming a eutectic structure, consistent with the loss of Ti from the Ni-Ti matrix. According to the Ni-Ti-C ternary phase diagram [Stover *et al.* (1959)], there is a field of three-phase equilibrium where TiC coexists with NiTi and Ni<sub>3</sub>Ti.

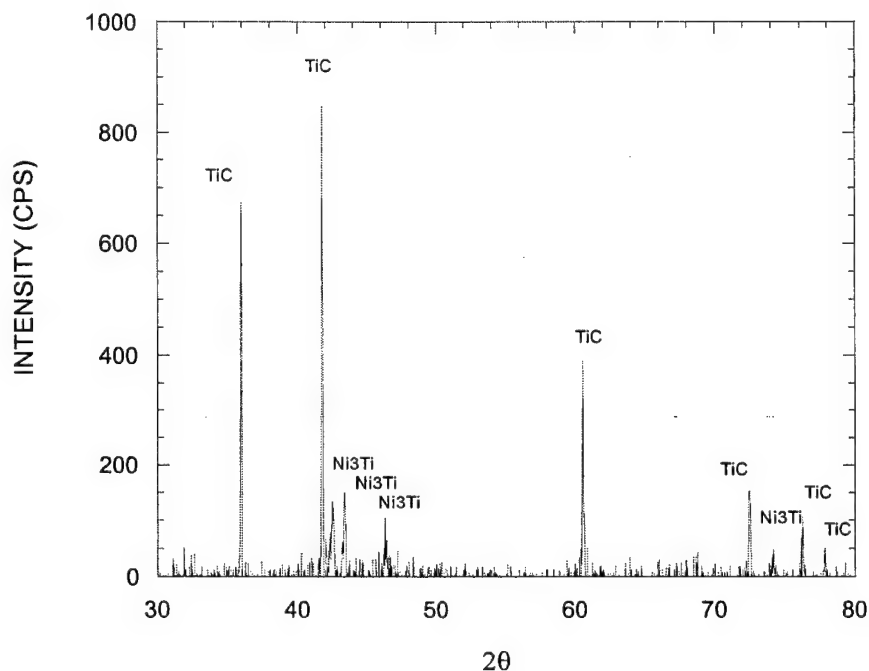


Figure 7.2 X-ray diffraction scan for stoichiometric TiC-40vol%NiTi.



Figure 7.3 Backscattered electron micrograph of stoichiometric TiC-40vol% NiTi. The microstructure, consisting of TiC particles surrounded by a two-phase matrix, is typical of composites synthesized with the anticipation of stoichiometric carbide formation.

The apparent loss of titanium in SHS produced TiC-NiTi composites could not be accounted for by volatilization. The maximum temperatures achieved during the reaction were always lower than the boiling point of titanium (3357 °C). On the other hand, studies on sintered TiC-NiTi have revealed that there can be a redistribution of Ti atoms from the matrix to the carbide [Poletika *et al.* (1983) and Kul'kov *et al.* (1984)]. This process leads to titanium impoverishment in the matrix and consequently the formation of Ni<sub>3</sub>Ti. The transfer of titanium from the NiTi matrix to the carbide is possible, because TiC<sub>x</sub> forms a single phase over a wide range of compositions (Figure 2.1). This wide range of compositions is caused by defects in the carbon sublattice of the sodium chloride structure of TiC<sub>x</sub>. In the present work, it was proposed that the formation of nonstoichiometric titanium carbide occurred

during combustion synthesis of TiC-NiTi composites and accounted for the presence of Ni-rich phases within the matrix.

The stoichiometry of the carbide can be determined by comparing the characteristics of the reactant powder mixture with the resulting product structure. According to the Ni-Ti phase diagram (shown in Figure 3.1) a liquid with the composition 61at%Ni-39at%Ti undergoes an eutectic reaction to form  $\text{Ni}_{57}\text{Ti}_{43}$  and  $\text{Ni}_3\text{Ti}$ . The proportions of these products are determined by the lever rule to be 77.8%  $\text{Ni}_{57}\text{Ti}_{43}$  and 22.2%  $\text{Ni}_3\text{Ti}$ . Since the initial molar quantities of titanium, carbon and nickel ( $x_{\text{Ti}}$ ,  $x_{\text{C}}$ , and  $x_{\text{Ni}}$ , respectively) used in the reaction are known, the equation  $x_{\text{Ti}}\text{Ti} + x_{\text{C}}\text{C} + x_{\text{Ni}}\text{Ni} \rightarrow x_{\text{TiC}}\text{TiC}_x + x_{\text{Ni}_3\text{Ti}}\text{Ni}_3\text{Ti} + x_{\text{NiTi}}\text{Ni}_{57}\text{Ti}_{43}$  can be solved by elemental balance for the carbide stoichiometric coefficient  $x$ . For the TiC-40vol% NiTi sample shown in Figure 7.3, the carbide stoichiometry was calculated to be  $x=0.8$ .

Since the intermetallic  $\text{Ni}_3\text{Ti}$  is a relatively brittle phase that does not undergo stress-induced phase transformation, its presence within the matrix of TiC-NiTi composites was not desirable. In an attempt to suppress formation of  $\text{Ni}_3\text{Ti}$ , samples were prepared with additional titanium. Powder was mixed anticipating the formation of  $\text{TiC}_{0.7}$ . Figure 7.4 shows the X-ray-diffraction scan for  $\text{TiC}_{0.7}$ -40vol%NiTi. All peaks corresponding to  $\text{Ni}_3\text{Ti}$  have disappeared. The backscattered electron micrograph of the matrix, shown in Figure 7.5, no longer shows evidence of a eutectic structure.

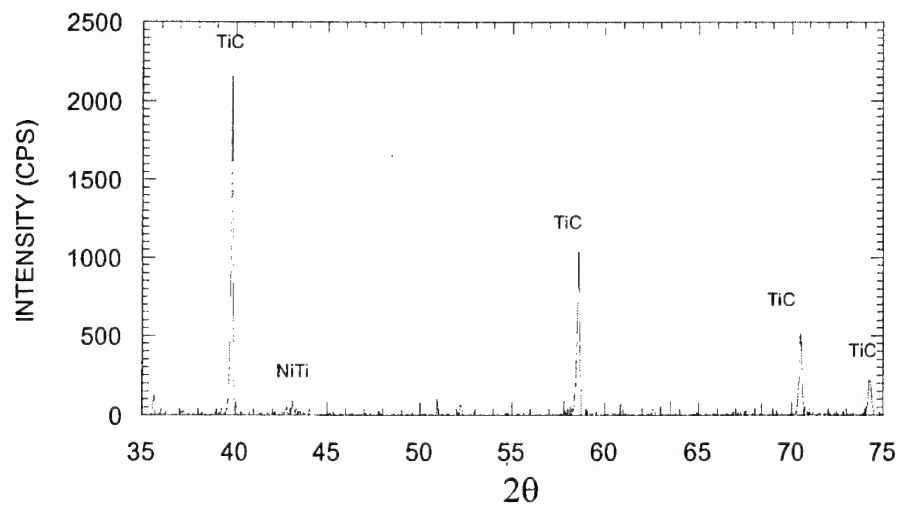


Figure 7.4 X-ray diffraction scan for nonstoichiometric  $\text{TiC}_{0.7}$ -40vol% NiTi. Initial compact size was 3 cm in diameter and 25g .

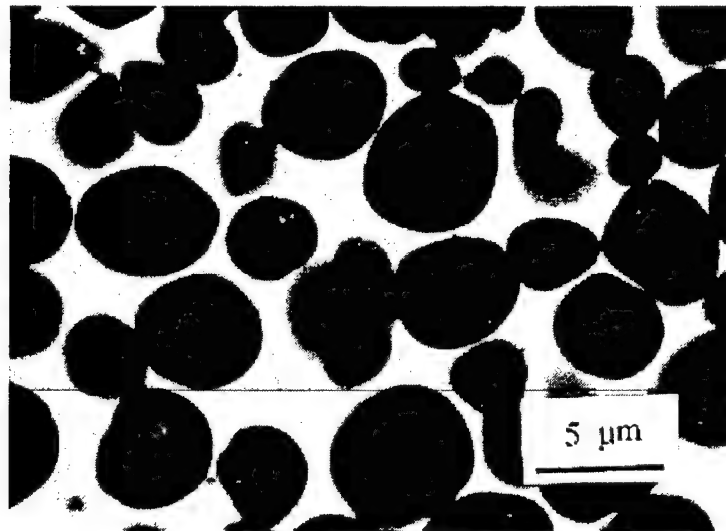


Figure 7.5 Backscattered electron micrograph of nonstoichiometric  $\text{TiC}_{0.7}$ -40vol%NiTi. The microstructure, consisting of spheroidal TiC particles surrounded by a NiTi matrix, is typical of composites synthesized with the anticipation of the formation of nonstoichiometric carbide. Initial compact size was 3 cm in diameter and 25g .



Figure 7.6 Selected area diffraction pattern in  $\text{TiC}_{0.7}$ -40 volume % NiTi showing 6-fold rotational symmetry. The pattern matches the NiTi B2 structure. [Courtesy of Dr. A. J. Strutt]

It is important to note that while the peak locations for the NiTi and  $\text{Ni}_3\text{Ti}$  match those listed by JCPDS, the peak intensities do not. This revealed the possibility of preferred grain orientation within the matrix. This feature would not be surprising, because the high reaction temperatures and the long cooling times associated with the SHS processing sequence should facilitate the growth of large NiTi grains. NiTi texture has not been observed in composites formed by vacuum hot pressing. In vacuum hot pressing the matrix is formed from sintering randomly oriented NiTi powders, so the product matrix structure is relatively isotropic.

Figure 7.4 shows that the structure of the NiTi matrix in this particular  $\text{TiC}_{0.7}$ -40vol%NiTi sample is B2 at room temperature. This is confirmed by TEM characterization. The selected area diffraction pattern, shown in Figure 7.6, has the 6-fold rotational symmetry which excludes the monoclinic structure of the B19' phase.

The lattice parameter is calculated to be  $3.05 \text{ \AA}$ , which is within 2% of the value reported by JCPDS for B2 NiTi. These results are for small samples (3 cm diameter, 25g) reacted anticipating carbide with a stoichiometry coefficient of  $x=0.7$ . The XRD scans for larger samples (7.5 cm diameter, 300g) mixed anticipating the same carbide stoichiometry are shown in Figure 7.7. The  $\text{Ni}_3\text{Ti}$  phase has also been successfully suppressed, but the NiTi matrix is martensitic at room temperature. The matrix in 20NiTi, 40NiTi and 60NiTi composites is a combination of the R and B19' phases. The 80 NiTi sample has only the R-phase structure. Therefore, it is important to emphasize that the structure of the NiTi matrix in composites mixed anticipating the formation of nonstoichiometric carbide depends on the initial compact size.

The dependence of the structure of the NiTi matrix on sample size is most probably the result of differences in cooling rates. As described by LaSalvia (1994), the carbide which forms first during the SHS reaction is most likely to have a composition in equilibrium with the saturated melt. From the Ti-C phase diagram (Figure 2.1) this composition corresponds to  $\text{TiC}_{0.47}$ . Quenching experiments have shown that this carbide forms as a layer on the surface of the carbon particles. As C diffusion proceeds through the carbide layer, the stoichiometry of the  $\text{TiC}_x$  increases. In smaller samples, which cool faster, it is expected that the stoichiometric coefficient  $x$  will be smaller than in larger samples. This will result in a Ni-rich matrix, which is known to lower the  $M_s$  temperature.

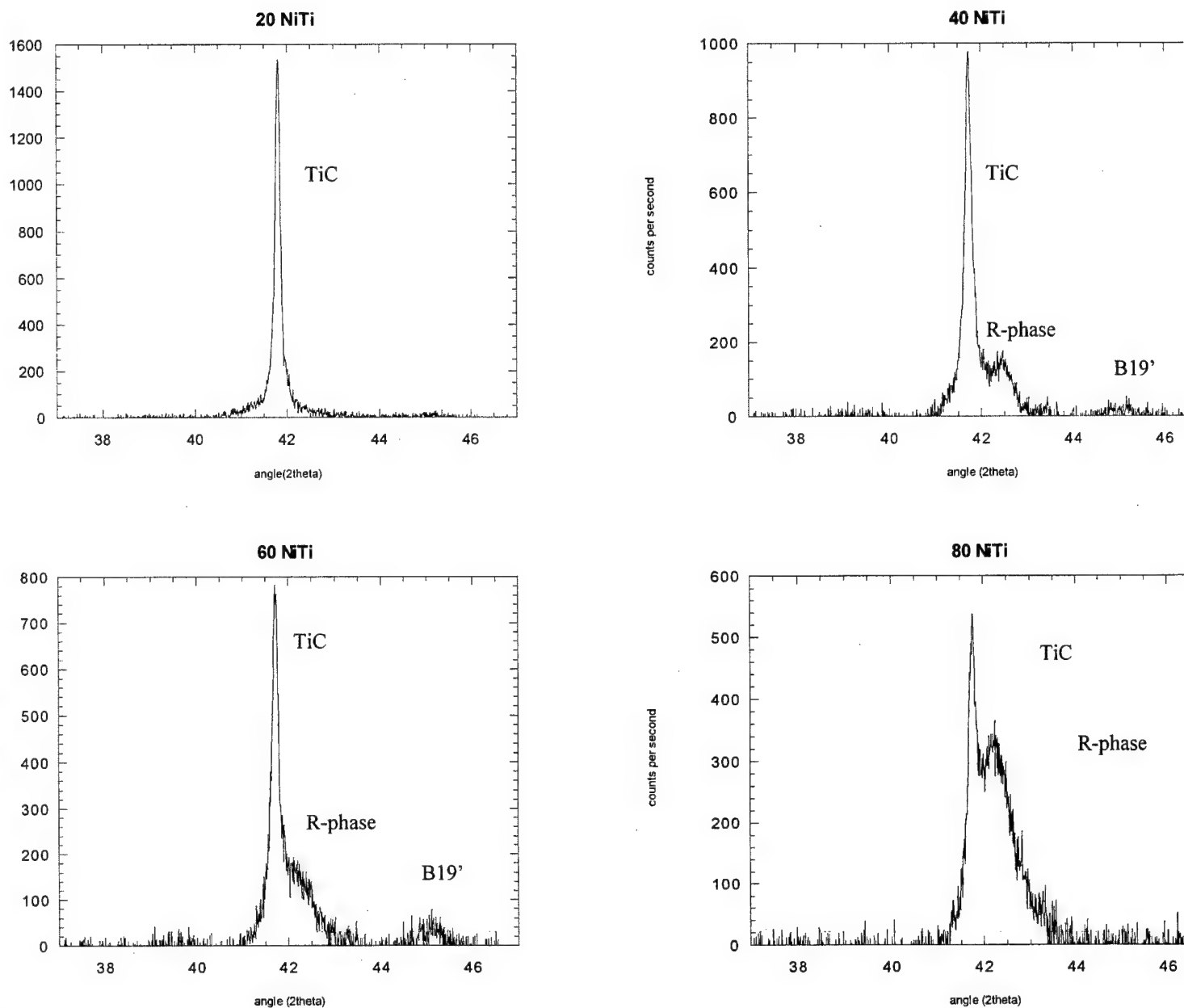


Figure 7.7 X-ray diffraction scans for TiC<sub>0.7</sub>-NiTi samples with initial compact size of 7.5 cm in diameter and 300g. ,



### 7.3 Shape Change During QIP

#### 7.3.1 Theory

The objective of this section is to provide a framework for calculating the shape distortion of an initially cylindrical specimen subjected to QIP. The full prediction of distortion requires finite element computation. The calculation of the change in the height ( $H$ )/diameter ( $2R$ ) ratio (also called aspect ratio) as a function of the mechanical properties of the PTM and porous sample can be made by analytical methods.

For this analysis, the constitutive behavior of the PTM is assumed to be elastic [Lichti and Hofstatter (1985)]. The constitutive behavior of the porous body is assumed to be nonlinearly-viscous. Nonlinear-viscous mechanical behavior is typical of powdered materials under conditions of hot compaction or two-phase composites containing liquid. It is also assumed that the stresses are uniform within both the PTM and porous body. For simplicity, a cylindrical geometry is assumed, and cylindrical coordinate system is used throughout this paper (see Figure 7.8). The procedure is described below.

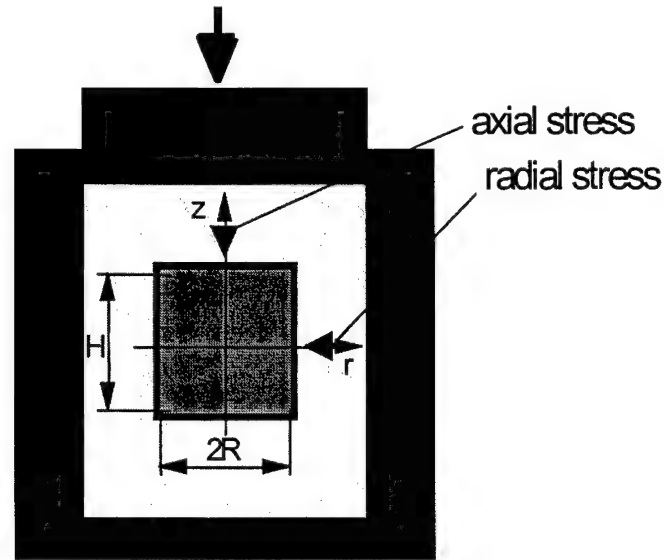


Figure 7.8. Loading mode under Quasi-Isostatic Pressing.

#### 7.3.1.1 Equations Describing the Constitutive Behavior of a Porous Specimen

The mechanical response of a nonlinear-viscous porous body can be described [Skorohod *et al.* (1993a,b), Olevsky (1996)] by a rheological (constitutive) relationship connecting components of stress tensor  $\sigma_{ij}$  and strain rate tensor  $\dot{e}_{ij}$  :

$$\sigma_{ij} = A \left( \frac{\sqrt{\varphi \dot{\gamma}^2 + \psi \dot{e}^2}}{\sqrt{1-\theta}} \right)^{n-1} \left[ \varphi \dot{e}_{ij} + \left( \psi - \frac{1}{3} \varphi \right) \dot{e} \delta_{ij} \right] \quad (1)$$

where  $A$  and  $n$  - are material creep parameters;  $\varphi$  and  $\psi$  are the shear and bulk normalized viscosity module, which depend on porosity  $\theta$  (for example, following

[Skorohod *et al.* (1993a,b), Olevsky (1996)],  $\varphi = (1-\theta)^2$ ,  $\psi = \frac{2(1-\theta)^3}{3\theta}$ ;  $\delta_{ij}$  is a

Kronecker symbol ( $\delta_{ij} = 1$  if  $i=j$  and  $\delta_{ij} = 0$  if  $i \neq j$ );  $\dot{e}$  is the first invariant of the strain rate tensor, i.e. sum of tensor diagonal components:  $\dot{e} = \dot{e}_{11} + \dot{e}_{22} + \dot{e}_{33}$ ;  $\dot{\gamma}$  is the

shape change rate. In cylindrical coordinates, the ratio of the radial  $\sigma_{rr}$  and axial  $\sigma_{zz}$  stresses is

$$\frac{\sigma_{rr}}{\sigma_{zz}}(specimen) = \frac{\left( \phi \dot{e}_{rr} + \left( \psi - \frac{1}{3} \phi \right) \dot{e} \right)}{\left( \phi \dot{e}_{zz} + \left( \psi - \frac{1}{3} \phi \right) \dot{e} \right)} \quad (2)$$

The volume-change rate  $\dot{e}$  and the shape-change rate  $\dot{\gamma}$  in cylindrical coordinates are given by:

$$\dot{e} = \dot{e}_{zz} + 2\dot{e}_{rr} = \left[ 1 + 2 \left( \frac{\dot{e}_{rr}}{\dot{e}_{zz}} \right) \right] \dot{e}_{zz} = \frac{\dot{\theta}}{1 - \theta} \quad (3)$$

$$\dot{\gamma} = \sqrt{\frac{2}{3}} |\dot{e}_{zz} - \dot{e}_{rr}| = \sqrt{\frac{2}{3}} \left| 1 - \left( \frac{\dot{e}_{rr}}{\dot{e}_{zz}} \right) \right| |\dot{e}_{zz}| \quad (4)$$

where  $\dot{e}_{zz}$ ,  $\dot{e}_{rr}$ , and  $\theta$  are the axial strain rate, radial strain rate, and porosity, respectively. For a cylindrical specimen, the axial and radial strain-rates are also given by:

$$\dot{e}_{zz} = \frac{\dot{H}}{H}; \dot{e}_{rr} = \frac{\dot{R}}{R} \quad (5)$$

where  $H$  and  $R$  are the instantaneous cylinder height and radius. Equation (4) gives the following relationship for the shape-change rate:

$$\dot{\gamma} = \sqrt{\frac{2}{3}} \left| \frac{H}{R} - \frac{R}{H} \right| \quad (6)$$

This expression will be used to derive relationships between the height and radius of the cylindrical specimen and porosity.

### 7.3.1.2 Equations Describing the Constitutive Behavior of PTM

For the PTM, the radial and axial stresses are related to the axial strain  $e_{zz}$  by Hooke's law and are given by:

$$\sigma_{rr} = \left[ \frac{\nu}{(1 + \nu)(1 - 2\nu)} \right] E \varepsilon_{zz} \quad (7)$$

$$\sigma_{zz} = \left[ \frac{1 - \nu}{(1 + \nu)(1 - 2\nu)} \right] E \varepsilon_{zz} \quad (8)$$

where  $\nu$  and  $E$  are the Poisson's ratio and Young's modulus for the PTM. These depend upon PTM porosity  $\theta_p$  and are given by :

$$\nu = \frac{2 - 3\theta_p}{4 - 3\theta_p} \quad (9)$$

$$E = 4E_o \left[ \frac{(1 - \theta_p)^2}{4 - 3\theta_p} \right] \quad (10)$$

where  $E_o$  is the Young's modulus of the granular material making up the PTM. The ratio of the radial stress to the axial stress is therefore given by:

$$\frac{\sigma_{rr}}{\sigma_{zz}}(PTM) = \frac{\nu}{1 - \nu} = \frac{2 - 3\theta_p}{2} = \frac{1}{k} \quad (11)$$

### 7.3.1.3 Equations Describing the Constitutive Behavior of a Porous Specimen Embedded in PTM

It is assumed that the presence of the porous cylindrical body within the PTM provides a negligible effect on its state-of-stress as a result of the applied axial load. This is equivalent to imagining the porous cylindrical body embedded in an infinitely-extended PTM with a far-field applied stress  $\sigma_{zz}^\infty$  at its boundary. The PTM itself is assumed to be under the condition of uniaxial load with lateral confinement (i.e.

pressing in a rigid die). Therefore, the sample can be considered under conditions of biaxial loading (Fig. 7.8).

Since the specimen dimensions are assumed to be small compared to the PTM, the ratio of the radial stress to the axial stress in the specimen ( $\frac{\sigma_{rr}}{\sigma_{zz}}(specimen)$ ) is assumed to be equal to the ratio of the radial stress to the axial stress in the PTM ( $\frac{\sigma_{rr}}{\sigma_{zz}}(PTM)$ ). Setting Equation (2) equal to Equation (11) yields the following equation for the radial/axial strain rate ratio

$$\frac{\dot{e}_{rr}}{\dot{e}_{zz}} = \frac{k(2-3\theta) - 2}{2(2-3\theta) - k(4-3\theta)} \quad (12)$$

If  $k = \frac{2}{2-3\theta}$  (which means that  $\theta = \theta_p$ ), then  $\dot{e}_{rr} = 0$ , and we have the conditions of pressing in a rigid die. If  $k=1$  (i.e., if  $\theta_p = 0$  which means that PTM is an incompressible material),  $\dot{e}_{rr} = \dot{e}_{zz}$ , and we have the conditions of isostatic pressing. If  $k \rightarrow \infty$  (i.e., if  $\theta_p = 2/3$ ) which approximately corresponds to the density of packed isomeric spherical particles then  $\dot{e}_{rr} = \frac{3\theta-2}{4-3\theta}\dot{e}_{zz}$ , and we have the conditions of free up-setting.

Combining Equations (3), (5), and (12) gives the following expression for the axial strain-rate in terms of the rate-of-change of porosity:

$$\dot{e}_{zz} = \frac{\dot{H}}{H} = \frac{1}{3} \left[ \frac{2\theta_p + (1-3\theta_p)\theta}{(1-\theta_p)(1-\theta)} \right] \frac{\dot{\theta}}{\theta} \quad (13)$$

Combining Equations (3), (12), and (13) gives the following expression for the radial strain-rate in terms of the rate-of-change of porosity:

$$\dot{\epsilon}_{rr} = \frac{\dot{R}}{R} = \frac{1}{3} \left[ \frac{\theta - \theta_p}{(1 - \theta)(1 - \theta_p)} \right] \frac{\dot{\theta}}{\theta} \quad (14)$$

The shape change rate can be represented as follows :

$$\dot{\gamma} = 2\sqrt{6} \left| \frac{(1 - \theta)(1 - k)}{2(2 - 3\theta) - k(4 - 3\theta)} \right| |\dot{\epsilon}_{zz}| \quad (15)$$

Subtracting Equation (14) from (13), and integrating gives the following expression for the aspect ratio  $H/R$ :

$$\begin{aligned} \frac{\dot{H}}{H} - \frac{\dot{R}}{R} &= \left( \frac{\theta_p}{1 - \theta_p} \right) \frac{\dot{\theta}}{\theta} \Rightarrow \int_{\frac{H_0}{R_0}}^{\frac{H}{R}} d \ln \left( \frac{H}{R} \right) = \left( \frac{\theta_p}{1 - \theta_p} \right) \int_{\theta_0}^{\theta} d \ln \theta \\ \Rightarrow \frac{H}{R} &= \frac{H_0}{R_0} \left( \frac{\theta}{\theta_0} \right)^{\frac{\theta_p}{1 - \theta_p}} \end{aligned} \quad (16)$$

In deriving Equation (16), it was assumed that  $\theta_p$  is constant. Equation (16) indicates that the change in the aspect ratio  $H/R$  does not depend upon the constitutive behavior of either the PTM or densified body, but depends only on the PTM's porosity and the body's initial density and dimensional parameters.

In Figure 7.9, the curves are shown corresponding, for various PTM porosities, to the relationships between the change of the aspect ratio expressed by the relationship  $\frac{H}{R} / \frac{H_0}{R_0}$  and sample's porosity. For comparison, the curves corresponding

to the conditions of free up-setting, pressing in a rigid die ( $\frac{\dot{\epsilon}_{rr}}{\dot{\epsilon}_{zz}} = 0$ ) and isostatic

pressing ( $\frac{\dot{\epsilon}_{rr}}{\dot{\epsilon}_{zz}} = 1$ ) are shown too [Olevsky *et al.* to be submitted]. Initial porosity of

the sample is assumed to be  $\theta_0 = 0.3$ .

The calculation results indicate that, for sufficiently dense PTM, having porosity  $\theta_p < 0.2$ , the deformation state under QIP is close to the isostatic one. However, for most cases, in the capacity of PTM, industrial sand (alumina) or graphite powder in a loose state are used. Therefore usually  $\theta_p > 0.2$ . This means that the aspect ratio evolution under QIP can be close to that one obtained under the conditions of pressing in a rigid die or free up-setting.

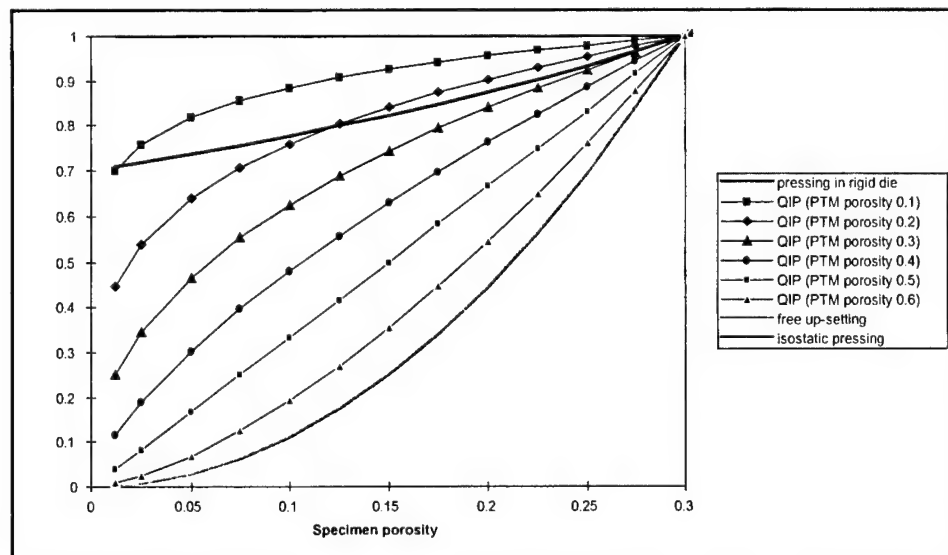


Figure 7.9. Shrinkage anisotropy as a function of specimen porosity under QIP.

### 7.3.2 Experimental Measurements of Shape Change

Nickel and titanium samples were produced by the preliminary cold pressing of loose powders. The cold pressing was performed to produce three nickel and three titanium samples, whose heights and diameters are given in Table 7.1.

In order to vary the yield limit, samples were pre-heated to a variety of temperatures. Each sample was then placed in a thick walled cylinder (inner diameter = 3", height = 4") and surrounded by pressure transmitting medium. The samples were loaded under forces ranging from 2.5 to 10 kN. Diameter and height were measured before and after QIP. The results of experiments are represented in Table 7.1.

Based on the experimental data on initial parameters (aspect ratio and porosity) for QIP of Ni and Ti powder samples, the calculations were performed in conformity to Equation (16). The final aspect ratio was determined from the final height and diameter. PTM (graphite powder) porosity was determined experimentally:  $\theta_p = 0.4$ . This value was used in the calculations.

One can see from Table 7.1 that the experimental and calculation results agree well: for most cases, the relative error in values of the final aspect ratio is smaller than 5%. Thus, Equation (16) can be recommended for use as a practical means for the quantitative prediction of the shape change during QIP in those cases where the compact dimensions are small compared to the dimensions of the containment fixture of the PTM.



Table 7.1 Comparison of theoretical and experimental results on QIPing of Ni and Ti porous samples

	<i>initial height</i>	<i>initial diameter</i>	<i>final height</i>	<i>final diameter</i>	<i>initial porosity</i>	<i>final porosity</i>	<i>change of aspect ratio (experiment)</i>	<i>change of aspect ratio (theoretical)</i>	<i>relative error</i>
Nickel	1.186	1.275	1.031	1.273	0.47	0.38	0.810	0.782	0.035
Nickel	0.478	1.274	0.386	1.264	0.48	0.35	0.305	0.290	0.051
Nickel	0.619	1.274	0.434	1.253	0.51	0.28	0.346	0.297	0.141
Titanium	0.97	1.275	0.863	1.276	0.52	0.46	0.676	0.688	0.018
Titanium	1.508	1.275	1.219	1.267	0.5	0.38	0.962	0.945	0.018
Titanium	0.975	1.278	0.819	1.277	0.45	0.35	0.641	0.621	0.032

## 7.4 Indentation Experiments and Constitutive Response

As mentioned above, the complete description of the densification process requires knowledge of the constitutive response of the material. It is important to obtain this constitutive description, for implementation into computational codes, which can then predict the response of the material under a variety of loading configurations and enable a predictive shape capability. The parameters in Equation (1) can be experimentally measured by performing indentation tests. Figure 7.10(a) shows the experimental setup used. A disk-shaped green compact was placed in an uniaxial testing machine (Instron) and ignited. After the reaction was completed, a cylindrical indenter was moved onto the specimen at a prescribed velocity, producing an indentation, whose cross-section is shown in Figure 7.10(b). The velocity of the sintered SiC indenter was 0.4 m/s. Figure 7.11a shows the experimental stress-strain curve for combustion synthesized TiC-NiTi. The stress is very low (below 10 MPa) up to a strain of 0.6( compressive) , and then rises sharply.

In order to obtain an analytical solution of the indentation process, the uniaxial up-setting of a porous cylinder with a radius smaller than the indenter is modeled. Friction is neglected, as well as the distortion of the compact outside of the main deformation zone.

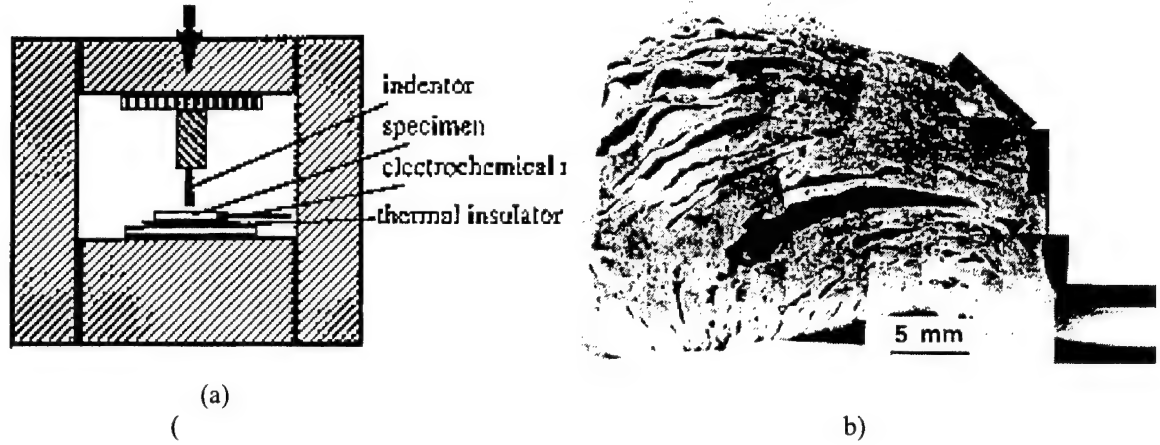


Figure 7.10 (a)Schematic of indentation setup;(b)Cross-section of indented TiC-NiTi specimen, showing distortion and full densification under indenter.

During free upsetting, the applied stresses on the lateral surfaces are equal to zero. By setting  $\sigma_r=0$  in Equation (1), one can obtain the following relationship between the axial and radial strain rates:

$$\frac{\dot{\epsilon}_{rr}}{\dot{\epsilon}_{zz}} = \frac{1-3\left(\frac{\psi}{\phi}\right)}{1+6\left(\frac{\psi}{\phi}\right)} = -\left(\frac{2-3\theta}{4-3\theta}\right) \quad (17)$$

Combining Equations (1), (3), (4) and (17) and considering that  $\sigma_{zz} < 0$ , the following expression for the axial stress is obtained:

$$\sigma_{zz} = -A(6)^{\frac{n+1}{2}} \left[ \frac{(1-\theta)^{n+2}}{(4-3\theta)^{\frac{n+1}{2}}} \right] |\dot{\epsilon}_{zz}|^n \quad (18)$$

The latter equation can be transformed as follows:

$$\frac{|\sigma_z|}{A} \left( \frac{H_o}{V_p} \right)^n = 6^{\frac{n+1}{2}} \left[ \frac{(1-\theta)^{n+2}}{(4-3\theta)^{\frac{n+1}{2}}} \right] \left( \frac{H_o}{H} \right)^n \quad (19)$$

where  $H_o$  is the initial height of the porous cylinder and  $V_p$  is the constant velocity of the indenter. From Equations (3), (5), and (17) it follows that:

$$\frac{\theta}{1-\theta} = \frac{3\theta}{4-3\theta} \frac{\dot{H}}{H} \quad (20)$$

Integration of Equation (20) gives

$$\left( \frac{\theta}{\theta_o} \right)^4 \frac{1-\theta_o}{1-\theta} = \left( \frac{H}{H_o} \right)^3 \quad (21)$$

where  $\theta_o$  is the initial porosity before the indentation. The solution of Equations (19) and (21) enables the determination of the stress-strain dependence characterizing the mechanical response of the porous material.

The dependence of the normalized stress  $\frac{|\sigma_z|}{A} \left( \frac{H_o}{V_p} \right)^n$  on the engineering strain is shown in Figure 7.11(b) for different values of the strain rate sensitivity  $n$ . The engineering strain is calculated as  $\frac{H_o - H}{H}$ . Here it should be noted that the dimensionless stress depends on the strain rate sensitivity  $n$  itself.

Using Equations (19) and (21), one can find the constitutive properties (coefficients  $A$  and  $n$ ) which provide the best fit for the experimental data given in Figure 7.11(a). It is determined that the following values:  $A = 180 \text{ MPa} \cdot \text{s}^{0.2}$ ,  $n = 0.2$  provide the best fit to the experimental data.

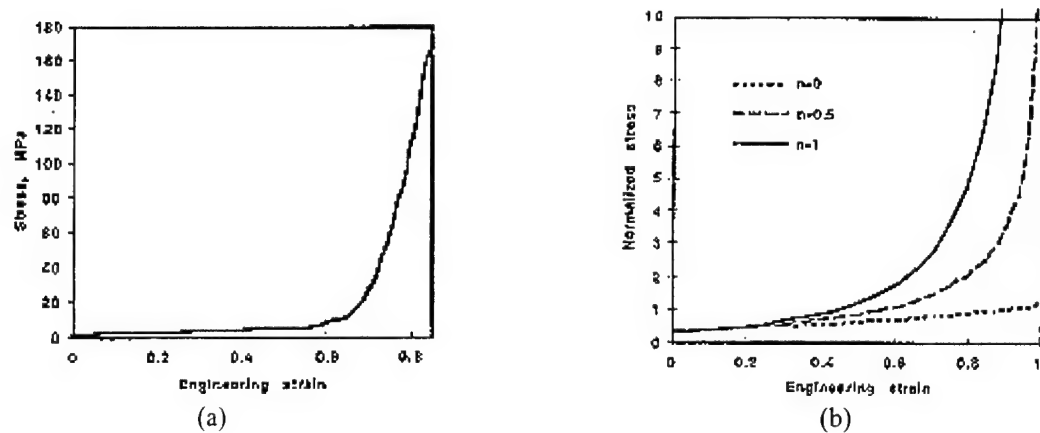


Figure 7.11 (a) Experimentally obtained stress strain response of SHS product (TiC-NiTi); (b) Predictions of stress strain response using Skorohod equation and analytical framework for free-upsetting geometry ( $\sigma_{\pi}=0$ ), for different values of rheology parameter  $n$  ( $A=180 \text{ MPa.s}^n$ ).

## 7.5 SHS/QIP

Figure 7.12 shows the effectiveness of the QIP densification sequence for removing the porosity in 3 cm diameter SHS products. The large voids and lateral channels created during the SHS process are shown in Figure 7.12(a) for a TiC-40 vol% NiTi composite. In Figure 7.12(b) these voids have been collapsed by applying a 125 MPa pressure after a delay time of 10 seconds. The optimum delay time and pressure were dependent on sample composition and size. In 7.5 cm diameter samples, the delay times and loads had to be adjusted to ensure pore collapse while avoiding material extrusion from the containment cup. Surprisingly, the samples with 80vol%NiTi were the most difficult to consolidate. Molten material was ejected from the containment cup immediately after contact with the densification punch. This underscores the importance

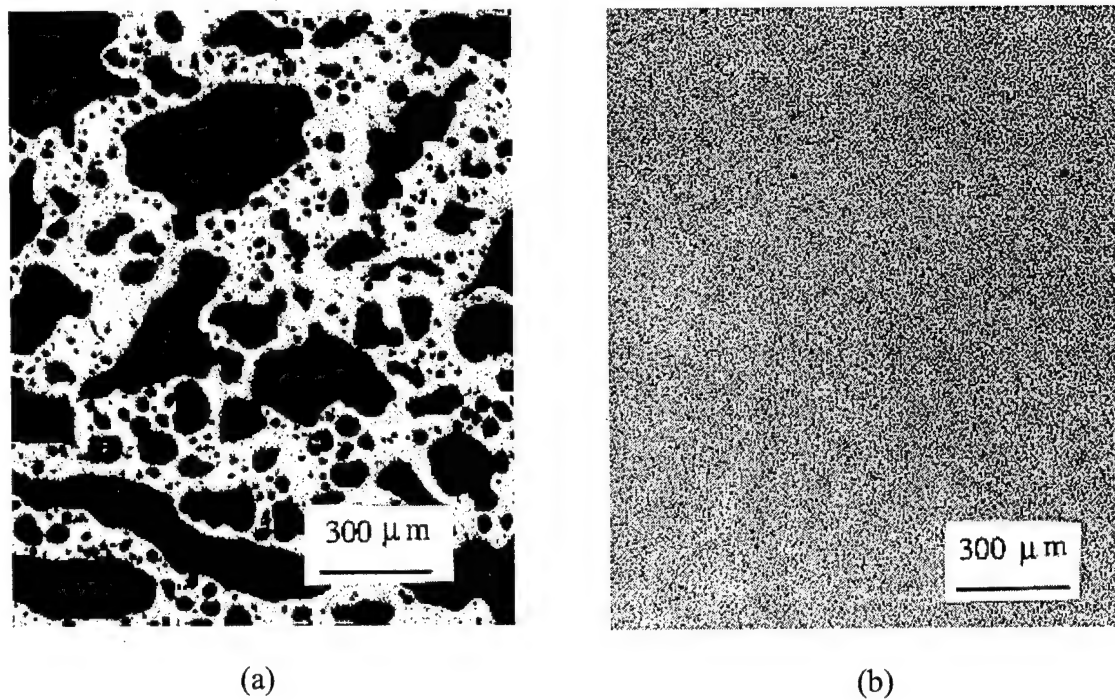


Figure 7.12 Comparison of pore structure in SHS synthesized TiC-40vol% NiTi.  
(a) as-reacted material not subject to post reaction densification;  
(b) reacted and densified material.

of adjusting the delay time and the gap between the punch and containment cup rim. The times and pressures that produced the best results for the 7.5 cm diameter samples loaded according to the configuration in Figure 6.1 are shown in Table 7.2.

Table 7.2 The times and pressures that produced the best results for the 7.5 cm samples loaded according to the configuration in Figure 6.1.

Volume %NiTi	Delay Time	Pressure
20NiTi	5 sec	160 MPa
40NiTi	15 sec	160 MPa
60NiTi	10 sec	120 MPa
80NiTi	15 sec loaded in increments	120MPa

## 7.6 $\text{TiC}_x$ Particle Size and Morphology

Figure 7.5 shows the microstructure of a  $\text{TiC}_{0.7}$ -40vol% NiTi composite, which is typical of composites synthesized anticipating nonstoichiometric  $\text{TiC}_{0.7}$ . The ceramic reinforcement forms spheres within the intermetallic matrix. For this composite the particle size is approximately  $4 \mu\text{m}$ . Table 7.3 shows the  $\text{TiC}_x$  particle size for various volume fractions of NiTi for the 3 cm diameter compacts. The  $\text{TiC}_x$  particle size decreases with increasing volume fraction of NiTi. This is consistent with a decrease in the adiabatic reaction temperature (Figure 7.1). The 7.5 cm diameter samples also show the decrease in particle size with increasing volume fraction of NiTi. However, the actual particle sizes, for a given volume fraction of NiTi, are larger than in the 3 cm

diameter compacts because of slower cooling rates. The particle morphology of the 7.5 cm samples is shown in Figure 7.13.

Table 7.3  $\text{TiC}_x$  particle size as a function of NiTi content in  $\text{TiC}_{0.7}$ -NiTi composites. Compact size 3cm diameter, 25g.

Vol%NiTi	Average $\text{TiC}_x$ particle size ( $\mu\text{m}$ )	Average standard deviation ( $\mu\text{m}$ )
30	6.9	1.8
40	3.9	1.0
50	2.7	0.7

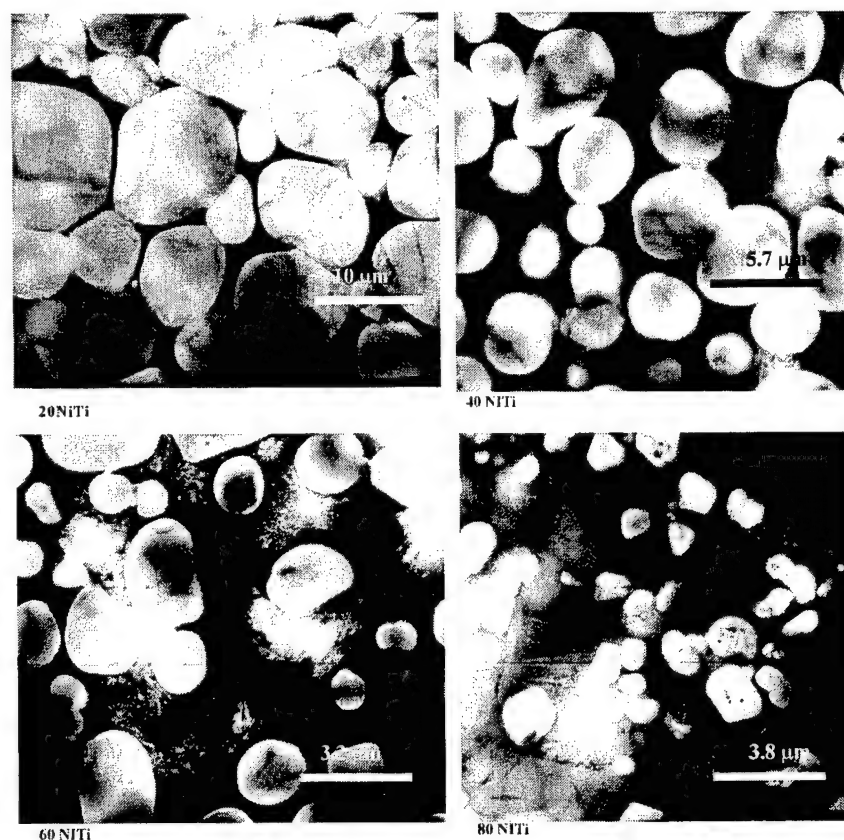


Figure 7.13 The particle morphology of the 7.5 cm diameter  $\text{TiC}_{0.7}$ -NiTi samples [Courtesy of Dr. T Radetic, NCEM].



Several of the microstructural features in SHS produced TiC-NiTi composites differ from those observed in composites formed by vacuum hot pressing. Most notably, the TiC particle size in composites formed by SHS is independent of the initial metal reactant particle size. The heat evolved during the reaction completely melts the Ti and Ni powders, so that there is no trace of the original powder surfaces. Instead, product structure is determined by parameters governing the combustion process, such as the wave propagation mode, wave velocity, maximum reaction temperature and the rate of cooling. In contrast, the TiC particle size in TiC-NiTi composites formed by vacuum hot pressing is essentially the same as the initial TiC powder particle size. The particles are irregularly shaped and often have sharp corners, which can serve as stress concentrators. Another notable difference between the structures produced by the two processing techniques is the porosity. There are no pores within the TiC particles in samples produced by SHS. Pores only appear within the matrix, and these can be removed by QIPing with an appropriate delay time. In samples produced by vacuum hot pressing pores appear both within the TiC particles and within the matrix. The pores in the TiC particles are reported to be artifacts of the original starting TiC powder. Since they are closed pores they are difficult to remove by hot pressing or HIPing. Finally, there is no visible evidence of contamination in composites produced by SHS. Figure 7.14 shows a transmission electron micrograph of an SHS produced  $\text{TiC}_{0.7}$ -20 vol%NiTi composite. The interfaces between the ceramic reinforcement and the matrix are not outlined by impurities as they are in vacuum hot pressed composites (see Figure 4.2). The high reaction temperatures achieved during the SHS effectively drive off all volatile impurities, so that the purity of the product is not limited by the purity of the reactants.

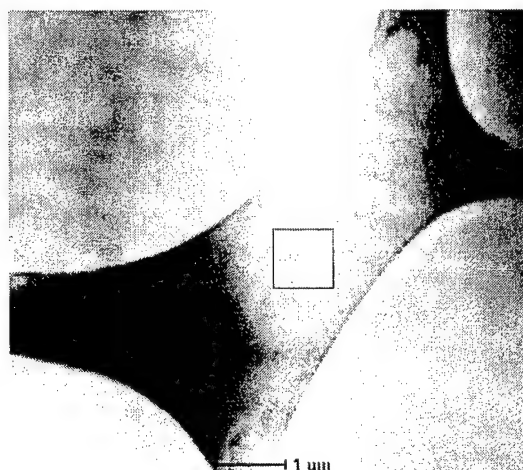


Figure 7.14. Transmission electron micrograph of  $\text{TiC}_{0.7}$ -20vol%NiTi showing the interface between the TiC particles and the NiTi matrix. [Courtesy of C. Echer, NCEM].

### 7.7 Chemistry of Matrix

The NiTi sample from Nitinol Devices and Components was stated by the manufacturer to have a composition of 55.7 wt % Ni, which corresponds to 50.6 atomic % Ni. The composition of this NiTi sample was checked by EDX in the TEM using the HAD detector. The composition was determined using both the k-factors supplied by the Emispec analytical software and those determined by the National Center for Electron Microscopy. Both sets of k-factors provided compositions that matched the manufacturer's reported composition within the 1% experimental uncertainty. Since the match with the manufacturer's reported composition was somewhat closer for the k-factors provided by Emispec, those values ( $K_{\text{Ni}}=1.489$ ,  $K_{\text{Ti}}=1.213$  for the HAD detector) were used for the analysis of the NiTi matrix of the composites. The NiTi sample was not evaluated in the UTW detector, so all data from the UTW detector were multiplied

by normalization factors. These normalization factors were determined by comparing the EDX data from the UTW and HAD detectors taken from the same area of the same sample. Table 7.4 shows the results of the energy dispersive x-ray analysis (EDX) that was performed on the TiC-NiTi composites.

Table 7.4 Composition of matrix of 7.5 cm diameter  $\text{TiC}_{0.7}$ -NiTi composites. The corresponding standard deviations are presented in parentheses.

	Ti atomic percent	Ni atomic percent
20NiTi sample	51.5 ( $\pm 0.7$ )	48.5 ( $\pm 0.7$ )
40NiTi sample	51.2 ( $\pm 1.0$ )	48.8 ( $\pm 1.0$ )
60NiTi sample	48.8 ( $\pm 0.6$ )	51.2 ( $\pm 0.6$ )
80NiTi sample (data acquired in spot mode)	49.7 ( $\pm 0.6$ )	50.3 ( $\pm 0.6$ )
80NiTi aged (data acquired in spot mode)	44.9 ( $\pm 1.5$ )	55.1 ( $\pm 1.5$ )

Figure 7.15 shows a concentration profile for the  $\text{TiC}_{0.7}$ -20NiTi measured by EDX in the transmission electron microscope. The profile starts in a  $\text{TiC}_x$  particle, continues through the NiTi matrix, and then passes through another  $\text{TiC}_x$  particle. In the NiTi matrix, both the Ni and Ti intensities decrease uniformly with one another and with the background spectrum. This reveals that the apparent decline in the Ni and Ti intensities is the result of differences in the thickness of the specimen. The sample gets thinner along the measured profile line, so the overall number of counts measured decreases. The composition of the matrix varies along the profile line between  $\text{Ni}_{47.6}\text{Ti}_{52.4}$  and  $\text{Ni}_{49.0}\text{Ti}_{51.0}$ . The average composition acquired by rastering over several areas of the matrix is  $\text{Ni}_{48.5}\text{Ti}_{51.5}$ , which is rich in titanium. Honma (1987) has shown that the martensitic transformation temperature in NiTi is independent of composition for titanium contents higher than 49.81 at%. The expected  $M_s$  temperature for such a composition is 70 °C. If the EDX measurements taken from a few areas in a thin foil of

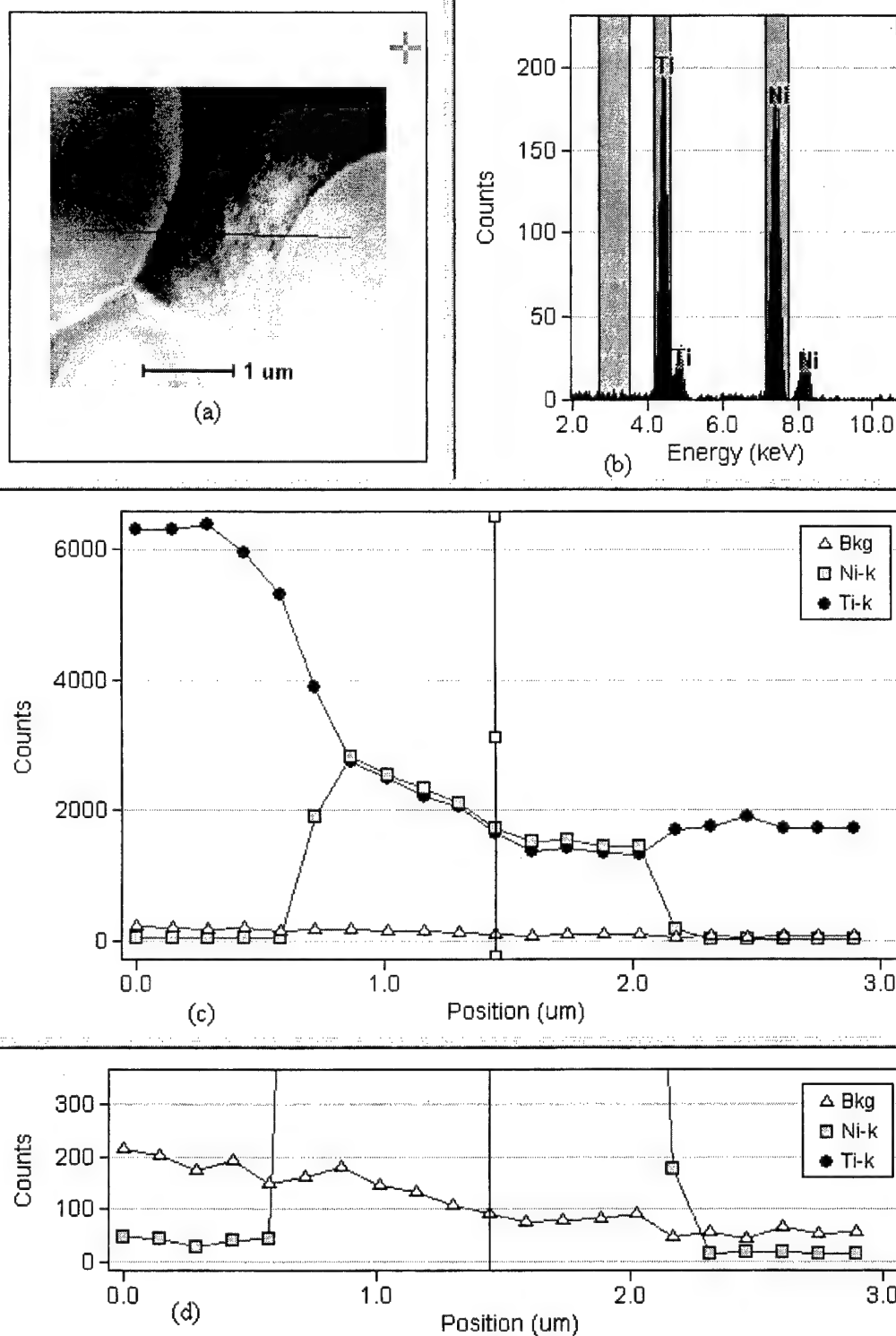


Figure 7.15. Concentration profile for the  $\text{TiC}_{0.7}\text{-20NiTi}$  measured by EDX in the transmission electron microscope. [Courtesy of C. Echer, NCEM].

the  $\text{TiC}_{0.7-20\text{NiTi}}$  sample are representative of the composition of the matrix in the bulk sample, then shifts in the  $M_s$  temperature would not be attributable to chemical effects. Such shifts in the transformation temperature would be the result of the addition of  $\text{TiC}_x$  inclusions.

The data on the composition of the NiTi matrix can also be used to calculate the stoichiometry of the carbide. The reactant powders were mixed with the anticipation of forming  $\text{TiC}_{0.7-20\text{Ni}_{50}\text{Ti}_{50}}$ . The EDX results reveal that the actual composition of the matrix is  $\text{Ni}_{48.5}\text{Ti}_{51.5}$ . Therefore the carbide must not contain as much titanium as expected. The stoichiometry of the carbide calculated from an elemental balance of the equation  $x_{\text{Ti}}\text{Ti} + x_{\text{C}}\text{C} + x_{\text{Ni}}\text{Ni} \rightarrow x_{\text{TiC}}\text{TiC}_x + x_{\text{NiTi}}\text{Ni}_{48.5}\text{Ti}_{51.5}$  is equal to  $\text{TiC}_{0.71}$ .

Figure 7.16 shows a concentration profile for the matrix of a  $\text{TiC}_{0.7-40\text{NiTi}}$  sample. The composition of the matrix varies along the profile line between  $\text{Ni}_{50.1}\text{Ti}_{49.9}$  and  $\text{Ni}_{48.7}\text{Ti}_{51.3}$ . The average composition, acquired by rastering over several areas of the matrix is  $\text{Ni}_{48.8}\text{Ti}_{51.2}$ , which is again rich in titanium. The calculated stoichiometry of the carbide is  $\text{TiC}_{0.72}$ .

Figure 7.17 shows a concentration profile for the matrix of a  $\text{TiC}_{0.7-60\text{NiTi}}$  sample. Since the Ni and Ti intensity profiles mirror the shape of the background spectrum, variations in the number of counts are due primarily to changes in the thickness of the specimen. The composition of the matrix varies along the profile line between  $\text{Ni}_{50.7}\text{Ti}_{49.3}$  and  $\text{Ni}_{51.3}\text{Ti}_{48.7}$ . The average composition acquired by rastering over several areas of the matrix is  $\text{Ni}_{51.2}\text{Ti}_{48.8}$ . The matrix in this sample is rich in nickel. If this composition is representative of bulk  $\text{TiC}_{0.7-60\text{NiTi}}$ , chemical effects can not be ignored. The calculated stoichiometry of the carbide is  $\text{TiC}_{0.66}$ .

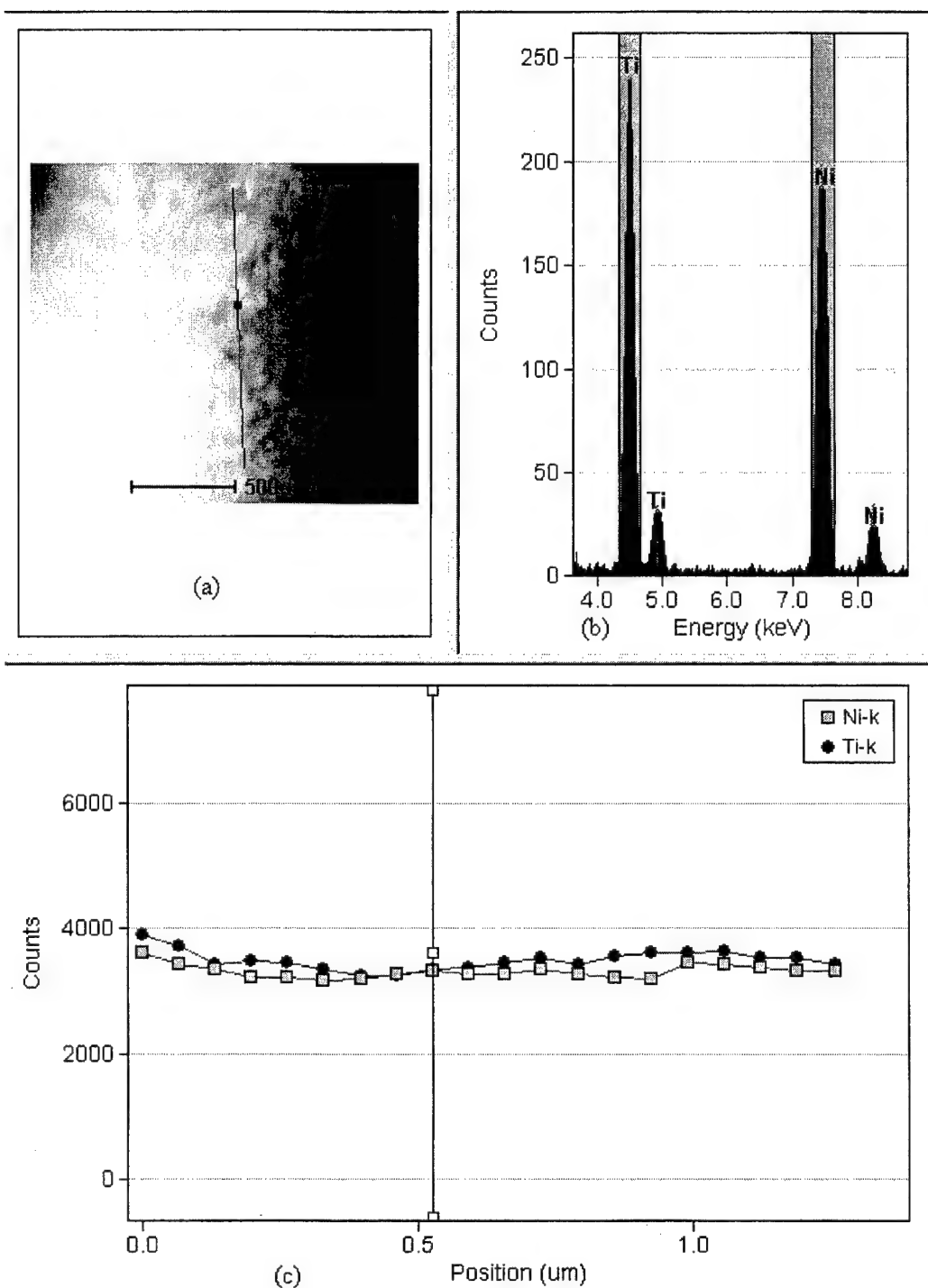


Figure 7.16. Concentration profile for the  $\text{TiC}_{0.7}\text{-40NiTi}$  measured by EDX in the transmission electron microscope [Courtesy of C. Echer, NCEM].

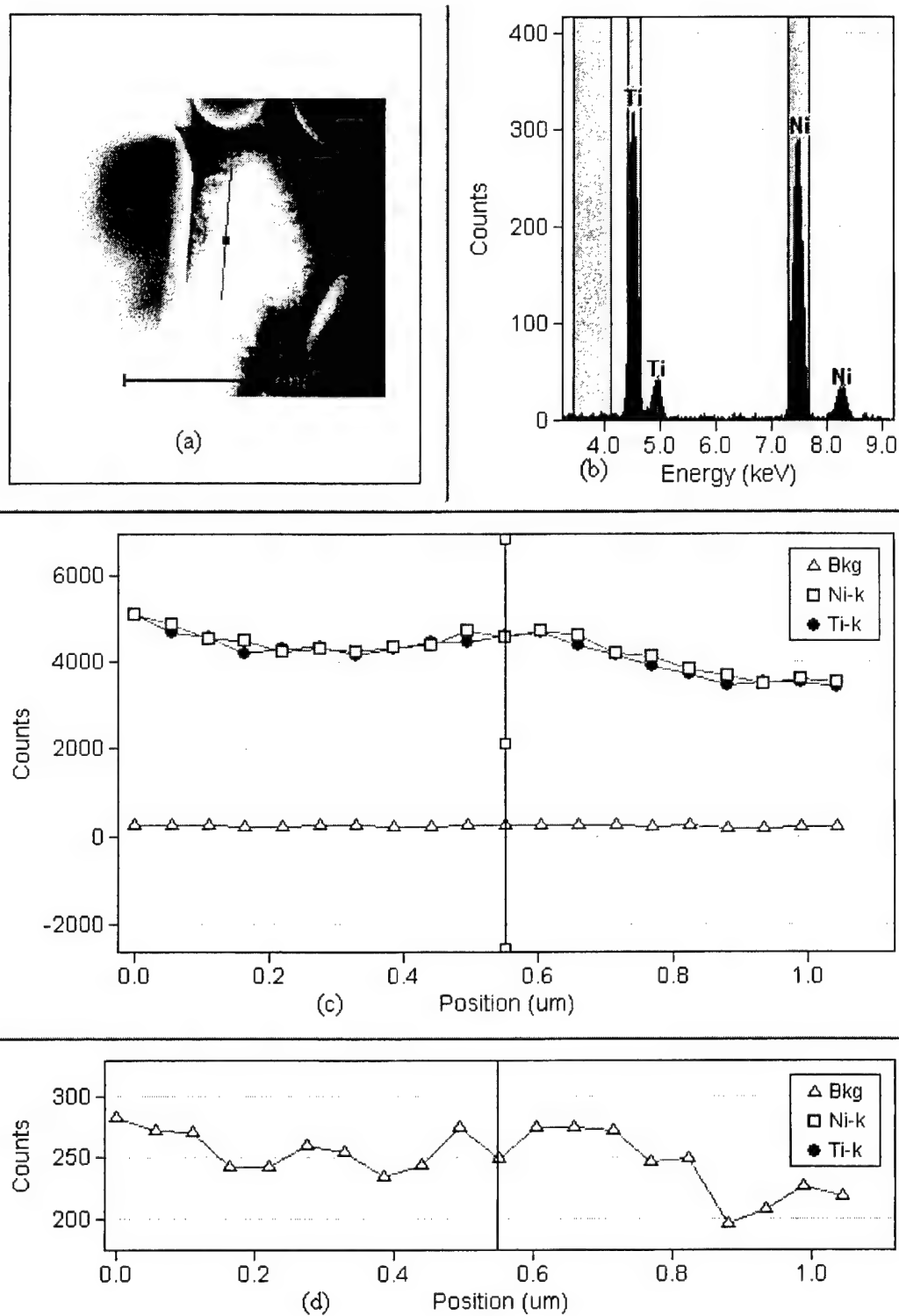


Figure 7.17. Concentration profile for the  $\text{TiC}_{0.7}\text{-60NiTi}$  measured by EDX in the transmission electron microscope [Courtesy of C. Echer, NCEM].

The composition of the as-synthesized and aged  $\text{TiC}_{0.7}$ -80NiTi samples were measured by using the spot mode in the TEM. Each of the values reported in Table 7.4 is the average of three spot measurements. From these limited number of measurements, the matrix of the aged 80NiTi sample appears to have a much higher nickel content than the as synthesized sample. It would be expected that the average matrix composition of the two 80NiTi samples would be the same. However, the spot mode does not raster over an area of matrix to acquire chemical data. Instead, a 600 Å diameter probe remains fixed at one point in the matrix. Since the aged 80NiTi sample was heated in the DSC at 3 °C/min up to 350 °C and held at that temperature for approximately 30 minutes, precipitation of  $\text{Ni}_4\text{Ti}_3$  could have occurred. Such precipitates were not imaged in the transmission electron microscope, but were detected by selected area diffraction (SAD). Figure 7.18 shows a SAD pattern taken from the matrix of the aged 80NiTi sample. The large bright spots, and those appearing at the  $1/3 \langle 110 \rangle_{\text{B}_2}$  are characteristic of the R-phase. The faint spots that appear clustered around the  $\langle 110 \rangle_{\text{B}_2}$  are from  $\text{Ni}_4\text{Ti}_3$  precipitates [Stroz (1997)]. The presence of  $\text{Ni}_4\text{Ti}_3$  precipitates in the aged 80NiTi should cause a variation in matrix composition from point to point. This variation is confirmed by the large standard deviation of composition measurements taken on the aged 80NiTi. The SAD patterns taken of the matrix of as-synthesized 80NiTi did not show the presence of  $\text{Ni}_4\text{Ti}_3$  precipitates; only the R-phase structure of NiTi was present at room temperature.



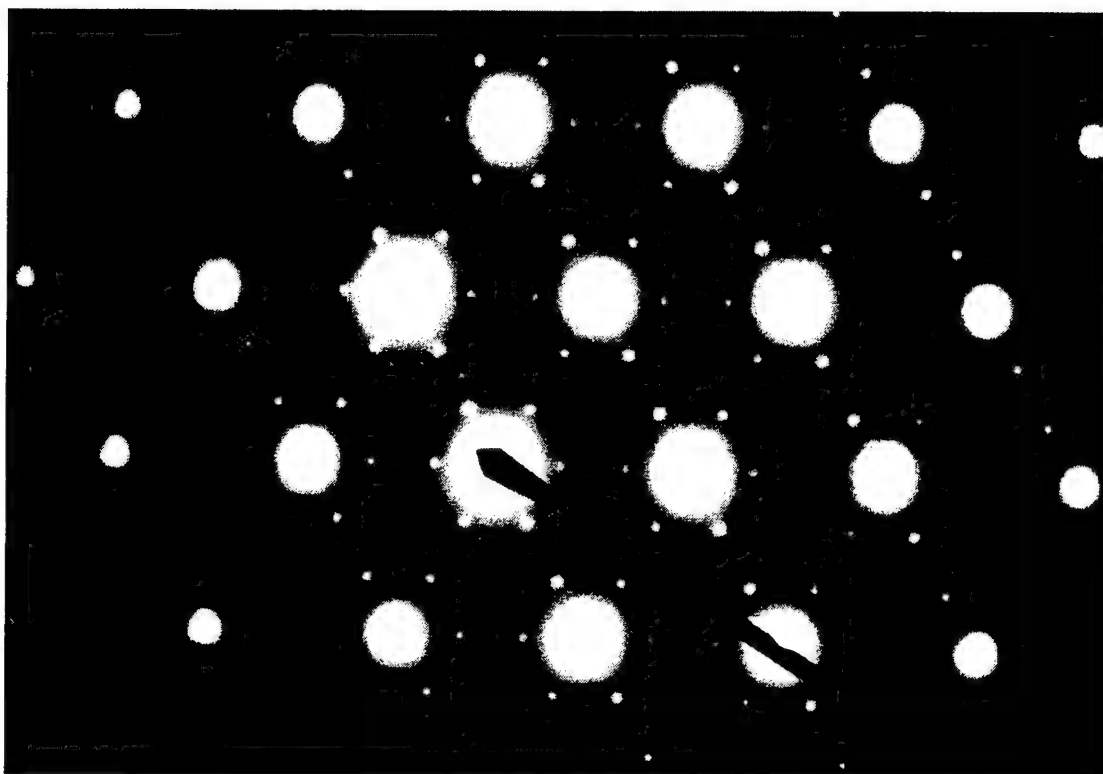


Figure 7.18 SAD pattern taken from the matrix of the aged 80NiTi sample  
[Courtesy of Dr. T Radetic, NCEM].

### 7.8 DSC Results

Figure 7.19 shows the calorimetry spectra for the  $\text{TiC}_{0.7}\text{-NiTi}$  samples during the first thermal cycle. Only one peak was observed in the forward and reverse DSC curves for the 20NiTi and 40NiTi samples. In contrast, the curve for the 60NiTi sample is significantly broader and appears to be composed of multiple peaks. Usually, if the martensitic transformation occurs in multiple steps, i.e.  $\text{B2} \rightarrow \text{R} \rightarrow \text{B19}'$ , then multiple peaks will appear on the DSC curve. However, if the R-phase and B19' transformation temperature ranges overlap, then the multi-step transformation may not be clearly resolved. In such cases, it is also necessary to look at the heat measured upon transformation.

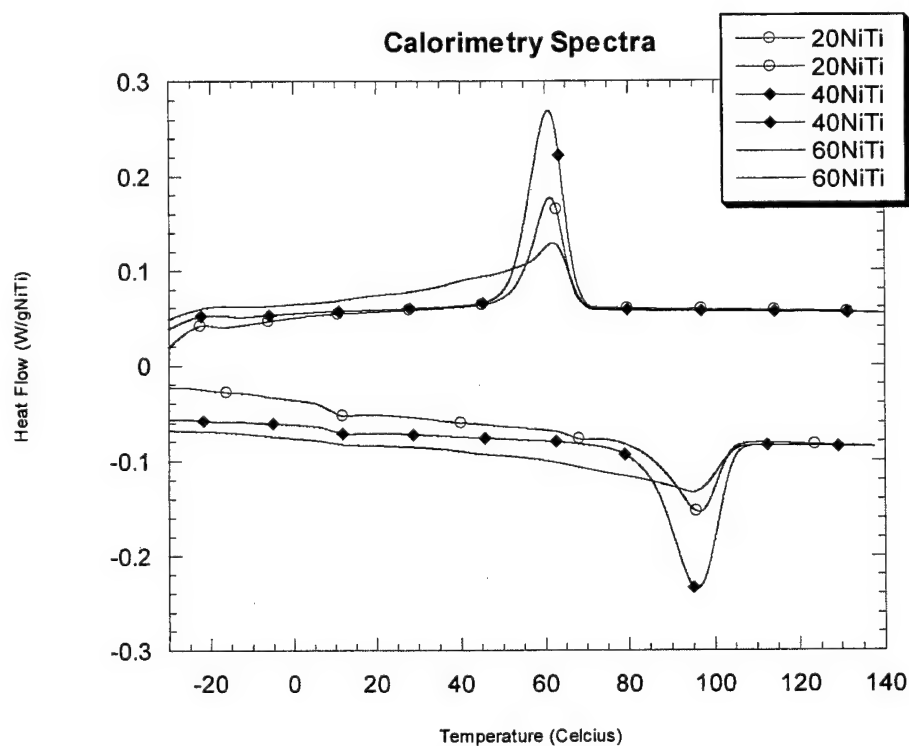


Figure 7.19 Calorimetry spectra for the  $\text{TiC}_{0.7}\text{-NiTi}$  samples during the first thermal cycle (Scanning rate: 5 °C/min) Curves have been shifted along the vertical axis in order to facilitate comparison of transformation temperatures. Samples sectioned from the 7.5 cm diameter, 300 g samples.

The area under the peak in the DSC curve is a measure of the net enthalpy of transformation ( $\Delta h_{net}$ ). Mari and Dunand (1995a) showed that during the forward transformation, from parent to martensite, the net enthalpy  $\Delta h_{net}^{P \rightarrow M}$  released is determined by the equation:

$$-\Delta h_{net}^{P \rightarrow M} = -\Delta h_{ch}^{P \rightarrow M} + \Delta h_{el}^{P \rightarrow M} + \Delta h_d^{P \rightarrow M} + \Delta h_{fr}^{P \rightarrow M}$$

where  $-\Delta h_{ch}^{P \rightarrow M}$  is the chemical enthalpy representing the total energy available for the transformation,  $\Delta h_{el}^{P \rightarrow M}$  is the stored elastic energy,  $\Delta h_d^{P \rightarrow M}$  is the energy stored in defects, and  $\Delta h_{fr}^{P \rightarrow M}$  is the frictional work not dissipated as irreversible heat. During the reverse transformation the net enthalpy  $\Delta h_{net}^{M \rightarrow P}$  absorbed is

$$\Delta h_{net}^{M \rightarrow P} = +\Delta h_{ch}^{M \rightarrow P} - \Delta h_{el}^{M \rightarrow P} + \Delta h_d^{M \rightarrow P} + \Delta h_{fr}^{M \rightarrow P}$$

Experiments by Mari and Dunand (1995a) have shown that the addition of TiC particles into NiTi reduces the measured net enthalpy of transformation  $\Delta h_{net}$  during both the forward and reverse transformation. Their thermodynamic calculations used to quantify  $\Delta h_{el}$  reveal that only a fraction of the observed decrease in  $\Delta h_{net}$  can be attributed to the elastic stored energy. The remaining decrease must result from incomplete transformation. Therefore, to a first approximation, the measured net enthalpy  $\Delta h_{net}$  from the calorimetry spectra in Figure 7.19 can be assumed to be a measure of the transformed fraction of martensite.

Table 7.5 lists the measured net enthalpy  $\Delta h_{net}$  for the samples during the forward transformation. By comparing these values with the expected energy release for NiTi

phase transformations, the volume fraction of martensite formed can be estimated. The expected energy release for the  $B2 \rightarrow R$  transformation is  $-3.75$  J/g and the expected energy release for the  $R \rightarrow B19'$  transformation is  $-25.5$  J/g [Goo and Sinclair (1985)]. Since the room temperature XRD scans (Figure 7.7) show the presence of the R-phase in all  $\text{TiC}_{0.7}$ -NiTi composites, the multi-step transformation  $B2 \rightarrow R \rightarrow B19'$  is assumed to occur in the DSC. The volume fraction of B19' formed during cooling is calculated by assuming that the matrix transforms completely to the R-phase before transforming to the B19' phase. The results are shown in Table 7.5.

Table 7.5. Measured net enthalpy of transformation during cooling and estimate of fraction of martensite formed.

	20vol%NiTi	40vol%NiTi	60vol%NiTi	80vol%NiTi
$\Delta h_{net}^{P \rightarrow M}$	-12.6 J/g NiTi	-25.2 J/g NiTi	-22.6 J/g NiTi	-6.5 J/g NiTi
Energy $B2 \rightarrow R$	-3.75 J/g NiTi	-3.75 J/g NiTi	-3.75 J/g NiTi	-3.75 J/g NiTi
Energy available for $R \rightarrow B19'$	-8.8 J/g NiTi	-21.4 J/g NiTi	-18.8 J/g NiTi	2.7 J/gNiTi
Estimated fraction of matrix that transformed to B19'	0.35	0.84	0.74	0.11

These energy calculations reveal that the R-phase and B19' forward transformations overlap. Even though only one peak is observed in the DSC curves during cooling of the 20NiTi and 40NiTi samples, multi-step transformations are occurring. This overlap makes the definition of distinct transformation temperatures somewhat difficult. For example, the peak onset temperature for the 20NiTi sample upon cooling is  $67^\circ\text{C}$  (as shown in Figure 7.19) and this can be attributed to the

beginning of R-phase formation ( $R_s$ ). The peak then returns to the baseline at 52 °C. At first glance this temperature would appear to mark the end of the B2  $\rightarrow$  R transformation and should be designated  $R_f$ . However, the energy calculations in Table 7.5 reveal that sufficient energy was released to not only completely transform B2 to R, but to also transform 35% of the matrix from R to B19'. The  $R_f$  and  $M_s$  temperatures cannot be distinguished. In Table 7.6 the peak start and finish temperatures are listed. The peak finish temperature upon cooling has been labeled as  $R_f$ , with the understanding that this most probably marks the lower bound temperature for completion of the B2 to R-phase transformation. The  $M_s$  temperature is not defined.

Table 7.6 Transformation temperatures measured by differential scanning calorimetry

	20NiTi	40NiTi	60NiTi	80NiTi	80NiTi (aged)
$R_s$	67 °C	67 °C	69 °C	16 °C	48 °C
$R_f$	52 °C	51 °C	25 °C		24 °C
$T_s$	75 °C	85 °C	63 °C		30 °C
$T_f$				34 °C	55 °C
$A_s$	85 °C				
$A_f$	105 °C	104 °C	104 °C		

Figure 7.19 also shows the calorimetry spectra obtained during heating. The endothermic peaks represent the reversion of the martensite to the parent B2 structure. In-situ TEM experiments (discussed in Section 7.9) reveal that the R phase regions are the first to transform. Then at a slightly higher temperature, the B19' regions begin to transform directly to B2 phase without passing through the intermediate R-phase.

The DSC curve for the 20NiTi curve, shown again in Figure 7.20, reveals a complicated structure. Besides the prominent peak between 83 °C and 104 °C, there are two smaller peaks, one between 6 °C and 20 °C, and another starting at 62 °C. Since NiTi martensitic transformations are thermoelastic, the reverse transformation always occurs at a higher temperature than the forward transformation. Therefore, the small peak between 6 °C and 20 °C cannot be attributed to the reverse transformation of any R-phase that formed during the first thermal cycle. Based on the observation that the R-phase has a hysteresis of less than 2 °C [Fukuda *et al.* (1992)], the small peak starting at approximately 62 °C is associated with the R → B2 transformation. The large peak is attributed to the B19' → B2 transformation

The cause of the small peak between 6 °C and 20 °C is not clear. It may be from the reverse transformation of a small amount of R or B19' martensite that was retained in the matrix at 150 °C. As shown in Table 7.7, the total energy absorbed during the reverse transformation exceeds the energy released during the forward transformation. This reveals that the original assumption that the matrix was completely B2 at 150 °C was incorrect. Even though the temperature exceeds  $A_f$ , the matrix must be composed of both B2 and martensite.

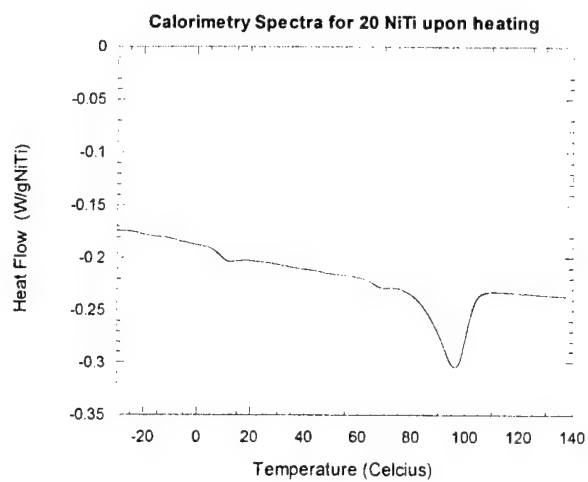


Figure 7.20 The calorimetry spectra for 20NiTi upon heating.

Table 7.7. Measured net enthalpy of transformation during heating

	20vol%NiTi	40vol%NiTi	60vol%NiTi	80vol%NiTi
$\Delta h_{net}^{M \rightarrow P}$	14.4 J/g NiTi	25.5 J/g NiTi		8.6 J/g NiTi

Mari and Dunand (1995) have also reported a greater  $\Delta h_{net}$  upon reverse transformation than upon forward transformation in TiC-NiTi composites. With increasing number of thermal cycles, they observed a decrease in the measured transformation enthalpy. Their calculations of elastic stored energy could only account for a fraction of the observed decrease, so they attributed the missing energy to an increasing fraction of nontransforming phase. They proposed that this nontransforming phase is stabilized by dislocations introduced to relax the misfit stresses between the particles and matrix.

The measured transformation temperatures upon heating the TiC<sub>0.7</sub>-NiTi composites are listed Table 7.6. The onset temperature for the  $R \rightarrow B2$  transformation is designated as  $T_s$ . Due to peak overlap, the  $R \rightarrow B2$  finish temperature cannot be resolved in Figure 7.19 and is consequently not listed. The  $B19' \rightarrow B2$  start and finish temperatures are listed as  $M_s$  and  $M_f$ , respectively. The measured net enthalpy  $\Delta h_{net}$  for the samples during the reverse transformation are listed in Table 7.7. No energy value is reported for the 60 NiTi sample because the baseline was not well defined.

Figure 7.21 shows the DSC curves for the as-synthesized 80NiTi sample. The measured energy during the forward transformation (listed in Table 7.5) is significantly smaller than in the other composites, indicating that only a small fraction of the matrix transformed to B19'. The  $M_s$  temperature of the  $R \rightarrow B19'$  transformation must be near the lowest temperature reached in the DSC ( $-50^\circ\text{C}$ ). Mari and Dunand (1995a) showed that in TiC-NiTi composites with low volume fractions of reinforcement, the  $M_s$  is unaffected by the particles and is the same as in unreinforced NiTi of the same



composition. This would indicate that the bulk as-synthesized 80NiTi has a nickel content of approximately of 50.74 at% [Honma (1997)], which is within the uncertainty of the composition measured by EDX.

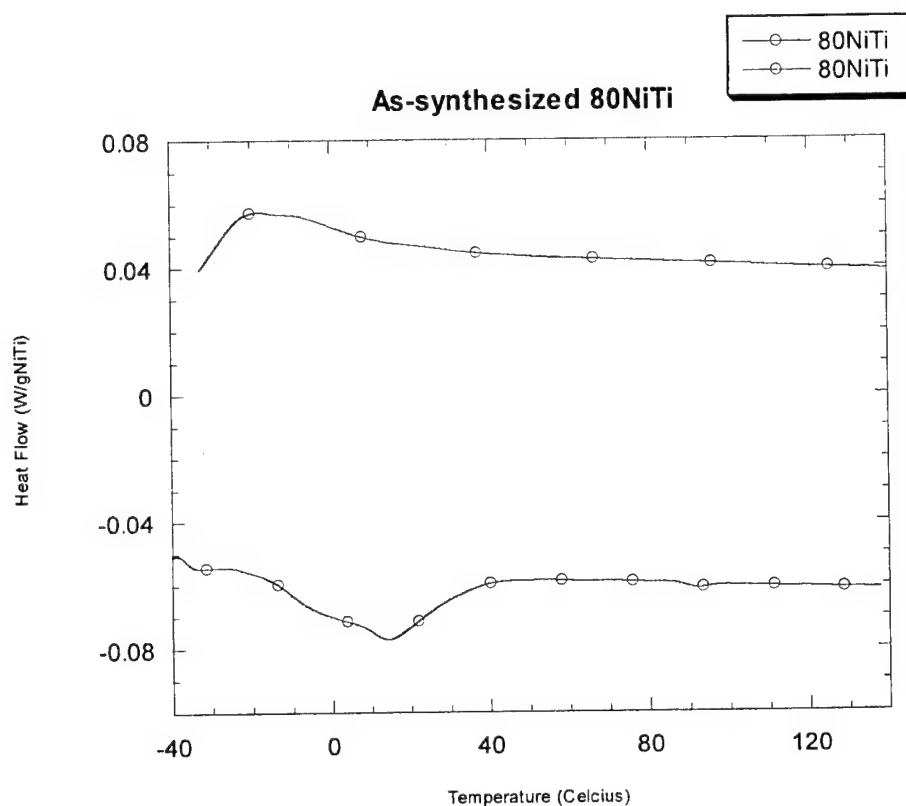


Figure 7.21 Calorimetry spectra for as-synthesized 80NiTi sample during the first thermal cycle (Scanning rate: 5 °C/min) .

Figure 7.22 shows the DSC curves for the aged 80NiTi sample. The R-phase transformation occurs at a higher temperature than in the as-synthesized 80NiTi. Based on the SAD image shown in Figure 7.18, it is apparent that the aging process has caused precipitation of the  $\text{Ni}_4\text{Ti}_3$ . Formation of nickel rich precipitates increases the martensitic transformation temperatures, by shifting the nickel content of the matrix towards the stoichiometric composition. It is worth noting that the expected increase in titanium content of the NiTi matrix was not reflected in the EDX measurements reported in Table 7.4. Although the composition data were acquired in the spot mode, it was not possible to determine if the probe was focused on the NiTi matrix or on the  $\text{Ni}_4\text{Ti}_3$  precipitates, because the precipitates were not visible in the image.

The energy of the of peak corresponding to the  $B2 \rightarrow R$  transformation in Figure 7.22 is -4.3 J/g. This indicates that some B19' formation has also occurred. The energy of the reverse  $R \rightarrow B2$  transformation is 7.3 J/g. Since this value exceeds the energy released during the forward transformation, it is evident that there was some B19' above 150 °C. By comparing these transformation energies with those given in Table 7.5, it is also evident that the matrix of aged 80NiTi sample releases and absorbs less energy than the matrix of the as-synthesized 80NiTi. This is consistent with the formation of  $\text{Ni}_4\text{Ti}_3$  precipitates. These precipitates do not undergo martensitic transformation

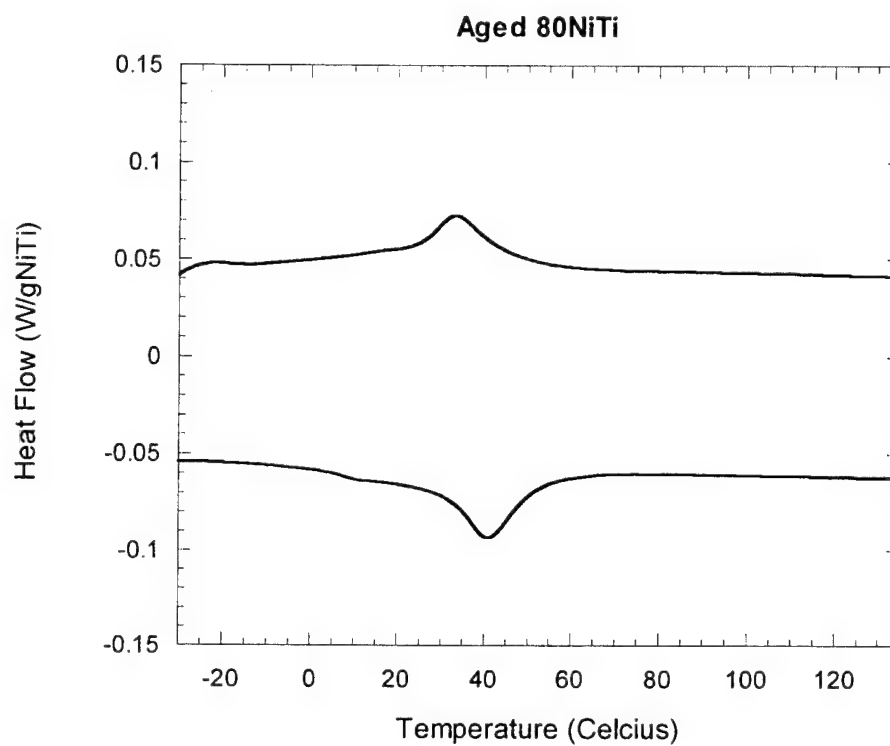


Figure 7.22 Calorimetry spectra for aged 80NiTi sample (Scanning rate: 5 °C/min) .

## 7.9 In-Situ TEM

In-situ heating and cooling was used to investigate the transformation path, martensite nucleation and growth, and the effect of carbide particles on the movement of NiTi transformation fronts. The samples were first heated to 110 °C (above the  $A_f$  temperature). This process was performed in stages in order to record selected area diffraction patterns, bright field images, and dark field images at specific temperatures. The experiments were also recorded on video. Then the samples were cooled in stages to room temperature in order to observe the martensitic forward temperature. Again selected area diffraction patterns, bright field images, and dark field images at specific temperatures were recorded. In most cases the  $R \rightarrow B19'$  transformation was incomplete at room temperature, so liquid nitrogen was added to cool the specimen even further.

Upon heating the R-phase regions of the matrix are the first ones to transform to the B2 phase. Then, as the temperature is increased, the B19' regions transform directly to the B2 phase, without passing through the R-phase. This transformation behavior was recorded in the 20NiTi, 40NiTi, and 60NiTi samples. In the 80NiTi sample, only the R-phase was present at room temperature. Consequently only the  $R \rightarrow B2$  transformation was observed.

During cooling, the  $B2 \rightarrow R$  transformation occurs first. This transformation is clearly identified by the presence of spots at the  $1/3 \langle 110 \rangle_{B2}$  positions in the SAD. With further cooling, usually to temperatures lower than room temperature, B19' martensite appears. Figure 7.23 shows the  $R \rightarrow B19'$  transformation in 20NiTi. The specimen has been tilted so that the B19' appears with a dark contrast and the R-phase has a lighter

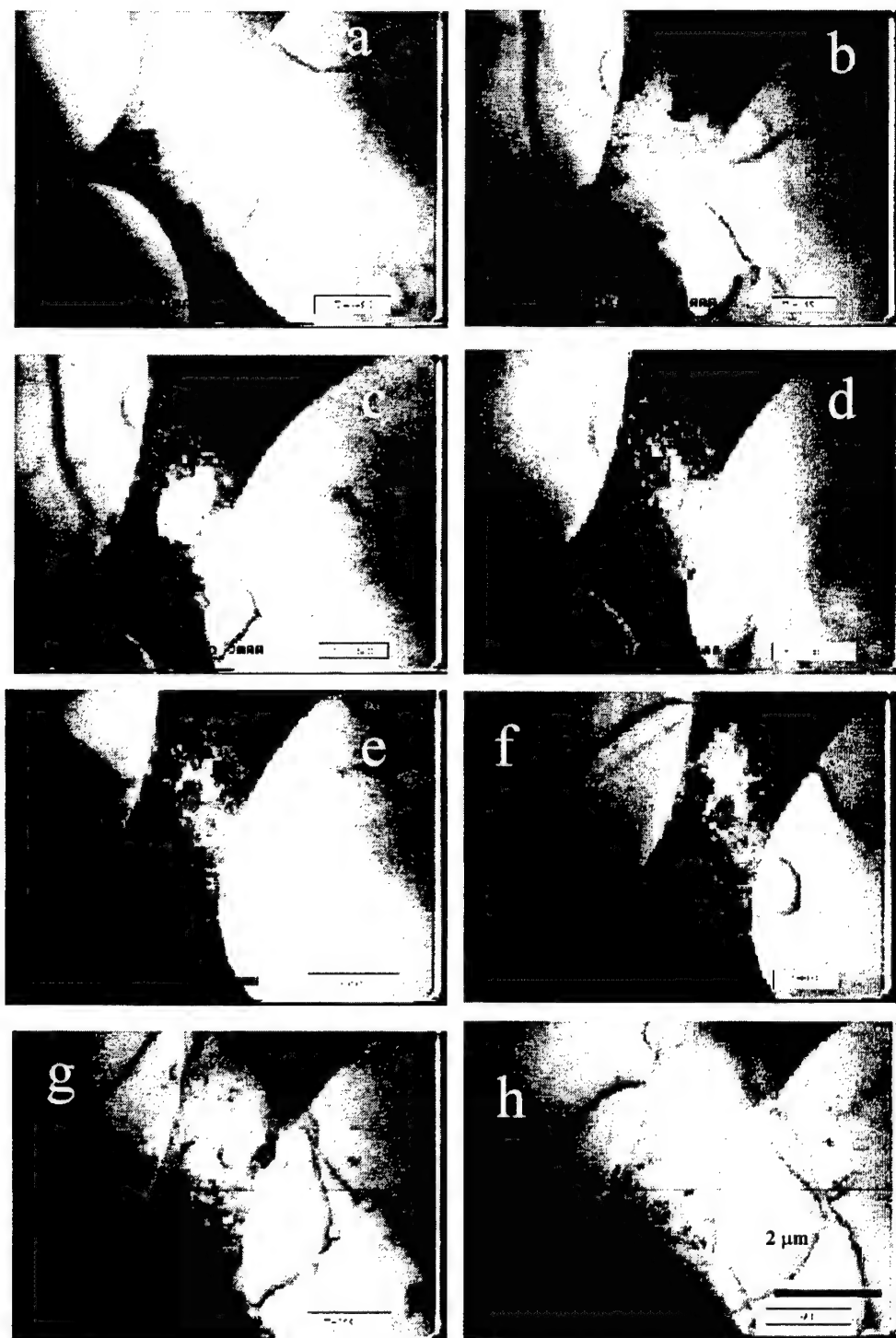


Figure 7.23 In-situ experiments in 20NiTi. (a)-(d)  $R \rightarrow B19'$  transformation upon cooling. (e)-(h)  $B19' \rightarrow B2$  transformation upon heating. (a)  $T = -45^\circ\text{C}$  (b)  $T = -65^\circ\text{C}$  (c)  $T = -86^\circ\text{C}$  (d)  $T = -112^\circ\text{C}$  (e)  $T = 74^\circ\text{C}$  (f)  $T = 80^\circ\text{C}$  (g)  $T = 85^\circ\text{C}$  (h)  $T = 86^\circ\text{C}$  [Courtesy of Dr. T Radetic, NCEM].

contrast. As shown in Fig 7.23(a), the B19' nucleates in the narrowest corridors between the carbide particles. It grows along the carbide particle interfaces and then into the wider regions of matrix. In Figure 7.23(c) the remaining R-phase appears as an island surrounded B19'. At -112 C (Fig 7.23(d)) only the smallest amount of retained R-phase remains. Upon heating, the last B19' martensite plates to form are among the first to revert back to the parent B2 structure. The transformation front moves from the center of the matrix toward the carbide particles.

Figure 7.24 shows the  $R \rightarrow B19'$  transformation in another region of the 20NiTi specimen. In this case the martensite nucleates at the intersection of the TiC interface and a NiTi grain boundary. It grows along the NiTi grain boundary and then spreads throughout matrix.

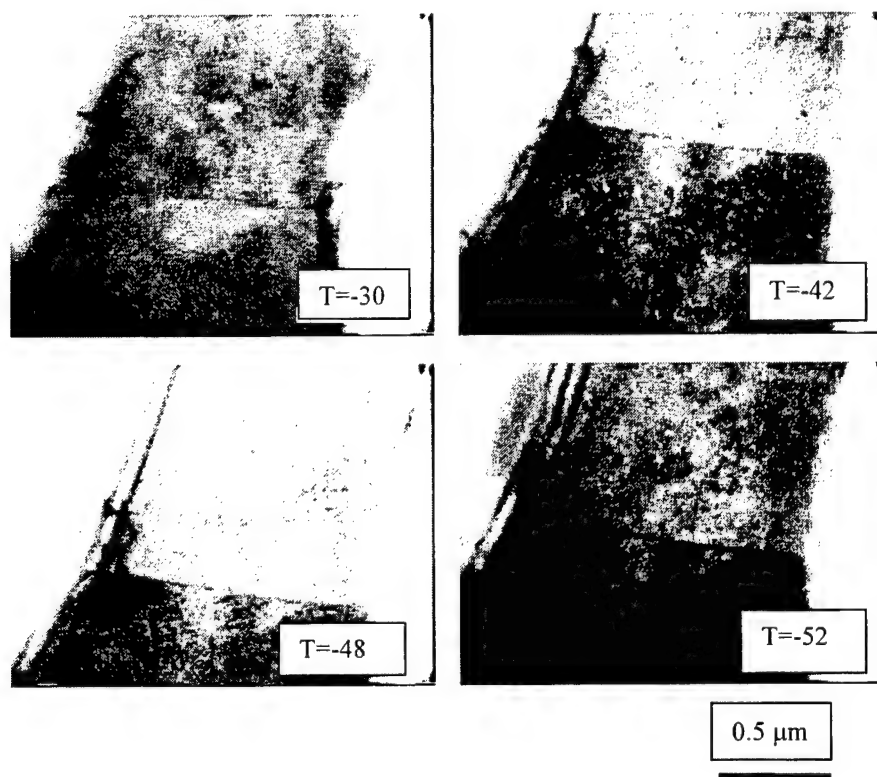


Figure 7.24 Nucleation of B19' at the intersection of a TiC interface and a NiTi grain boundary in 20NiTi. [Courtesy of Dr. T Radetic, NCEM].

Similar transformation behavior to that described for the 20NiTi was also observed in the 40NiTi and 60NiTi composites, although the temperatures at which the transformations occurred differed. The  $R \rightarrow B19'$  and  $B19' \rightarrow R$  transformation was never in the 80NiTi sample. The transformation temperatures observed in the TEM are listed in Table 7.8

Table 7.8 The transformation temperatures measured in the DSC and in the TEM.

	20NiTi		40NiTi		60NiTi		80NiTi		80NiTi	
	DSC	TEM	DSC	TEM	DSC	TEM	DSC	TEM	DSC	TEM
$R_s$	67	40-50	67	42	69	22-41	16	15	43	
$R_f$	52	>29	51		25				26	
$M_s$		-12		34		-25		<-138		<-150
$M_f$		<-108		-13		<-104				
$T_s$	75	56	85		63	50		95		
$T_f$							34	108		
$A_s$	85	71		94		70				
$A_f$	105	99	104	101	104	80				



These in-situ TEM experiments clearly indicate that TiC particles affect B19' martensite nucleation in 20NiTi, 40NiTi and 60NiTi composites. . The martensite nucleates either in the narrowest corridors between the carbide particles or at the intersection of particle interfaces with NiTi grain boundaries. Therefore, it is expected that an increased volume fraction of carbide particles would increase  $M_s$ . However, in studies on TiC-NiTi composites manufactured with a carefully controlled chemistry, no increase in the  $M_s$  was observed with increasing particle content up to 20% [Mari *et al* (1995b)]

Mari *et al.* (1995b) also noted a systematic decrease in  $M_f$  with increasing particle content. They argued that the  $M_f$  temperature is reduced with increasing particle content, because the TiC particles are obstacles for the propagation of martensite plates. However, in-situ TEM reveals that the growth of B19' is limited by the impingement of the martensite variants with one another. The martensite transformation fronts do not sweep past the carbide particles. They move outward away from them.

## 7.10 Mechanical Tests

Since interest in TiC-NiTi composites is driven by its potential use as an armor material, a number of mechanical tests were performed. Focus was placed on the  $\text{TiC}_{0.7}$ -30NiTi composite, because it contains a large volume fraction of ceramic particles. Table 7.9 shows the transformation temperatures that were measured by acquiring calorimetry spectra between 20 °C and 150 °C. Following the method outlined in Section 7.8, the sample matrix was estimated to be 82% R-phase and 18% B19' at room temperature.

Table 7.9 Transformation temperatures in  $\text{TiC}_{0.7}$ -30NiTi measured by acquiring calorimetry spectra between 20 °C and 150 °C. (It is worth noting that the this composite was formed from an original powder compact that was only 150 g in mass and 6.4 cm in diameter)

	$\text{TiC}_{0.7}$ -30NiTi
$R_s$	58 °C
$R_f$	47 °C
$T_s$	63 °C
$A_s$	73 °C
$A_f$	90 °C

Quasi-static compression tests were performed above and below the  $R_s$  temperature in order to determine if stress induced transformation or variant reorientation could be detected. Since small strains needed to be measured, strain gages were attached to the test specimens as outlined in Section 6.4. Figure 7.25 shows the stress-strain curve of the 30NiTi sample tested at room temperature. Upon unloading, the strain did not return to zero, during the first thermal cycle, as would be expected if the sample behaves completely elastically within this pressure range. During the second compression test on the same sample, the strain returned to zero upon unloading. It is possible that residual stresses in the adhesive used to attach the strain gages are responsible for the nonzero strain after the compression sequence. In order to confirm this, it would be necessary to perform quasi-static compression tests on monolithic ceramic samples. A monolithic ceramic will deform elastically. Therefore any residual strain that appears after unloading during the first compression cycle could be attributed to effects from the adhesive. Such tests are important, because if the matrix in the TiC-30NiTi composites undergoes stress induced  $R \rightarrow B19'$  transformation or B19' variant reorientation, there will also be a residual strain upon unloading.

Fukami-Ushiro and co-workers (1996A) have observed the formation of stress-induced martensite during quasi-static compression of a TiC-80NiTi composite tested at a temperature of  $A_f + 5K$ . The  $B2 \rightarrow B19'$  transformation began at stresses as low as 320 MPa and was detected by yielding in the stress-strain curve. They observed strains greater than 4% in composites tested to a maximum pressure of approximately 700 MPa. Upon unloading, they did not observe superelastic recovery, because the martensite was strain stabilized.

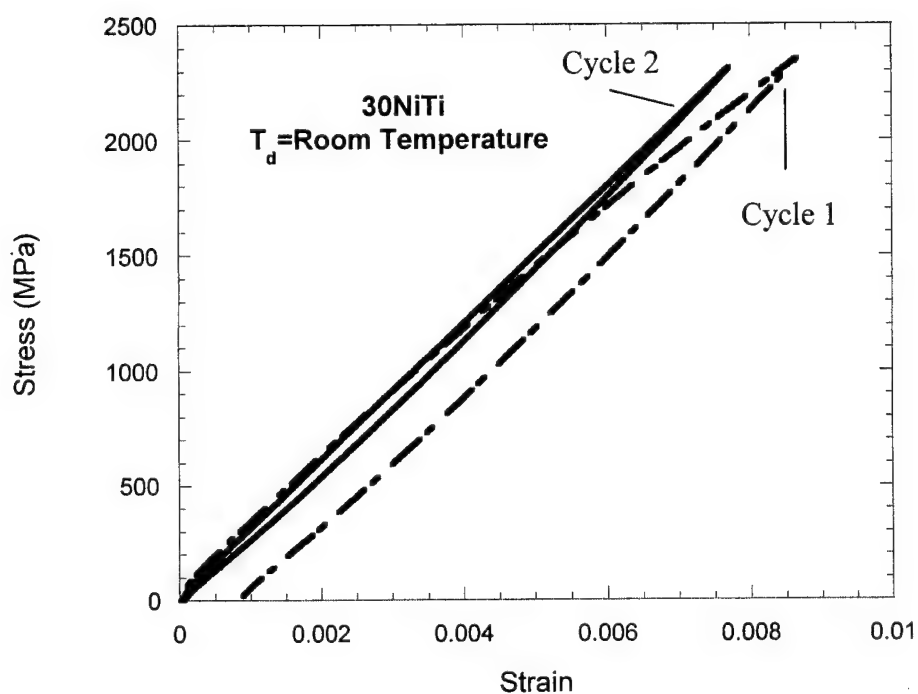


Figure 7.25 The stress-strain curve for the 30NiTi composite tested at a temperature room temperature and loaded to approximately 2350 MPa . (a) First compression cycle. The small remaining strain upon unloading may to result from residual stresses in the adhesive used to attach the strain gage. (b) Second compression cycle

In the 30 NiTi composites studied in the present work, the carbide particles are interconnected. They form a rigid skeleton that resists deformation. These ceramic particles will bear the majority of the load, so high external pressures are expected to be required to force the formation of stress induced martensite in the matrix. It may even be possible that sample failure will occur before the transformation can be detected.

Several quasi-static tests were also performed at higher temperatures. The same 30NiTi sample that was tested in Figure 7.25 was heated to  $T_d = A_f + 20$  °C and then loaded to a maximum pressure of 2608 MPa and strain of 0.93%. Figure 7.26 shows the results. The stress-strain curve remains linear until approximately 0.8% strain. Then, there is an apparent bend in the curve. The yield point is at the maximum stress (2350 MPa) obtained in Figure 7.25. Unfortunately, it is still not clear if this strain is from the adhesive or from the formation of stress induced martensite. However, it is quite likely to be from the adhesive, because any B19' that might have formed as a result of compressive loading at room temperature would be strain stabilized [Fukami-Ushiro and Dunand. (1996b)]. It would not be expected to revert to B2 upon heating to  $T_d = A_f + 20$  °C. Therefore, only those regions of R-phase that did not transform to B19' previously, could revert to B2 during heating and contribute to the observed yield behavior. Since the temperature is now above  $A_f$ , the measured yield point should be at a stress higher than the maximum stress reached in the previous test, not at the same stress.

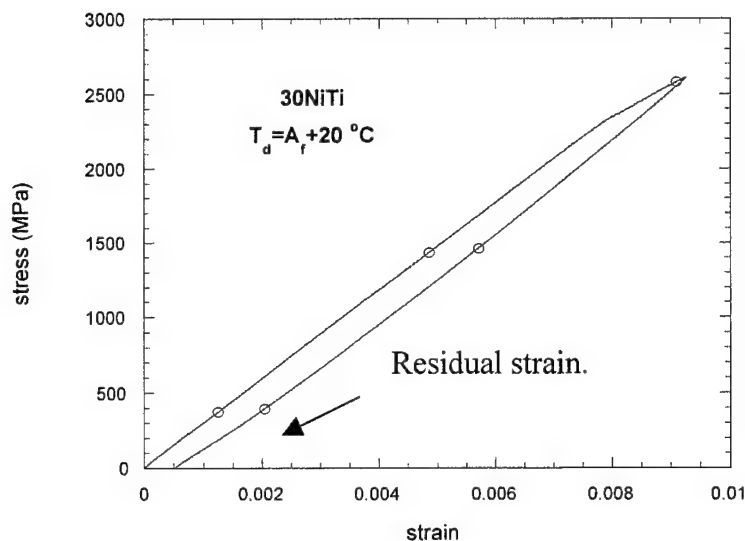


Figure 7.26 The stress strain curve for another 30NiTi sample tested at  $T_d = A_f + 20^\circ\text{C}$  and loaded to 2600 MPa.

The elastic modulus of the 30NiTi sample, as determined from the slope of the stress-strain curve in Figure 7.26 is  $E_{\text{load}} = 300 \text{ GPa}$ . The predicted modulus, calculated by the rule of mixtures, is 329 GPa for a 30NiTi composite with a B2 matrix and 315 GPa for a composite with a B19' matrix. The compressive strength, measured by testing a sample to failure at room temperature, is 2.8 GPa. The strain to failure was 0.96%

Figure 7.27. shows the stress-strain curves for a 30NiTi specimen tested dynamically in the split Hopkinson bar at an average strain rate of  $10^2/\text{sec}$ . In this case, the strains and stresses were measured by strain gages on the incident and transmission bars. The actual specimen was not instrumented with a strain gage. Since the sample did not fail, both the loading and unloading behavior were recorded. However, for more accurate measurements, strain gages should be directly attached to the test specimen.

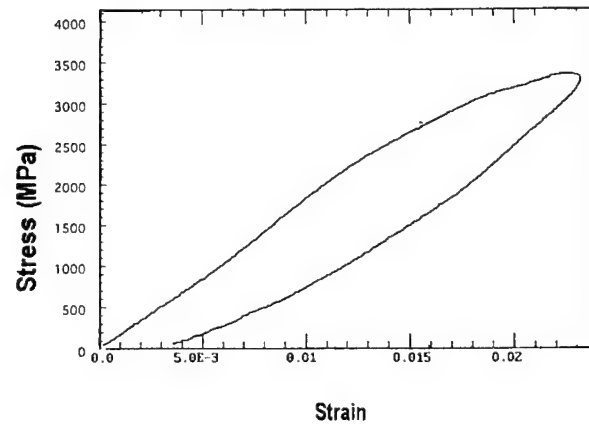


Figure 7.27 Stress-strain curve for  $\text{TiC}_{0.7}$ -30vol%NiTi tested dynamically at a strain rate of  $10^2/\text{sec}$ .

In both quasi-static and dynamic tests where the 30NiTi specimens failed, fracture was by axial splitting. Figure 7.28 shows the fracture surface, in which there is very little evidence of ductile behavior in the NiTi. It appears to be essentially brittle fracture in which the  $\text{TiC}_x$  particles have cleaved transgranularly. It is important to note that there is no evidence that the material prefers to fail along the interface between the  $\text{TiC}_x$  inclusions and the NiTi matrix. This supports the hypothesis that the  $\text{TiC}_x$  particles are well bonded to the NiTi matrix and that the interface between the two phases is strong.

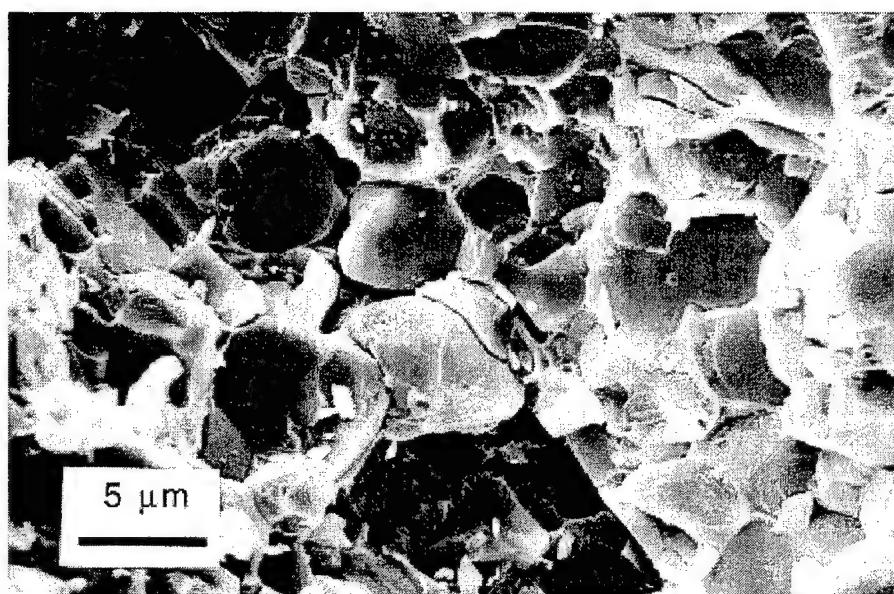


Figure 7.28 Fracture surface of failed TiC<sub>0.7</sub>-30vol%NiTi



The results from preliminary 4-point bend tests are listed in Table 7.10. The samples for the bend tests were taken from a different plate than that used for the quasi-static tests. Some of the bend test samples had surface flaws and pores. Those specimens with surface flaws failed at much lower loads than those specimens with no apparent defects. The average flexural strength for specimens with no visible flaws is 1047 MPa with a standard deviation of 90 MPa.

Table 7.10 Flexural strength of  $\text{TiC}_{0.7}$ -30vol%NiTi

Sample Number	Presence of Visible Surface Flaws	Flexural Strength (MPa)
1	yes	204
2	no	1095
3	no	1102
4	yes	288
5	yes	715
6	no	943

The measured Vickers hardness values for  $\text{TiC}_{0.7}$ -NiTi composites (3 cm diameter samples) of various volume fractions of NiTi are listed in Table 7.11. As expected the hardness decreases with increasing volume fraction of NiTi. In Figure 7.29, these hardness values are compared to the monolithic ceramic.

Table 7.11 Vickers hardness of  $\text{TiC}_{0.7}$ -NiTi composites.

Vol%NiTi	Vickers Hardness (GPa)	Standard Deviation
30	10.0	0.4
40	9.3	0.25
50	8.8	0.2

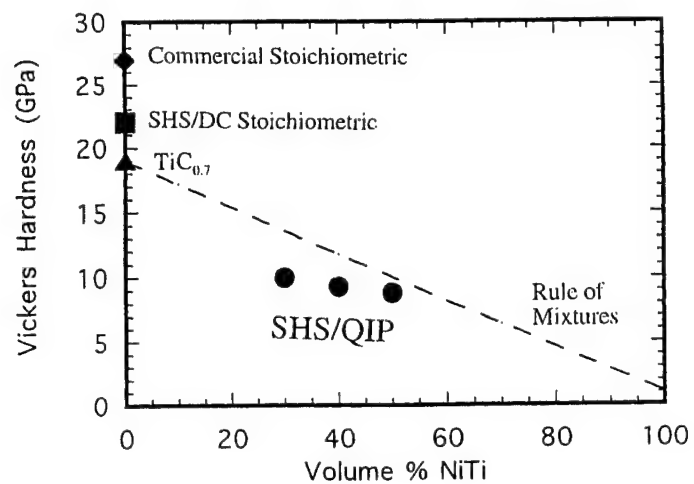


Figure 7.29 Vickers hardness of SHS/QIP  $\text{TiC}_{0.7}$ -NiTi composites compared to the hardness of monolithic TiC and  $\text{TiC}_{0.7}$  [LaSalvia *et al.* (1992) and Kosolapova (1986)]

Several ballistic impact tests were also performed. As described in Section 6.4, two different configurations were used. In the first configuration, the TiC-NiTi target was simply taped to a large steel back plate. There was no lateral confinement. A 1090 steel projectile, 25 mm in length and 3.9 mm in diameter, was fired at a velocity of 500 m/s. Since the projectile mass was 0.0019 kg, the energy of impact was 240 Joules. The composite target plate was 6mm thick and 40 mm in diameter. Figure 7.30 shows the steel projectile and 30NiTi target and after impact. The projectile shattered into many pieces, while the 30NiTi composite suffered no visible penetration and did not crack.

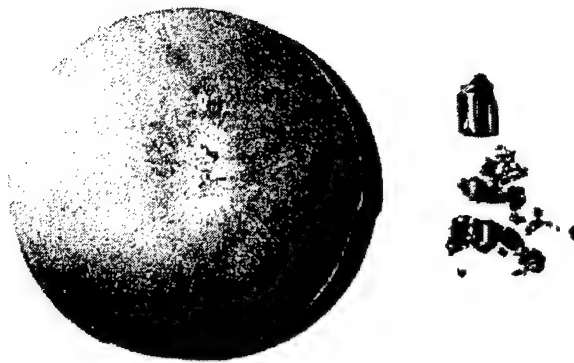


Figure 7.30 Photograph of TiC<sub>0.7</sub>-30 vol%NiTi plate and steel projectile after impact without lateral confinement.

In the other test configuration (Configuration 2, Figure 6.8) the targets were press fit into 1.9 cm thick steel plates. The projectile diameter was 12.7 mm, which was greater than 30% of the diameter of the target. The projectile was cylindro-conical in shape, 38.1 mm in length, and 0.031 kg in weight. Table 7.12 shows a summary of the ballistic tests performed in this configuration.

Table 7.12 Summary of the ballistic tests performed in Configuration 2.

	20NiTi	30NiTi	60NiTi	
$R_s$	58 °C	57 °C	61 °C	63 °C
Thickness	5.8 mm	4.3 mm	3.9 mm	5.1 mm
Density	4.81 g/cm <sup>3</sup>	4.86 g/cm <sup>3</sup>	5.66 g/cm <sup>3</sup>	5.58 g/cm <sup>3</sup>
Areal Density	2.8 g/cm <sup>2</sup>	2.1 g/cm <sup>2</sup>	2.2 g/cm <sup>2</sup>	2.9 g/cm <sup>2</sup>
Projectile Velocity	600 m/s	500 m/s	350 m/s	650 m/s
Projectile Energy	5544 J	3850 J	1885 J	6507 J
Armor Penetration	Armor Shattered	Radial cracking	Armor Intact	Armor Shattered
Back-plate Penetration	< 5mm	None	None	1.9 cm

Figure 7.31 shows the result of impact on a 30NiTi target. The projectile was again fired at a velocity of approximately 500 m/s. However, because of the increased mass of the projectile, the energy of impact was increased to 3850 Joules. In this case, the composite armor did suffer radial cracking. The steel back-plate showed no visible penetration.



Figure 7.31 Photograph of  $\text{TiC}_{0.7}$ -30 vol%NiTi plate after 3850 Joule impact.

Figure 7.32 shows the result of two impact tests on 60NiTi targets. In Figure 7.32(a), the target was impacted by a projectile traveling at 350 m/s. The impact energy of 1885 Joules, caused only slight surface indentation. No radial cracking occurred. In Figure 7.32(b) the target was impacted with a kinetic energy of 6507 Joules. The target completely shattered, and the projectile penetrated the steel back-plate into which the target was press fit.

The highest energy projectile, which was effectively defeated in these ballistic tests, was 5544 Joules. The target armor used in this case was 20NiTi. Although the armor shattered, the steel back-plate sustained only a few mm of penetration.

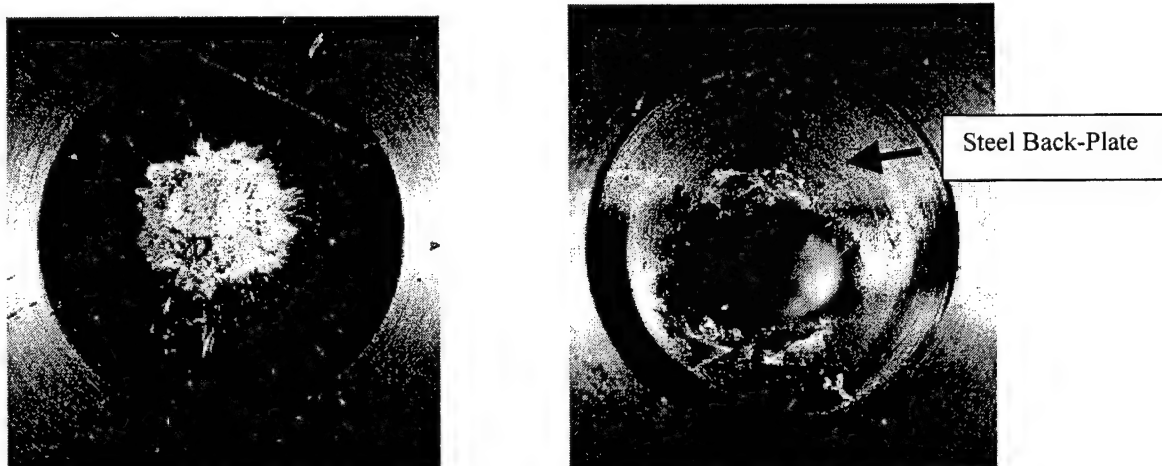


Figure 7.32 Photograph of  $\text{TiC}_{0.7}$ -60 vol%NiTi (a) after 1885 Joule impact and (b) after 6507 Joule impact.

## References

- V. V. Akimov, I. I. Vil'msen, V. E. Panin, S. N. Kul'kov, *Poroshovaya Metallurgiya*, **7** (283), 1986, 83.
- I. Barin, Thermochemical Data of Pure Substances, 3<sup>rd</sup> Edition, VCH Publishers, New York, 1995.
- M. Bauccio (ed.), ASM Engineering Materials Reference Book, 2<sup>nd</sup> Edition, ASM International, Materials Park, OH, 1994.
- T. M. Brill, S. Mittelbach, W. Assmus, M. Müllner, and B. Lüthi, *J. Phys. Cond. Mater*, **3**, 1991, 9621.
- T. E. Buchheit and J. A. Wert, *Metall. Mater. Trans A*, **27A**, 1996, 269.
- R. Chang and L. J. Graham, *J. Appl. Phys.*, **37** (10), 1966, 3778.
- T. W. Clyne and P. J. Withers, An Introduction to Metal Matrix Composites, Cambridge University Press, Cambridge, 1993.
- G. Das, K. S. Mazdiasni and H. A. Lipsitt, *J. Am. Ceram. Soc.*, **65** (2), 1982, 104.
- D. C. Dunand, D. Mari, M. A. M. Bourke, and J. A. Roberts, *Metall. Mater. Trans A*, **27A**, 1996, 2820.
- J. D. Eshelby, *Proc. Roy. Soc.* **A241**, 1957, 376.
- J. D. Eshelby, *Prog Solid Mech*, I. N. Sneddon and R. Hill (eds.), 1961, 89.
- K. L. Fukami-Ushiro, D. Mari and D. C. Dunand, *Metall. Mater. Trans A*, **27A**, 1996a, 183.
- K. L. Fukami-Ushiro and D. C. Dunand, *Metall. Mater. Trans A*, **27A**, 1996b, 193.
- T. Fukuda, T. Saburi, K. Doi, and S. Nenno, *Materials Transactions, JIM*, **33** (2), 1992, 271.
- D. Goldstein, U. S. Patent no. 4030427, June 21, 1977.
- D. Goldstein, U. S. Patent no. 5145506, Sept. 8, 1992.
- A. A. Golestaneh and J. M. Carpenter, *Acta Metall.*, **38** (7), 1990, 1291.
- E. Goo and R. Sinclair, *Acta Metall.*, **33**, 1985, 1717.

- J. E. Hanlon, S. R. Butler, and R. J. Wasilewski, *Trans. Met. Soc. AIME*, **239**, 1967, 1323.
- D. E. Hodgson, M. H. Wu, and R. J. Biermann, in: *ASM Metals Handbook*, 10<sup>th</sup> Edition, Volume 2, ASM International, Metals Park, OH, 1990, 897.
- T. Honma: in *Shape Memory Alloys*, H. Funakubo (ed.) Gordon and Breach, New York, NY (1987)
- K. Jacobus, H. Sehitoglu, and M. Balzer, *Metall. Mater. Trans A*, **27A**, 1996, 3066.Y.
- Kaieda, M. Otaguchi, O. Odawara, M. Nakamura, T. Oie, S. Shite, *Sintering* **87**, 1, 1987, 557.
- T.Y. Kosolapova (ed.), *Handbook of High Temperature Compounds: Properties, Production, Applications*, Hemisphere Publishing Corporation, New York, 1990.
- S. N. Kul'kov, T. M. Poletika, A. Y. Chukhlomin, and V. E. Panin, *Poroshkovaya Metallurgiya*, **8** (260), 1984, 88.
- J. C. LaSalvia, L. W. Meyer, and M. A. Meyers, *J. Am. Ceram. Soc.*, **75** (3), 1992, 552.
- J. C. LaSalvia, PhD Thesis, University of California San Diego, San Diego, CA, 1995.
- J. C. LaSalvia, M. A. Meyers and D. K. Kim, *J. Mat. Syn. Proc.*, **2**, 1994, 255.
- J. C. LaSalvia, D. K. Kim, R. A. Lipsett, and M. A. Meyers, *Metall. Mater. Trans A*, **26A**, 1995a, 3001.
- J. C. LaSalvia and M. A. Meyers, *Metall. Mater. Trans A*, **26A**, 1995b, 3011.
- W. P. Lichti and A. F. Hofstatter, U. S. Patent no. 4539175, Sept. 3, 1985.
- D. Mari and D. C. Dunand, *Metall. Mater. Trans A*, **26A**, 1995a, 2833.
- D. Mari, L. Bataillard, D. C. Dunand, and R. Gotthardt, *J. de Phys.*, **C8**, 1995b, C8-659.
- K. N. Melton and O. Mercier, *Acta Metall.*, **29**, 1981, 393.
- A. G. Merzhanov, in: *Combustion and Plasma Synthesis of High Temperature Materials*, Z. A. Munir and J. B. Holt (eds.), VCH Publishers, New York, 1990, 1.
- G. M. Michal and R. Sinclair, *Acta Cryst. B*, **B37**, 1981, 1803.



- D. B. Miracle and H. A. Lipsitt, *J. Am. Ceram. Soc.*, **66** (8), 1983, 592.
- S. Miyazaki, K. Otsuka, and Y. Suzuki, *Scripta Metall.*, **15**, 1981, 287.
- S. Miyazaki, Y. Ohmi, K. Otsuka, and Y. Suzuki, *J. de Phys.*, **C4**, 1982, C4-255.
- S. Miyazaki and K. Otsuka, *Metall. Trans. A*, **17A**, 1986a, 53.
- S. Miyazaki, Y. Igo, and K. Otsuka, *Acta Metall.*, **34**, 1986b, 2045.
- S. Miyazaki, K. Otsuka, and C. M. Wayman, *Acta Metall.*, **37**, 1989, 1837.
- J. J. Moore and H. J. Feng, *Prog. Mat. Sci.*, **39**, 1995a, 243.
- J. J. Moore and H. J. Feng, *Prog. Mat. Sci.*, **39**, 1995b, 275.
- Z. A. Munir and U. Anselmi-Tambourini, *Mat. Sci. R.*, **3**, 1989, 277.
- J. L. Murray, in: Binary Alloy Phase Diagrams, ASM International, Metals Park, OH, 1986.
- T. H. Nam, T. Saburi, Y. Kawamura, and K. Shimizu, *Mater. Trans. JIM*, **31**, 1990, 262.
- M. Nishida, C. M. Wayman, and T. Honma, *Metall. Trans.*, **17A**, 1986, 1505.
- N. P. Novikov, I. P. Borovinskaya, and A. G. Merzhanov, in: Combustion Processes in Chemical Technology and Metallurgy, A. G. Merzhanov (ed.), Chernogolovka, Russia, 1975, 174.
- E. Olevsky, H.J. Dudek, W.A. Kaysser, *Acta Met. Mater.* **44** (2) (1996) 707.
- E.A. Olevsky, J.C. LaSalvia, and M.A. Meyers, "Densification of Porous Bodies in a Granular Pressure-Transmitting Medium: Part I, Shrinkage Anisotropy," *to be submitted*.
- K. Otsuka, T. Sawamura, and K. Shimizu, *Phys. Stat. Sol. A*, **5**, 1971, 457.
- V. E. Panin, A. I. Slosman, B. B. Ovechkin, M. P. Bondar, and N. A. Kostyukov, *Poroshkovaya Metallurgiya*, **7** (271) 1985, 27.
- J. R. Patel and M. Cohen, *Acta Metall.*, **1**, 1953, 531.
- K. Plietsch and K. Ehrlich, *Acta Materialia*, **45**, 1997, 2417.
- T. M. Poletika, S. N. Kul'kov, and V. E. Panin, *Poroshkovaya Metallurgiya*, **7** (247), 1983, 54.
- R. V. Raman, S. V. Rele, S. Poland, J. C. LaSalvia, M. A. Meyers, and Niiler, A. R., *JOM*, **47**, 1995, 23.

- C. Rodriguez and L. C. Brown, in: Shape Memory Effects in Alloys, J. Perkins (ed.), Plenum Press, New York, 1975, 29.
- T. Saburi, T. Tatsumi, and S. Nenno, *J. de Phys.*, **C4**, 1982, C4-261.
- T. Saburi, S. Nenno, Y. Nishimoto, and M. Zeniya, *Tetsu-to-Hagane*, **72**, 1986, 571.
- T. Saburi, *Proc. MRS Int. Mtg. On Adv. Mats.*, Tokyo, Volume9, 1989, 77.
- T. Saburi, in: Shape Memory Materials, K. Otsuka and C. M. Wayman (eds.), Cambridge University Press, U.K., 1998, 49.
- R. J. Salzbrenner and M. Cohen, *Acta Metall.*, **27**, 1979, 739.
- G. D. Sandrock, A. J. Perkins, and R. F. Hehemann, *Metall. Trans.*, **2**, 1971, 2769.
- V. Skorohod, E. Olevsky, M. Shtern, *Powd. Metall. & Met. Ceram.* N1(361) (1993a) 22.
- V. Skorohod, E. Olevsky, M. Shtern, *Powd. Metall. & Met. Ceram* N2(362) (1993b) 16.
- J. F. Shackelford (ed.), CRC Materials Science and Engineering Handbook, CRC Press, Boca Raton, FL, 1994.
- E. K. Storms, *The Refractory Carbides*, Academic Press, Inc., New York and London, 1967.
- D. Stroz, *J. Phys IV*, **C5**, 1997, C5-293.
- A. N. Tabachenko and G. G. Kryuchkova, *Journal of Engineering Physics and Thermophysics*, **65**(4) 1993, 1026.
- A. Wick, O. Vöhringer, and A. R. Pelton, *J. de Phys.*, **C8**, 1995, C8-789.
- W. S. Williams and R. D. Schaal, *J. Appl. Phys.*, **33** (3), 1962, 955.
- K. Wu, F. Yang, Z. Pu, and J. Shi, *Journal of Intelligent Material Systems and Structures*, **7**, 1996, 138.